

ABSTRACT

DEAN, GARRETT JAMES. Inverse Analysis of Irradiated Nuclear Material Gamma Spectra via Nonlinear Optimization. (Under the direction of Dr. John Mattingly.)

Nuclear forensics is the collection of technical methods used to identify the provenance of nuclear material interdicted outside of regulatory control. Techniques employed in nuclear forensics include optical microscopy, gas chromatography, mass spectrometry, and alpha, beta, and gamma spectrometry. This dissertation focuses on the application of inverse analysis to gamma spectroscopy to estimate the history of pulse irradiated nuclear material. Previous work in this area has (1) utilized destructive analysis techniques to supplement the nondestructive gamma measurements, and (2) been applied to samples composed of spent nuclear fuel with long irradiation and cooling times. Previous analyses have employed local nonlinear solvers, simple empirical models of gamma spectral features, and simple detector models of gamma spectral features.

The algorithm described in this dissertation uses a forward model of the irradiation and measurement process within a global nonlinear optimizer to estimate the unknown irradiation history of pulse irradiated nuclear material. The forward model includes a detector response function for photopeaks only. The algorithm uses a novel hybrid global and local search algorithm to quickly estimate the irradiation parameters, including neutron fluence, cooling time and original composition. Sequential, time correlated series of measurements are used to reduce the uncertainty in the estimated irradiation parameters.

This algorithm allows for in situ measurements of interdicted irradiated material. The increase in analysis speed comes with a decrease in information that can be determined, but the sample fluence, cooling time, and composition can be determined within minutes of a measurement. Furthermore, pulse irradiated nuclear material has a characteristic feature that irradiation time and flux cannot be independently estimated. The algorithm has been tested against pulse irradiated samples of

pure special nuclear material with cooling times of four minutes to seven hours. The algorithm described is capable of determining the cooling time and fluence the sample was exposed to within 10% as well as roughly estimating the relative concentrations of nuclides present in the original composition.

© Copyright 2017 by Garrett James Dean

All Rights Reserved

Inverse Analysis of Irradiated Nuclear Material Gamma Spectra via Nonlinear Optimization

by
Garrett James Dean

A dissertation submitted to the Graduate Faculty of
North Carolina State University
in partial fulfillment of the
requirements for the Degree of
Doctor of Philosophy

Nuclear Engineering

Raleigh, North Carolina

2017

APPROVED BY:

Dr. Joseph Doster

Dr. Carl Kelley

Dr. Louise Worrall

Dr. John Mattingly
Chair of Advisory Committee

DEDICATION

For the world.

May my efforts contribute to its betterment.

I am of the opinion that my life belongs to the whole community and as long as I live, it is my privilege to do for it whatever I can.

- George Bernard Shaw

BIOGRAPHY

The author was born in 1987 in Longmont, CO. He grew up in the Mojave desert of California and escaped to Durango, CO to receive a B.S in Physics from Ft. Lewis College. After a short period of work at an engineering firm, he returned to school for a B.S. in Mathematics from the University of Colorado. He moved to Raleigh in 2011 to pursue his Ph.D. at North Carolina State University.

ACKNOWLEDGEMENTS

I would like to thank my advisor, Dr. John Mattingly, for his guidance and persistence. Without him, this paper and research process would have been a far less enjoyable and meaningful experience.

I would like to thank my mother Kathy Dean for her tireless encouragement and acceptance of my journey to the densely wooded, flat East Coast.

Finally, I would like to thank all those who helped with this research and writing. With high commendation to my friends and colleagues, particularly Tessa.

TABLE OF CONTENTS

LIST OF TABLES	vii
LIST OF FIGURES	viii
Chapter 1 INTRODUCTION	1
1.1 Introduction	1
1.2 Previous Work	7
1.3 Experiments	12
1.3.1 Short Lived Fission Product Gamma Measurements	12
1.4 Novel Elements of this Dissertation	16
1.5 Organization of Dissertation	18
Chapter 2 GAMMA SPECTROSCOPIC ANALYSIS	20
2.1 Irradiation Mechanics	21
2.1.1 Neutron Capture Cross Sections	22
2.1.2 Radioactive Decay	26
2.2 Forward Modeling	29
2.2.1 Bateman Equations	30
2.2.2 Neutron Spectrum Simulation	33
2.2.3 ENDF Gamma Source Term Generator	37
2.2.4 Ray Tracer	38
2.2.5 Detector Response Function	39
2.3 Comparison	44
2.3.1 Peak Fitting	44
2.3.2 Source Term Mapping	49
2.4 Inverse Analysis	52
2.4.1 Nonlinear Optimization	53
Chapter 3 ALGORITHM APPLICATION	67
3.1 Parameters	68
3.2 Results	69
3.2.1 Single Gamma Spectrum	69
3.2.2 Other Parameters	74
3.3 Multiple Spectra	79
Chapter 4 CONCLUSIONS	86
BIBLIOGRAPHY	89
APPENDIX	92
Appendix A RAY TRACER	93
A.1 Deterministic	94

A.2	Stochastic	95
A.2.1	Spherical	96
A.2.2	Cylindrical	98
A.2.3	Pseudo-code	99
A.3	Comparison	100

LIST OF TABLES

Table 1.1	PNNL observed neutron fluence and calculated number of fissions. Table composed of relevant portions from [13].	15
Table 2.1	Coefficients used in Eq. (2.15)	40
Table 3.1	Initial and final flux and irradiation time for a ^{239}Pu sample with 192 min cooling time.	70
Table 3.2	Best fit values of fluence and number of fissions compared to reported values (300K neutron spectrum).	72
Table 3.3	Fluence and cooling time calculated by the algorithm for the ^{239}Pu sample. PNNL fluence value was $2.731 \times 10^{14} [\text{n}/\text{cm}^2]$. Uncertainties for each value are less than 0.1%	75
Table 3.4	Fluence and number of fissions calculated by the algorithm using multiple spectra from the ^{239}Pu sample. PNNL fluence value was $2.731 \times 10^{14} [\text{n}/\text{cm}^2]$ and underwent 1.15×10^8 fissions.	80
Table 3.5	Fluence and number of fissions calculated by the algorithm using multiple spectra from the ^{239}Pu sample. PNNL fluence value was $2.731 \times 10^{14} [\text{n}/\text{cm}^2]$	82
Table 3.6	Comparison of composition ratios found by the algorithm to the true ratio value for various numbers of spectra and blend ratios.	84
Table A.1	Source energy and intensity for comparison of ray tracers.	100
Table A.2	Comparison between MCNP and the deterministic and stochastic ray tracers for spherical shells.	101
Table A.3	Comparison between MCNP and the stochastic ray tracer for cylindrical shells. . .	101

LIST OF FIGURES

Figure 1.1	Graphical representation of inverse solver structure.	4
Figure 1.2	WSU TRIGA reactor layout taken from an MCNP model with the sample location marked with an *	13
Figure 1.3	The measured gamma spectrum of pulse irradiated ^{239}Pu taken fifty-three minutes post irradiation.	14
Figure 1.4	PNNL STAYSL adjusted spectra for the bare, Cd-shielded, and B_4C shielded cases taken from [10].	16
Figure 2.1	The mass yield distribution for ^{235}U and ^{239}Pu for thermal neutron induced fission.	21
Figure 2.2	Watt spectrum for neutrons born from thermal neutron induced ^{235}U fission.	22
Figure 2.3	Plutonium-239 fission cross section.	23
Figure 2.4	Neutron capture cross sections for (a) ^2H , (b) ^{59}Co , (c) ^{136}Xe , (d) ^{238}U , as a function of energy.	25
Figure 2.5	Chart of nuclides with decay modes.	26
Figure 2.6	^{137}Cs decay scheme and energy levels.	28
Figure 2.7	A graphical representation of the forward modeling process.	29
Figure 2.8	Plot of MCNP flux tally segmented by energy compared to standard components of a typical light water reactor spectrum.	34
Figure 2.9	PNNL STAYSL adjusted spectra for the bare, Cd-shielded, and B_4C shielded cases with the unshielded MCNP generated spectrum shown in dots. PNNL STAYSL data from [10].	35
Figure 2.10	Plot of absolute detector efficiency versus energy.	41
Figure 2.11	Plot of typical channel versus energy calibration.	42
Figure 2.12	Plot of the full width at half maximum (FWHM) versus energy calibration.	43
Figure 2.13	The process for determining photopeak area and location for isolated photopeaks taken from an example spectrum of ^{60}Co	46
Figure 2.14	Using parameter optimization to determine the photopeak area and location.	47
Figure 2.15	Overlapping photopeaks that are rejected.	49
Figure 2.16	Flow chart for the mapping process.	51
Figure 2.17	Plot of the fifty-three minute cooling time ^{239}Pu sample with the peaks used for inverse analysis.	52
Figure 2.18	Plot of Eq. (2.20) on $x \in [0, 1.5]$	54
Figure 2.19	Plot of Eq. (2.20) and two different exhaustive mesh densities	55
Figure 2.20	Illustration of genetic algorithm operation.	58
Figure 2.21	Illustration of MCMC operation.	60
Figure 2.22	Illustration of Nelder-Mead operation.	62
Figure 2.23	Illustration of LM operation.	65
Figure 3.1	The error surface for a ^{239}Pu sample at 192 minutes cooling time for the parameters flux and irradiation time.	71
Figure 3.2	Thermal neutron induced fission cross sections for ^{233}U , ^{235}U , and ^{239}Pu	73

Figure 3.3	Comparison of measured to predicted gamma spectrum for fifty-three minute cooling time sample of ^{239}Pu	74
Figure 3.4	The error surface for a ^{239}Pu sample at 100 minutes cooling time for the parameters flux and cooling time.	76
Figure 3.5	Algorithmic determination of the relative concentration of ^{239}Pu and ^{235}U for a true value of: (a) is a 25% ^{239}Pu and 75% ^{235}U mixture, (b) is a 33% ^{239}Pu and 67% ^{235}U mixture, (c) is a 50% ^{239}Pu and 50% ^{235}U mixture, (d) is a 67% ^{239}Pu and 33% ^{235}U mixture, (e) is a 75% ^{239}Pu and 25% ^{235}U mixture	77
Figure 3.6	Error surface for ^{235}U and ^{239}Pu mass	78
Figure 3.7	Optimizing fluence using spectra taken at 20, 31, and 84 minutes cooling time. . .	81
Figure 3.8	Optimizing fluence and cooling time using spectra taken at 84 and 131 minutes cooling time.	83
Figure 3.9	25/75 $^{239}\text{Pu}/^{235}\text{U}$ blend at 20, 31, and 84 minutes cooling time.	84
Figure A.1	Arrangement of layers for a sphere of radioactive material with a single layer of shielding.	94

CHAPTER

1

INTRODUCTION

1.1 Introduction

From 2013 to 2015, the James Martin Center for Nonproliferation Studies has recorded 514 incidents of nuclear and radiological materials out of regulatory control [22]. Many of the reported incidents are relatively benign, with such occurrences as the discovery of honey with high levels of ^{137}Cs , the theft of an exit sign containing tritium, or the discovery of old radiation sources in a school cabinet. However, a few of the events are malicious. In 2013, a radiological dispersal device comprised of 1.5 kilograms of uranium was discovered under a police station in Assam, India. Two years later, three smugglers were apprehended in Moldova with a vial of ^{135}Cs , attempting to sell the material to ISIS for use against U.S. citizens.

With over 150 reported incidents per year¹, the need for technologies to interdict, identify, and determine the provenance of nuclear material has become increasingly vital. Particularly, a means of quickly determining the history of interdicted nuclear material is needed to identify and prosecute the individuals or groups responsible. This dissertation aims to assist this endeavor by providing an additional tool to the toolbox of nuclear forensics.

The current collection of tools for nuclear forensics is broad, with only a handful making use of the nuclear nature of the samples. A detailed description of the technologies available is outside the scope of this document, but a precursory account serves to illustrate the usefulness of this research. *Nuclear Forensic Analysis* has a chapter dedicated to the nuclear forensic work performed on a uranium sample interdicted in Bulgaria on May 29, 1999 [29]. The techniques used to analyze the sample were: "optical microscopy; scanning and transmission electron microscopy, both with energy-dispersive x-ray analysis; x-ray and electron diffraction; radiochemistry followed by α - and γ -spectrometry and mass spectrometry; optical emission spectrometry; ion-, gas-, and gel-permeation chromatography; gas chromatography-mass spectrometry; infrared spectrometry; x-ray photoelectron spectroscopy; x-ray fluorescence spectroscopy; and metallurgical analysis." These analyses were applied to the uranium sample and the packing material and container. It was ultimately determined that the sample was a vial stolen from a reprocessing facility that took in spent 90% enriched uranium fuel and processed it back into usable reactor fuel. Attribution of the theft and the exact reprocessing center it occurred at was not determined at the conclusion of the investigation.

Timing was unimportant for this analysis because the sample had been collected nine months

¹Two-thirds of these reported events are from North America, leaving a large number of unreported or unintercepted events occurring elsewhere in the world.

prior and the case had already gone to trial. Bulgaria lacked the resources to do a full forensic analysis, but Lawrence Livermore National Laboratory felt it would be an intriguing exercise to determine the extent of information that could be discerned. In another situation, such as the capture of the explosive device in India, attribution of the source material is a more pressing matter to prevent further attacks. Transportation to a well equipped lab, sample preparation, and the actual series of measurements is expected to take weeks to months and even then may not produce definitive results [5]. The ability to provide some information on the sample's provenance within minutes of interdiction is a useful component of the attribution process.

The objective of this dissertation is to describe an algorithm that uses gamma spectroscopy and inverse analysis to quickly provide coarse characterization of special nuclear material with short irradiation and cooling time from a research reactor. There are 241 operational research reactors with 86 in developing countries and 507 decommissioned or nonoperational research reactors in the world [19]. The international atomic energy agency lists research reactors as having the least safeguards indicating a need for nuclear forensics techniques suited to this reactor class [11]. The technologies currently used in forensic analysis are capable of detecting components in the parts-per-billion range, but as stated, they take weeks to achieve this level of precision. This new analysis method is not as sensitive as the previous methods, but what it lacks in precision, it makes up in speed. It is a nondestructive technique based on gamma spectroscopy intended to supplement, rather than supplant existing destructive analysis methods.

The algorithm described in this dissertation uses a comparison between the gamma spectroscopic measurement of a sample with (partially) unknown irradiation history and a model of the irradiation process. The forward model uses the irradiation duration, irradiation intensity, time since irradiation, and initial sample composition as input, and it outputs the photopeak intensities and locations. A nonlinear optimizer iteratively adjusts the inputs while comparing the model prediction

to the measured photopeaks from the gamma spectrum. When the difference between the model and the measurement is minimized, the parameters correspond to those the sample was exposed to. The layout of the inverse solver encapsulating the forward model is shown in Fig. 1.1.

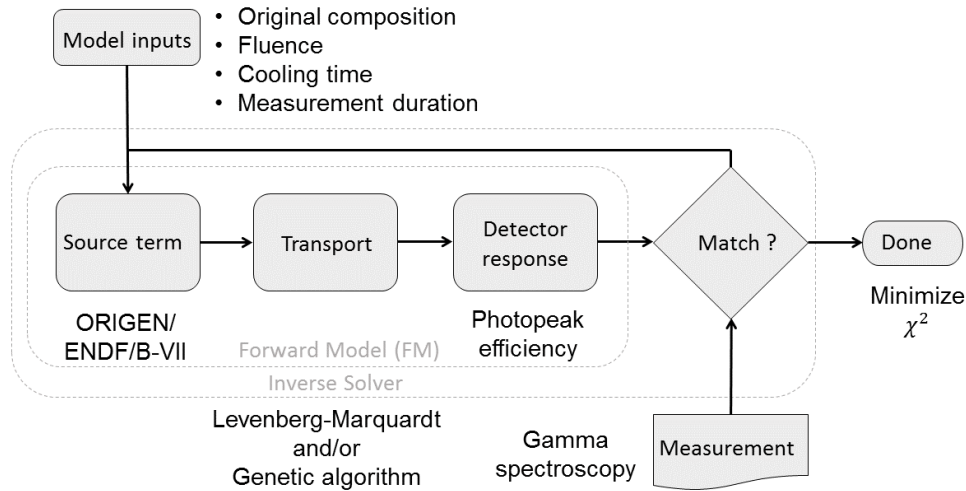


Figure 1.1 Graphical representation of inverse solver structure.

The forward model begins with ORIGEN, Oak Ridge Isotope GENERator, calculating the nuclide inventory during and after irradiation for a given initial nuclide inventory and irradiation history. The decayed nuclide inventory is converted to a list of gamma emissions using the ENDF/B-VII.1 decay sublibrary. The resulting gamma intensities and energies are the predicted gamma source term. The gamma source term is then input to the detector response function, which outputs the predicted photopeak locations and areas. The output from the forward model listing each photopeak location and intensity represents what the detector would report for the given irradiation history.

A nonlinear optimizer iteratively makes small changes to the parameters of the forward model and then compares the output to the measurement. When the difference between the measurement and the model is a minimized, the parameters are reported. The comparison is performed with a χ^2

error metric given in Eq. 1.1.

$$\chi^2(\mathbf{X}) = \sum_i \frac{(y_i - A(t_i; \mathbf{X}))^2}{\text{Var}_{y_i}} \quad (1.1)$$

where:

$A(t_i; \mathbf{X})$ = the sum of the gamma line intensities from the FM contributing to the i^{th} peak

\mathbf{X} = parameters of the model

y_i = the measured peak area of the i^{th} peak

Var_{y_i} = the variance in the area of the i^{th} measured peak

The measured peak area, y , and associated variance, Var_y is calculated from a model fit to the photopeak. The summation of counts under the photopeak and the use of Poisson statistics can also calculate y and Var_y .

The model for a photopeak in the gamma spectrum is comprised of two components: the photopeak and the underlying continuum. Eq. 1.2 is a common model for fitting photopeak data comprised of a Gaussian on top of a linear continuum .

$$f(E) = \frac{y}{\sigma\sqrt{2\pi}} \exp\left(-\frac{(E-\mu)^2}{2\sigma^2}\right) + mE + b \quad (1.2)$$

where E has units of energy (e.g., MeV) and

y = the area of peak [counts]

σ = the standard deviation in the peak [MeV]

μ = the centroid location in energy [MeV]

m = slope of the underlying continuum [counts/MeV]

b = y-axis intercept of the underlying continuum [counts]

The value of Var_y is provided by the solver or manual sampling of the error surface once the optimization has concluded.

Several local and global nonlinear solvers were tested; the combination of genetic algorithm and Levenberg-Marquardt was selected for implementation in this research. Once the genetic algorithm identifies the global minimum region, Levenberg-Marquardt completes the search. This combination was selected because global solvers require a large number of forward evaluations, but fully explore the sample space. Local solvers require few forward evaluations, but ignore candidate minima outside of the current concave region of the error surface. Together, the two are superior to each individually. They take slightly longer than a local solver, but have a high probability of converging to the global solution.

This algorithm has been tested against gamma spectra of special nuclear material (SNM) pulse-irradiated in a TRIGA reactor. The spectra were collected at Washington State University (WSU) TRIGA site by Pacific Northwest National Laboratory (PNNL) using high purity germanium detectors. Using each measured spectrum, the algorithm calculated the fluence² and number of fissions induced in the sample. The results correspond well with those published by PNNL. The algorithm

²Fluence is the product of irradiation time and flux and has units of n/cm²

also has been tested for its ability to solve for cooling time and returns a value within 5% of the true value. Finally, gamma spectra composed of spectra from pure ^{235}U and ^{239}Pu in varying ratios were created and the algorithm was used to determine sample composition, with distinctive results.

The algorithm is capable of determining irradiation intensity and duration (or the product of the two, fluence), cooling time, and relative sample composition. These properties are useful for ascertaining the provenance of interdicted material. A key finding from the research is that when irradiation duration and intensity can not be determined individually, this is indicative of material that has been pulse-irradiated.

1.2 Previous Work

Applying iterative inverse solvers to analyze irradiated nuclear material from research reactors has been performed previously by Matthew Sternat in 2012 [38]. For his doctoral dissertation at Texas A&M, Sternat analyzed a dissolved a sample of spent fuel from the Oak Ridge Research Reactor that had an initial enrichment of 93.1% ^{235}U . The sample was analyzed using inductively coupled plasma-atomic emission spectrometry, inductively coupled plasma-mass spectrometry, gamma spectrometry, and alpha spectrometry. Only the mass and gamma spectrometry measurements were used in his inverse analysis. The forward model for irradiation used a variant of MCNP that incorporates burnup effects and a generalized reactor core model to calculate the isotopic inventory during and after irradiation. The initial enrichment and burn up were estimated precisely, but the long cooling time led to an over-prediction in the the actual cooling time. His destructive methods and use of mass spectrometry allowed for the determination of initial sample composition for all uranium isotopes, which is not possible using gamma spectroscopy alone.

Dr. Charles Weber of Oak Ridge National laboratory has created an algorithm called INDEPTH

(INverse DEpletion THEory) that applies inverse analysis to the determine characteristics of spent nuclear fuel from commercial power reactors [40]. The algorithm uses the Broyden-Fletcher-Goldfarb-Shanno nonlinear optimization algorithm to determine the irradiation parameters of interest through repeated calls to the SCALE module ORIGEN. INDEPTH was initially designed to compare predicted nuclide inventories to nuclide concentrations found through destructive measurements [39]. The program was updated to individually determine the parameters reactor power and irradiation time along with burnup³, enrichment, and cooling time [8]. To allow for nondestructive assay of samples, INDEPTH was further modified to take a measured gamma spectrum and match it to a binned gamma output created by ORIGEN [40]. This change allowed for the observation of a large range of gamma energies and prevented poor estimates of a nuclide concentration from affecting the overall parameter estimation. In analyzing spent nuclear fuel, ORIGEN took advantage of the approximate cancelation between gamma attenuation within the fuel rod and detection efficiency, i.e., neither affect is explicitly modeled in INDEPTH, but their omission did not negatively impact INDEPTH's application to spent nuclear fuel.

Dr. Brandon Grogan at ORNL is now the primary individual responsible for maintaining and updating INDEPTH, and with the assistance of Dr. Weber, INDEPTH has implemented several updates [17]. The INDEPTH algorithm can make use of the DREAM(ZS) (DiffeRential Evolution Adaptive Metropolis-ZS variant) nonlinear solver, adding global search functionality and the ability to determine uncertainty for each parameter. A modification to the error metric to evenly balance the contributions from neutrons and gammas was also included. The results using neutrons are more accurate, with the same precision compared to the results from using only gamma spectroscopy. A full energy peak efficiency calibration is inversely applied to the measured gamma spectrum to determine the incident gamma flux. This allows for direct comparison with the output from

³Burnup is the product of reactor power and irradiation duration and has units of gigaWatt-days per metric ton of heavy metal (GWD/MTHM).

ORIGEN without the need to apply a detector response function after each ORIGEN run. With these updates, simultaneously optimizing initial enrichment, cooling time, and burnup using only gamma measurements results in parameter values within 10% of declared values [16].

The INDEPTH algorithm is the most complete and automated inverse method for spent fuel analysis, but it is not the only method, nor is ORNL the only organization developing forensic analysis of spent nuclear fuel. Ian Gauld and Matthew Francis developed a full spectrum analysis program to determine the amount of various nuclides present within a sample using passive gamma spectroscopy, though no analysis was performed [14]. Kwang-June Park et. al used gamma spectra to find the content of ^{134}Cs and ^{137}Cs within a spent fuel rod and then compared the ratio to a table of values computed by ORIGEN to determine the plutonium to uranium ratio in and the burnup experienced by the sample [33].

Christofer Willman's doctoral dissertation expanded on the work by Kwang-Park et. al by including ^{154}Eu to help determine when fuel assembly declarations were in error [41]. Willman's method uses the amount of ^{134}Cs determined from the appropriate photopeak and a comparison to the predicted intensity using an ORIGEN based forward irradiation model. If a discrepancy was found, then the ratios using the measured amounts of ^{154}Eu , ^{137}Cs , and ^{134}Cs could determine whether burnup, cooling time, power level, composition, or number of cycles had been reported in error [41].

The analyses by Sternat, Weber, and Willman all use spent nuclear fuel with cooling times of less than ten years. Samples with cooling times longer than this are not used because at time scales longer than a year, a gamma spectrum from irradiated nuclear fuel contains approximately ten photopeaks from a handful of nuclides. At longer time scales, most of these nuclides decay, leaving only the emissions from the long lived ^{137}Cs . As was shown by Skutnik, at these long time scales, the solution space for determining irradiation history has degeneracies due to the limited information

available [37].

Each of the previous methods primarily used gamma measurements of the spent fuel, making use of the natural radioactive decay of the fission products. However, an alternative method for determining irradiation history is an active measurement. In the dissertation by Vladimir Mozin, passive gamma spectroscopy was used after a D-T generator irradiated the spent fuel and created new fission products [30]. The high background from the fuel made observing induced gamma emissions below 3 MeV impossible. Even with this constraint, the methodology was able to determine relative concentrations of ^{235}U , ^{238}U , ^{239}Pu , and ^{241}Pu post-irradiation. The potential for determining initial composition was discussed but not implemented.

Inverse problems are not unique to nuclear forensics and have existed for centuries. One of the earliest documented inverse problems was the discovery of Neptune by Urbain Le Verrier. Le Verrier was able to use the discrepancy between the Newtonian prediction for Uranus's orbit and the actual orbit to predict the mass and location of the planet Neptune [3]. Nearly two hundred years later, the first systematic attempt to solve an inverse problem was performed by Viktor Ambartsumian in 1929 when he attempted to find the equations for a given set of eigenvalues [2]. Inverse problems, often called parameter optimization, are prolific now and applications are found in nearly every industry.

Methods for solving nonlinear problems are numerous, but a few methods are particularly noteworthy. The Nelder-Mead algorithm uses an $N+1$ dimension simplex and a series of simple rules to modify the simplex to move towards the local minimum. It has slow convergence compared to more advanced methods, but requires no derivative evaluations [31]. The Levenberg-Marquardt algorithm is a method using steepest descent when the search is far from the minimum and transitioning to Gauss-Newton as the algorithm approaches the solution [23, 26]. Markov Chain Monte

Carlo(MCMC) has a history stretching back to the Manhattan project with the first MCMC algorithm described by Metropolis in 1953 [35]. MCMC is a global solver that uses Bayesian inference to find a distribution for the parameters rather than a single value. Genetic algorithms are discussed in the dissertation by Adenike Adewuya. He provides an overview of genetic algorithms including the various means of reproduction, crossover, and mutation implemented in genetic algorithms and introduces the quadratic crossover method for accelerating convergence [1].

The process of peak fitting is used in the analysis of gamma spectra from irradiated material and is another application of nonlinear optimization. One of the most complete descriptions of the models for the continuum and photopeak is given by Helmer and Lee [18]. The paper compares ten equations for the underlying continuum and fifteen for the photopeak, with the conclusion that models using more parameters provide better fits, but are also more sensitive to initial values and less likely to converge. Numerous other papers have looked into differing methods for peak fitting with Bayesian being a preferred alternative to gradient based parameter optimization [25, 36].

This research focuses on material irradiated in pulsed reactors and uses data from samples irradiated in a TRIGA pulsed reactor. The TRIGA reactor used for irradiating the SNM was created in 1956 by Edward Teller as a reactor that has inherent safety through its unique fuel design [15]. The TRIGA reactor was used by Metz et al. to investigate fission yields of short lived fission products from SNM [28, 10]. Metz et al. also determined that there existed a large variance in the fluence a sample was exposed during a pulse event within the TRIGA, and fluence wires were needed to determine actual fluence for a given pulse [34]. The variances were most likely caused by variations in fuel rod composition from trace elements, and initial position, final position, and/or removal speed of the control rod. The research by Irena Mele et al. found that when using fresh fuel in their TRIGA the predicted fuel temperature, pulse width, total energy, and peak power all matched the predicted values very well [27]. Many groups have measured the flux in a TRIGA reactor using fluence wires

[21, 7, 34] or estimated it by modeling [4].

1.3 Experiments

1.3.1 Short Lived Fission Product Gamma Measurements

In January of 2011, Pacific Northwest National Laboratory (PNNL) made use of the Washington State University (WSU) Training, Research, Isotopes, General Atomics (TRIGA) reactor to pulse irradiate pure samples of special nuclear material in various configurations and then measure the resultant gamma spectrum from each of the samples. The gamma measurements began four minutes post irradiation and continued for approximately seven hours at the TRIGA site. Samples were also transported to PNNL to undergo measurements from six to 218 hours. This research focuses solely on the measurements made at WSU.

The samples were composed of highly pure ^{235}U , ^{233}U , ^{239}Pu , and ^{237}Np . Each sample of special nuclear material was dissolved in an acid solution and then drip deposited on filter paper before being dried. A Tedlar® packaging was sealed around the sample to retain the gaseous fission products⁴. The sample was placed into a thin polyethylene container in either a bare or a shielded configuration. Two shields composed of cadmium and B_4C were selected to limit thermal and thermal/epithermal neutrons respectively. This resulted in three pulsed measurements, one unshielded and one for each shielding configuration, for each sample except ^{237}Np which was not irradiated in the unshielded configuration. The sample container was placed outside the reactor core as shown in Fig. 1.2.

The reactor was brought to a stable power level and then the control rod was removed from the center of the reactor producing a pulse of neutrons several orders of magnitude more intense than the stable operating condition. The reactor quickly returned to a stable operating level. Within four

⁴PNNL later states the packaging was ineffective at retaining the gaseous fission products and some unknown amount escaped.

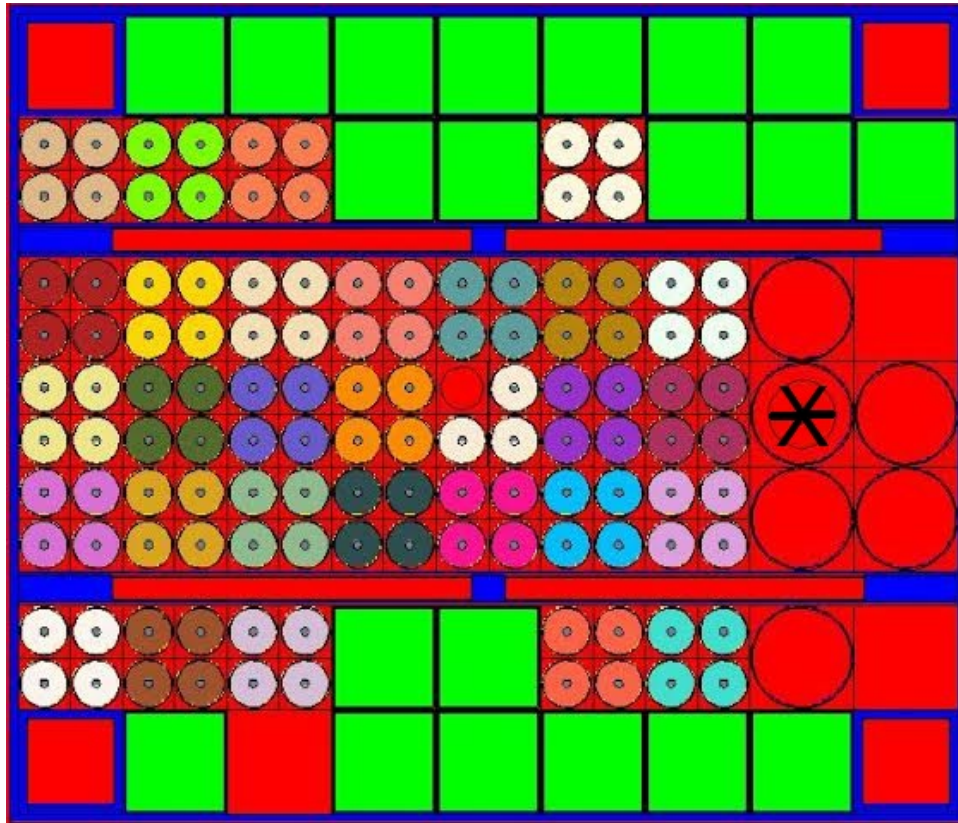


Figure 1.2 WSU TRIGA reactor layout taken from an MCNP model with the sample location marked with an *.

minutes, the sample was removed from the reactor and placed 11.5 cm from a 68% efficient⁵ HPGe detector. When the dead time decreased to 5%, the detector to sample distance was decreased to 5.1 and then 2.6 cm. Measurements were of increasing duration, beginning with a five minute dwell time and concluding with a one hour dwell time for the measurement begun more than four hours post irradiation. An example spectrum is shown in Fig. 1.3.

⁵Detector efficiency is measured relative to the number of 1332 keV photons recorded in 3 in × 3 in NaI detector.

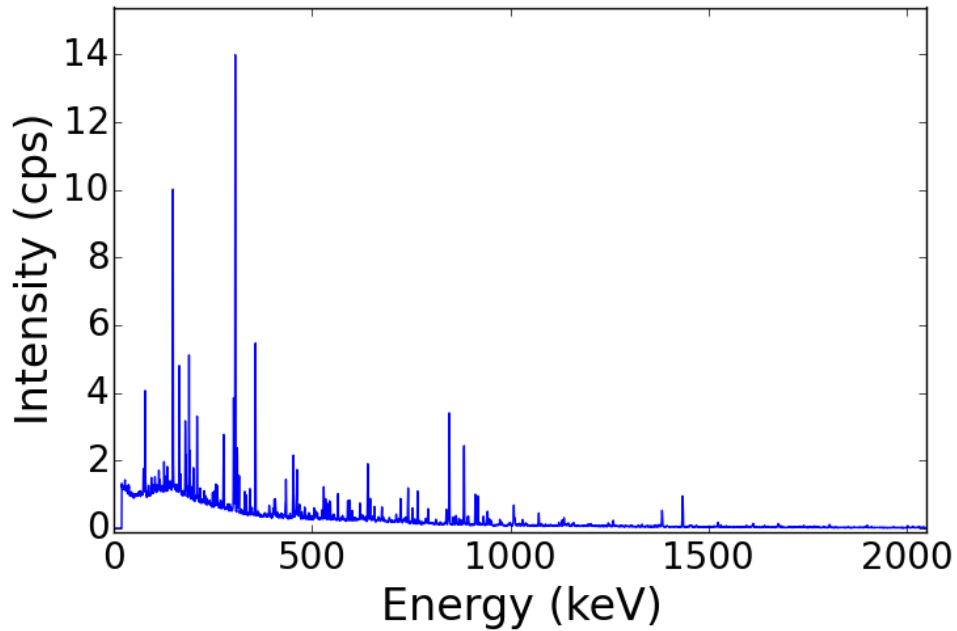


Figure 1.3 The measured gamma spectrum of pulse irradiated ^{239}Pu taken fifty-three minutes post irradiation.

Included with each sample, inside the respective shielding, were a series of pure metals⁶ to determine the fluence the sample experienced by delayed gamma neutron activation analysis. For each wire, the nuclides comprising each wire have a large neutron capture cross section in a particular region, but are low otherwise, making them selectively sensitive to different portions of the neutron spectrum. A capture reaction in the wire is most likely to occur for a neutron with an energy in the sensitive region and causes the stable nuclide to transmute into a radionuclide. When the wire was taken from the irradiation environment and measured by an HPGe detector, the gamma emissions from the newly created radionuclides were recorded. The photopeak area, along with the detector efficiency, are used to calculate the sample activity and radionuclide mass. The capture cross section and nuclide mass are used to estimate the fluence in the sensitive region that the wire sample was exposed to. Table 1.1 displays the PNNL calculated fluence in three regions and number of fissions induced in

⁶The metals used were copper, iron, titanium, cobalt-vanadium alloy, and gold-aluminum alloy.

the sample.

Table 1.1 PNNL observed neutron fluence and calculated number of fissions. Table composed of relevant portions from [13].

Target spectrum/shielding	Isotope	Observed neutron fluences (n/cm ²)			Calculated Fissions
		Thermal (% uncertainty)	Epithermal (% uncertainty)	Fission (% uncertainty)	
Bare	²³³ U	2.01×10 ¹⁴ (2)	6.17×10 ¹³ (10)	2.50×10 ¹³ (12)	1.70×10 ⁸
	²³⁵ U	2.19×10 ¹⁴ (3)	5.37×10 ¹³ (10)	2.59×10 ¹³ (5)	1.14×10 ⁸
	²³⁹ Pu	2.01×10 ¹⁴ (2)	4.92×10 ¹⁰ (10)	2.29×10 ¹³ (10)	1.15×10 ⁸
Cd-shielded	²³³ U	<1×10 ¹¹	8.53×10 ¹³ (5)	3.48×10 ¹³ (8)	2.35×10 ⁸
	²³⁵ U	<1×10 ¹¹	6.17×10 ¹³ (10)	3.60×10 ¹³ (2)	2.36×10 ⁸
	²³⁹ Pu	<1×10 ¹¹	6.52×10 ¹³ (10)	2.83×10 ¹³ (9)	1.61×10 ⁸
B ₄ C-shielded	²³³ U			2.19×10 ¹³ (7)	1.40×10 ⁸
	²³⁵ U			3.54×10 ¹³ (6)	6.54×10 ⁸
	²³⁹ Pu			3.57×10 ¹³ (6.3)	1.78×10 ⁸

A range of elements were selected to span the neutron spectrum. A total of nine overlapping energy regions were sampled, having neutron sensitivities from 0.01 eV up to 12 MeV. PNNL then used the calculated neutron intensities for each region as input to STAYSL PNNL, a code that adjusts the neutron spectrum using the number of neutron capture events in each sample as guidance, until a spectrum is found that matches the observations. WSU maintains an MCNP (Monte Carlo N-Particle transport code)⁷ model of the TRIGA reactor accounting for burnup and trace nuclides in each of the fuel elements. The MCNP model was used to calculate the base neutron spectrum for input to STAYSL PNNL (a PNNL update to the ORNL dosimetry unfolding least-squares code STAY'SL). STAYSL PNNL modified this spectrum by decreasing the neutron intensity from thermal regions and increasing epithermal region intensity [10]. Fig. 1.4 shows the three neutron spectra output from STAYSL PNNL.

⁷MCNP is a stochastic radiation transport code that uses a model to calculate neutron flux at various points, among other quantities.

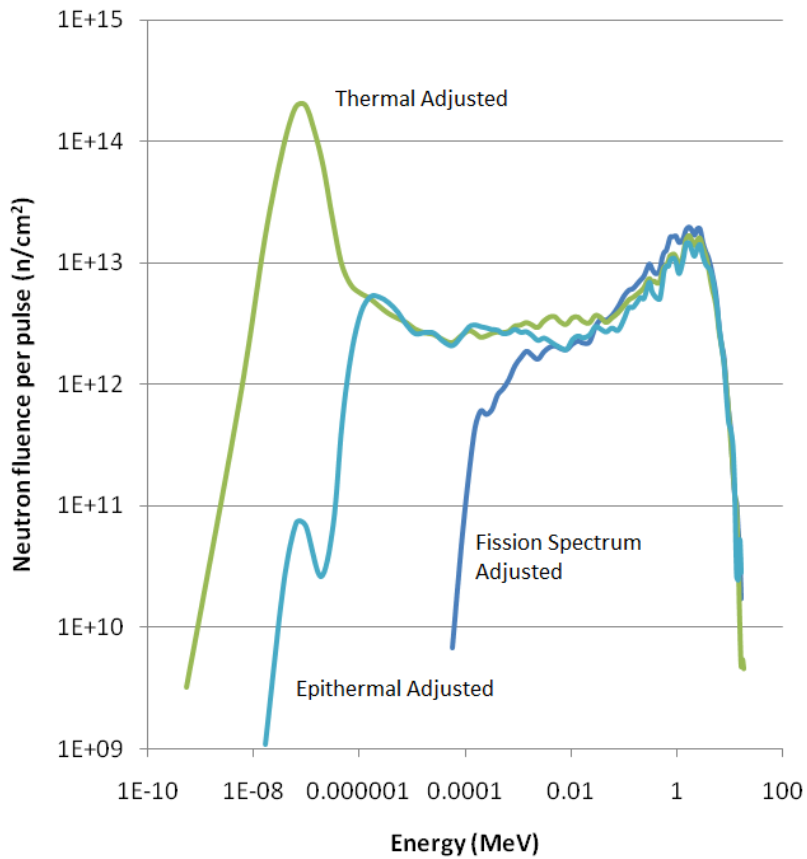


Figure 1.4 PNNL STAYSL adjusted spectra for the bare, Cd-shielded, and B₄C shielded cases taken from [10].

1.4 Novel Elements of this Dissertation

This dissertation expands on the previous work done in analyzing spent nuclear fuel, particularly for the application of nuclear forensics. Significant effort has been focused on analyzing spent fuel from commercial and research power reactors, using fuel rods that have been out of the reactor for years. Very little focus has been placed on fuel with cooling times less than one year when a large number of radionuclides are active. The long cooling time of these samples leaves only a handful of active radionuclides available for gamma spectroscopic analysis leading to degeneracies in the

solution space. The use of destructive measurements alleviates the degeneracies, but increases the time to complete the measurements.

Some of the previous analysis methods have used simple detector response functions, but often the analysis is performed using peaks that are in close proximity. Two photopeaks close to one another will have approximately the same detector efficiency and thereby enable the analysis to be performed without a detector response function. Analysis is performed using relative ratios of nuclides with absolute values being determined through supplemental methods. In the case of INDEPTH, the detector model was applied to the measured spectrum instead of the incident flux, preventing the inclusion of effects due to transport in the forward model.

Finally, most spent fuel analyses use a table look up, empirical model, or a local nonlinear solver. These methods have been shown to be effective, but leave open the possibility of degenerate solutions. By preselecting the photopeaks or nuclides to be analyzed, a large amount of information is discarded that could potentially improve the accuracy and precision of the inverse solution.

This dissertation expands in these areas to provide a means for analyzing short cooling time, pulse irradiated nuclear materials using a detector response function and a global solver. In summary, this research incorporates the following elements into a novel method for the nondestructive determination of parameter estimates for irradiated nuclear material:

- Capability to perform inverse analysis on material from an arbitrary irradiation environment/reactor, particularly pulsed reactors;
- Full spectrum analysis (not a limited number of pre-selected peaks) of high resolution gamma data;
- Combined genetic algorithm and Levenberg-Marquardt for finding the global and local error minimum, and;

- Incorporation of a detector response function, with the option for radiation transport.

1.5 Organization of Dissertation

This dissertation begins with a description of irradiation mechanics in chapter two. A explanation of neutron induced fission and neutron capture cross sections, along with radioactive decay, is provided. Chains of multiple neutron captures and/or decays are described. The means for calculating the neutron spectrum and the effect of the spectrum on cross sections is also described.

The chapter continues by describing the component parts of a forward radiation generation and detection model. The chapter begins by describing the methods used to determine a time dependent nuclide inventory for a given initial nuclide inventory and neutron spectrum. A means of converting the nuclide inventory to a gamma source term using the ENDF decay sublibrary is described. The equations used to describe the detector response for the impinging gamma term finish the forward model.

The chapter concludes by detailing the inverse algorithms available and methods for comparing the forward model to measured data. The global search options include exhaustive, genetic algorithm, and Markov Chain Monte Carlo. Local search methods include Nelder-Mead and Levenberg-Marquardt. The functioning of each is described and applied to an example problem. A hybrid method combining the genetic algorithm and Levenberg-Marquardt is also described. The chapter then finishes by describing the fitting of photopeaks in a gamma spectrum and making comparisons between model predictions of peak intensities and measurements.

In chapter three the algorithm is applied to the gamma spectra measured by PNNL. The algorithm's estimates of fluence are compared to the results provided by PNNL. Additionally, cooling

time is allowed to vary and compared to the known measurement start times. Each sample irradiated by PNNL was pure, so mixtures of spectra from the pure ^{235}U and ^{239}Pu samples are used to determine the relative sample composition. The chapter concludes by looking at the same three parameters, but for multiple spectra simultaneously, rather than individually.

The dissertation concludes in chapter four with a summary of the findings and a description of improvements to further extend the algorithm. Finally, appendix A contains information on the deterministic and stochastic ray tracer that was developed for this dissertation.

CHAPTER

2

GAMMA SPECTROSCOPIC ANALYSIS OF IRRADIATED NUCLEAR MATERIAL

This section describes how gamma spectroscopy can be used to determine the provenance of irradiated special nuclear material. The process uses a forward model comprised of a gamma source term generator, a radiation transport engine, and a detector model. The forward model prediction is compared to a measurement, and the differences guide changes to the forward model. The process of comparison and modification is repeated until the differences between the prediction and the measurement are minimized. Parameter optimization, which iteratively executes the forward model and changes the parameters, can be performed by several possible inverse solvers. Each piece of the algorithm will be described in this section.

2.1 Irradiation Mechanics

Neutron induced fission is the primary interaction this research is based upon. In neutron induced fission, a neutron interacts with a nucleus and the nucleus splits into two fragments. These two fragments are created with masses described by the distribution shown in Fig. 2.1.

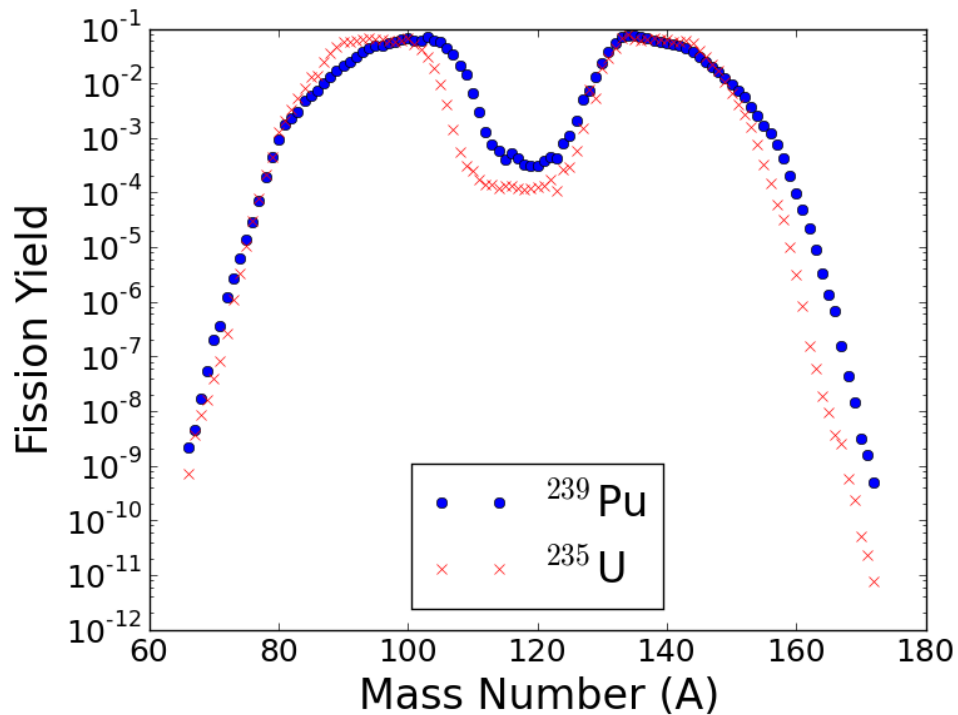


Figure 2.1 The mass yield distribution for ^{235}U and ^{239}Pu for thermal neutron induced fission.

The mass distributions for two fissionable nuclides, ^{235}U and ^{239}Pu , are shown in Fig. 2.1. Samples of these nuclides will be irradiated and the resultant gamma spectra analyzed later. The differences in the mass distribution will be exploited to distinguish between the two nuclides when they are both present in the measured spectrum.

Each fission fragment obtains kinetic energy from the fission event and travels away from the fission site. Femtoseconds after the creation of the two daughter fragments, a random number of neutrons is emitted with a distribution of energies. This distribution is called a Watt fission spectrum, and the Watt fission spectrum for ^{235}U is shown in Fig. 2.2.

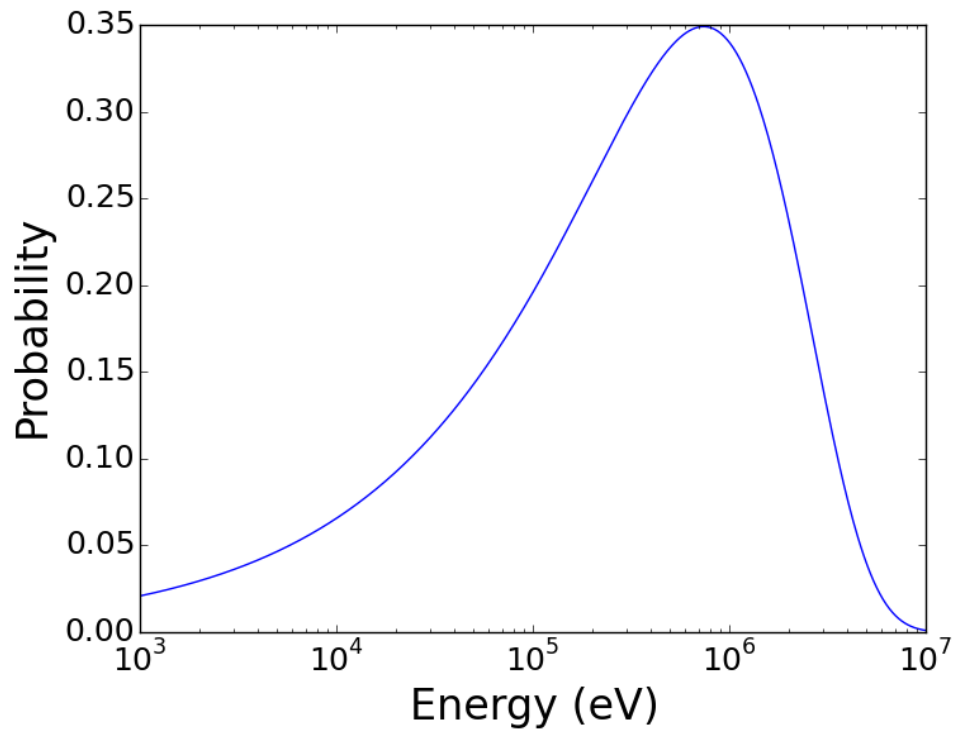


Figure 2.2 Watt spectrum for neutrons born from thermal neutron induced ^{235}U fission.

2.1.1 Neutron Capture Cross Sections

The probabilistic interaction of a neutron and a nucleus is described through cross sections. Cross sections have a basis in the apparent size of a nucleus and are measured in units of barns where 1 barn= 10^{-24} cm². In simplest approximation, nuclei with a higher atomic mass have a larger cross section and the more energy a neutron has, the less time it is present to interact with the nucleus

resulting in a corresponding decrease in cross section. This has some physical basis for scattering, but quantum effects modify this simplistic representation and create a complex, energy dependent behavior in the cross-section. Cross sections have been measured for each type of interaction a nucleus can undergo. For a neutron hitting a nucleus, the possible interactions are inelastic and elastic scattering, fission, and capture. The interactions of interest for this research are those where a nucleus captures a neutron: neutron induced fission and neutron capture.

The effects of neutron induced fission have been described previously. The fission cross section is a function of incident neutron energy and is displayed in Fig. 2.3 for ^{239}Pu . Fig. 2.3 shows the highly

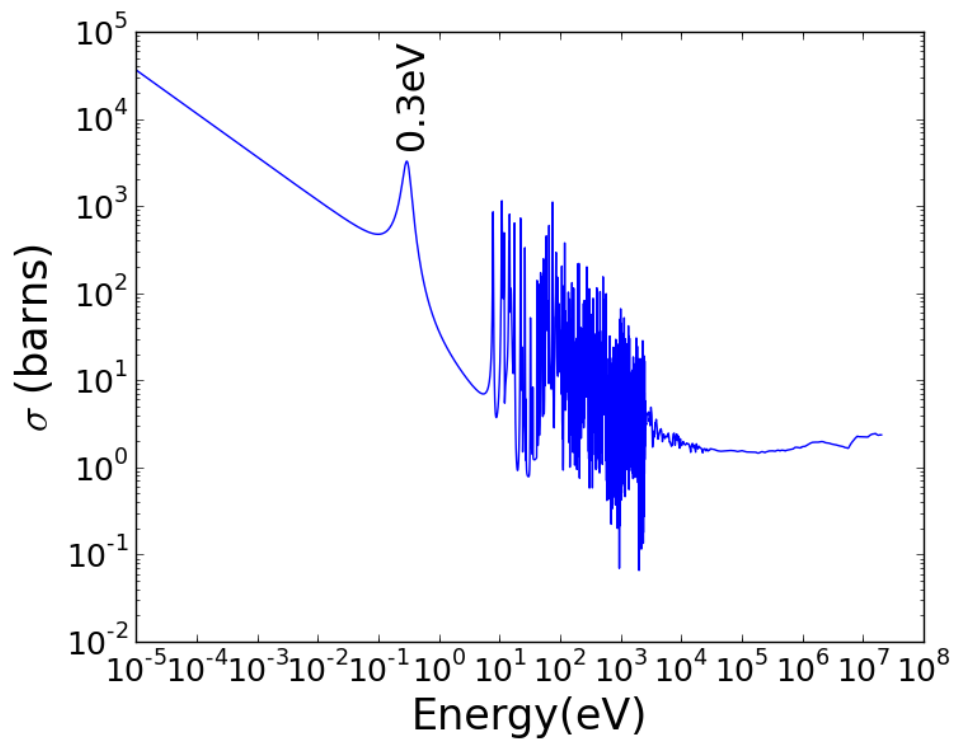


Figure 2.3 Plutonium-239 fission cross section.

complex and energy dependent behavior that is typical for fissionable transuranic nuclides. There is a $1/v$ region for low energies and resonances from the nuclear structure. Neutrons are far more likely to induce fission in one of these regions than near 1 MeV where they are typically born as shown in Fig. 2.2.

Neutron capture causes the transmutation of nuclei. The addition of a neutron to the nucleus increases the nucleon number by one and can take it from stability to instability. Unlike fission, the capture reaction does not require a high atomic number to occur but is possible for every element. Neutron cross sections for ^2H , ^{59}Co , ^{136}Xe , and ^{238}U are shown in Fig. 2.4. Each of these nuclides are stable¹ but they become the unstable nuclides ^3H , ^{60}Co , ^{137}Xe ², and ^{239}U ³ with the addition of a single neutron. In each cross section there is a $1/v$ dependence at low energies. Nuclei more complicated than hydrogen have resonances corresponding to their more complicated nuclear structure. The cross section magnitude also varies for each nuclide, being higher for uranium than hydrogen.

The cross sections can be used to determine the change in nuclide concentration through the equation

$$\frac{dN}{dt} = -\sigma\phi N \quad (2.1)$$

where

ϕ = neutron flux [$\text{n}/\text{cm}^2/\text{s}$],

σ = cross section [$\text{cm}^2/\text{nucleus}/\text{n}$],

N = nuclide concentration [$\text{nuclei}/\text{cm}^3$].

¹ ^{238}U is unstable with a 4.4 billion year half life that decreases by thirteen orders of magnitude to 23 minutes with the addition of one neutron.

² ^{137}Xe decays to the well known gamma emitter ^{137}Cs .

³ ^{239}U decays to ^{239}Pu in two steps over 2.3 days for the breeding of new fissionable fuel.

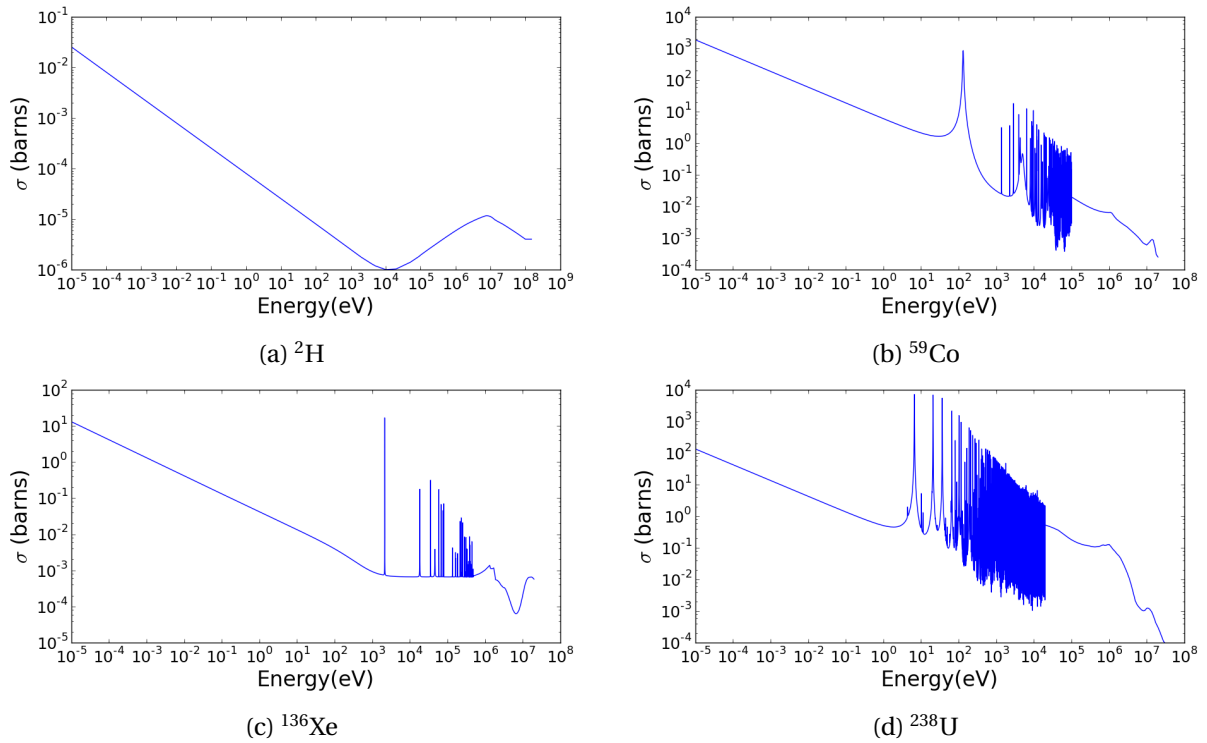


Figure 2.4 Neutron capture cross sections for (a) ^2H , (b) ^{59}Co , (c) ^{136}Xe , (d) ^{238}U , as a function of energy.

which has a solution at time t of

$$N(t) = N_0 e^{-\sigma\phi(t-t_0)} \quad (2.2)$$

where

N_0 = the initial concentration of N at $t = t_0$

t_0 = the initial time.

2.1.2 Radioactive Decay

When a nucleus is created from a nuclear reaction, there can be an excess of one type of nucleon. Protons repel one another while neutrons help to hold the nucleus together. An excess of either causes instability. The unstable nuclei will balance out the excess nucleons through various decay process and result in a more stable state. The chart of the nuclides and the dominant decay modes for each nuclide are shown in Fig. 2.5.

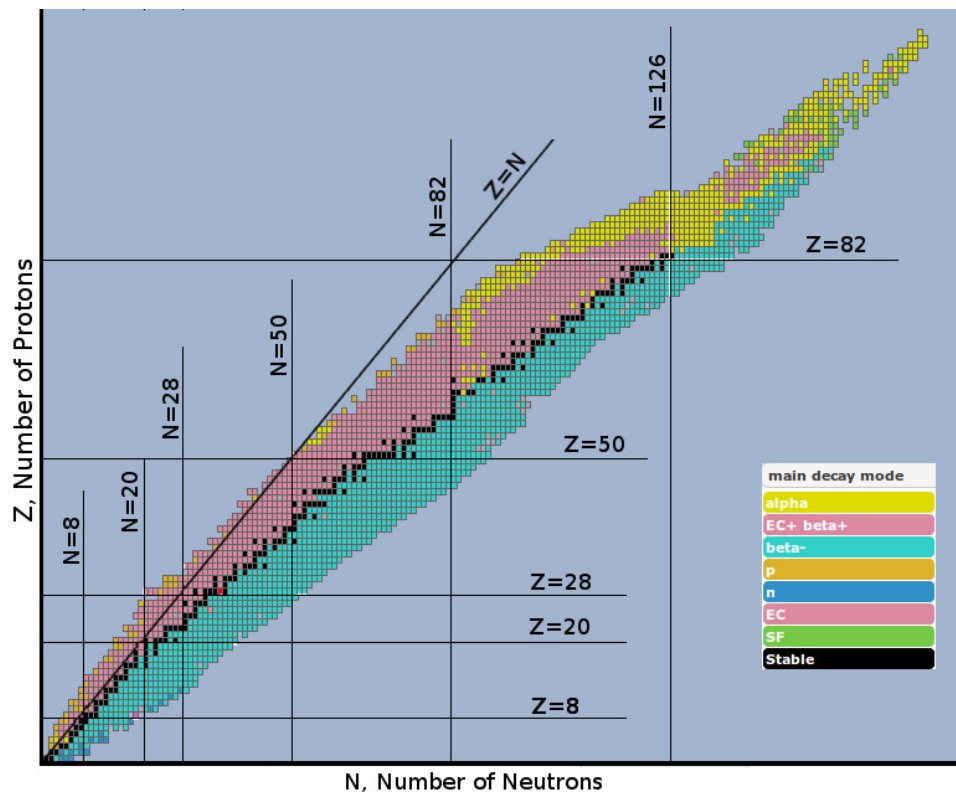


Figure 2.5 Chart of nuclides with decay modes. Source: https://upload.wikimedia.org/wikipedia/commons/9/9e/Decay_Mode_Valley_of_Stability.jpg

The daughter products of nuclear fission are neutron heavy (below the line of the stable nuclides

in Fig. 2.5), and will decay via beta-minus emission: the transformation of a neutron to a proton by emission of an electron⁴. This process maintains the number of nucleons while increasing the number of protons, resulting in a less neutron-heavy nucleus.

After a radioactive decay occurs, the daughter nucleus is often left in an excited state. The energy levels of the nucleus are determined by the allowed spin, rotational, and vibrational states. Quantum mechanics and the kinematics of the reaction determine the particular excited state a nucleus is left in following a radioactive decay. These excited states are unstable and decay by emitting the excess energy as a gamma ray or cascade of gamma rays. The quick emission of excess energy leads to the inclusion of the gamma ray(s) with the previous radioactive decay. The decay scheme and energy levels for ¹³⁷Cs are shown in Fig. 2.6.

¹³⁷Cs is a fission product that decays through the beta-minus decay mode, typical of all fission fragments. Approximately 95% of the time, the daughter nucleus ¹³⁷Ba is left in an excited state that is 662 keV above the ground state. When the ¹³⁷Ba nucleus relaxes to the ground state, this excess energy is emitted as a gamma ray 85% of the time, and through internal conversion⁵ the remaining times. The beta decay followed by subsequent 662 keV gamma emission acts as a fingerprint unique to the ¹³⁷Cs nuclide, with other nuclides having their own identifying gamma emission(s).

⁴An antineutrino is also ejected during the beta decay

⁵The internal conversion process ejects an orbital electron with kinetic energy equal to the excited state less the electron binding energy.

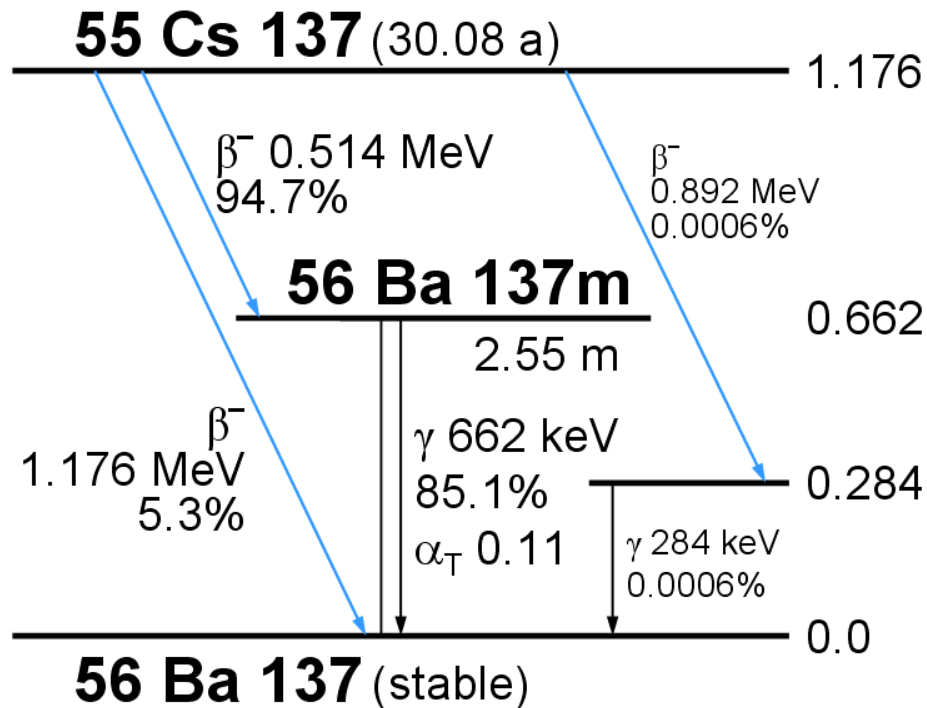


Figure 2.6 ^{137}Cs decay scheme and energy levels. Source: <http://www.nucleonica.net/wiki/images/7/7f/Cs137keV.png>

The decay of a single nuclide occurs randomly, but for large numbers of nuclei, the decrease in the nuclide population is proportional to the number of nuclei present.

$$\frac{dN}{dt} = -\lambda N \quad (2.3)$$

where N is the number of nuclei and λ is the decay constant of the nuclide in units of inverse time. The value of λ is unique to each nuclide and related to the commonly used quantity of half-life through

$$T_{1/2} = \frac{\ln(2)}{\lambda} \quad (2.4)$$

The solution of Eq. (2.3) at time, t , is

$$N(t) = N(t_0)e^{-\lambda t} \quad (2.5)$$

where $N(t_0)$ is the initial amount of the nuclide present at initial time, t_0 .

2.2 Forward Radiation Modeling

The forward model (FM) uses models of physical phenomena to create a synthetic gamma spectrum. The predicted spectrum is controlled by parameters that will be iteratively adjusted by the inverse solver described in section 2.4. Fig. 2.7 shows the flow chart of the FM calculations.

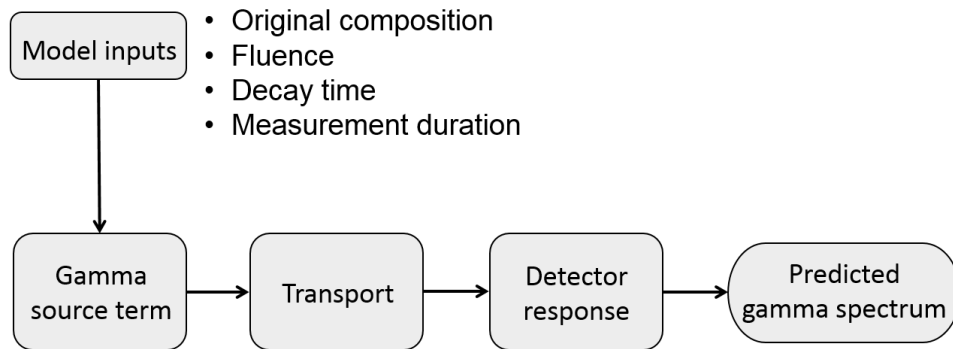


Figure 2.7 A graphical representation of the forward modeling process.

The FM consists of a gamma source term generator, a transport model, and detector model. The gamma source term model is composed of a nuclide inventory calculator and a nuclide-to-gamma energy and intensity converter. The transport model accounts for the effects of intervening materials between the gamma source and the detector and can be deterministic or stochastic in nature. The detector model simulates the gamma interaction with the detector and returns what would be recorded for an incident gamma flux. It can calculate the photopeaks or simulate the entire spectrum

depending on quality of the calibration measurements. The sequential implementation of these components creates the synthetic gamma spectrum and are known collectively as the forward model. Each component will be discussed in detail in the following section.

2.2.1 Bateman Equations

Neutron capture and radioactive decay have been described as isolated events, but this is not always the case. A nuclide may undergo multiple neutron interactions, decay events, or a combination of neutron capture and radioactive decays. The loss of one type of nuclide is an increase in a different nuclide creating a coupled system of equations describing neutron capture and radioactive decay conversions between the nuclides. The coupled differential equations describing the change in every nuclide are given by:

$$\frac{dN_i}{dt} = \sum_{j=1}^m l_{ji} \lambda_j N_j + \bar{\Phi} \sum_{k=1}^m f_{ki} \sigma_k N_k - (\lambda_i + \bar{\Phi} \sigma_i) N_i, \quad (i = 1, \dots, m) \quad (2.6)$$

where

N_i = atom density of nuclide i [nuclei/cm³],

λ_i = radioactive disintegration constant of nuclide i [decays/nucleus/s],

σ_i = spectrum-averaged neutron absorption cross section of nuclide i [cm²/nucleus/neutron],

$\bar{\Phi}$ = position- and energy-averaged neutron flux [n/cm²/s],

l_{ji} = branching fractions of radioactive disintegrations from other nuclides j [decays resulting in nuclide i]/[decays],

f_{ki} = branching fractions for neutron absorption by other nuclides k that lead to the formation of species i [absorption resulting in nuclide i]/[absorptions],

m = total number of nuclides.

Equation (2.6) describes the change in a single nuclide and how it is interdependent with other nuclides. This single nuclide produces other nuclides through decay or neutron absorption, while being produced from the decay or neutron absorption events of other nuclides. The dependence of each nuclide on others creates interdependence among the nuclides that is mathematically represented by a linear system of first order differential equations. The system can be represented in matrix form as

$$\frac{d}{dt} \vec{N} = \mathbf{A} \vec{N} \quad (2.7)$$

where \mathbf{A} is the matrix:

$$\mathbf{A} = \begin{bmatrix} -\lambda_1 - \bar{\Phi} \sigma_1 & l_{21} \lambda_2 + \bar{\Phi} \sigma_2 f_{21} & \cdots & l_{M1} \lambda_M + \bar{\Phi} \sigma_M f_{M1} \\ l_{12} \lambda_1 + \bar{\Phi} \sigma_1 f_{12} & -\lambda_2 - \bar{\Phi} \sigma_2 & \cdots & l_{M2} \lambda_M + \bar{\Phi} \sigma_M f_{M2} \\ \vdots & \vdots & \ddots & \vdots \\ l_{1M} \lambda_1 + \bar{\Phi} \sigma_1 f_{1M} & l_{2M} \lambda_2 + \bar{\Phi} \sigma_2 f_{2M} & \cdots & -\lambda_M - \bar{\Phi} \sigma_M \end{bmatrix} \quad (2.8)$$

and $\vec{N} = [N_1, N_2, \dots, N_M]^T$ is a vector of nuclide atom densities. Each of the components comprising \mathbf{A} comes from the evaluated nuclear data file (ENDF) database. The value of $\bar{\Phi}$, the single group flux related to the power/flux in the reactor, is provided as an input. The values λ , l , and f are all known nuclear data properties. The values for σ_x are dependent on the neutron spectrum, but are calculated before the forward model is run as described in section 2.2.1.

Similar to Eq. (2.5), the solution to Eq. (2.7) is :

$$\vec{N}(t) = e^{\mathbf{A}t} \vec{N}_0 \quad (2.9)$$

where $\vec{N}_0 = \vec{N}(t = 0)$ is the initial density of each nuclide. This can be evaluated using the Taylor expansion of the matrix exponential

$$e^{\mathbf{A}t} = \mathbf{I} + \mathbf{A}t + \mathbf{A} \cdot \mathbf{A} \frac{t^2}{2!} + \mathbf{A} \cdot \mathbf{A} \cdot \mathbf{A} \frac{t^3}{3!} + \dots = \sum_{k=0}^{\infty} \frac{(\mathbf{A}t)^k}{k!} \quad (2.10)$$

where \mathbf{I} is the identity matrix. For an initial nuclide inventory \vec{N}_0 , the expansion described in Eq. (2.10) gives a nuclide inventory $\vec{N}(t)$ of

$$\vec{N}(t) = \sum_{k=0}^{\infty} \frac{(\mathbf{A}t)^k}{k!} \vec{N}_0 \quad (2.11)$$

Computationally, an infinite expansion is impossible. The SCALE module ORIGEN was selected to calculate the time dependent nuclide inventory for this research. Instead of an infinite expansion, it truncates the infinite expansion to $3.5[\mathbf{A}]t + 6$ terms where $[\mathbf{A}] = \min \left\{ \max_i \sum_j |a_{ij}|, \max_j \sum_i |a_{ij}| \right\}$ [32],[6]. The matrix \mathbf{A} is also modified to account for short lived fission products (nuclides whose diagonal entry $-d$ causes $e^{-dt} < 0.001$) by omitting short half-life, intermediate nuclides and going straight to long-lived nuclides. The concentrations of these nuclides are calculated after the expansion is performed using the preceding nuclide. Using the truncated expansion, ORIGEN is capable of computing the nuclide inventories with a computational error of less than 0.1%, in a very short amount of processing time.

COUPLE

COUPLE is a module of SCALE that generates the one-group cross section libraries used by ORIGEN. COUPLE collapses the ENDF multi-group neutron cross sections stored in the SCALE database to one-group cross sections using a user supplied, multi-group, problem-dependent flux as a weighting function [32]. The multi-group neutron spectrum is used to collapse the multi-group cross-section

according to

$$\sigma = \frac{\sum_{i=1}^N \phi_i \sigma_i}{\sum_{i=1}^N \phi_i} \quad (2.12)$$

where ϕ_i is the flux for energy group i and σ_i is the cross section for group i .

Equation (2.12) takes the 238 energy group neutron flux generated using MCNP, as described in section 2.2.2 and combines it with cross section data that accompanies SCALE to create a single group, problem-dependent cross section. This is performed for every nuclide and reaction in the SCALE database. The collapsed cross-sections are then used in the irradiation calculation performed by ORIGEN.

2.2.2 Neutron Spectrum Simulation

The Bateman equations given in Eq. (2.6) and the matrix in Eq. (2.8) use energy averaged cross sections. The ENDF cross sections used as a data source are stored in an energy dependent structure. The method used to convert the multi-group data to a single group has been described previously, but the process requires a weighting function which is nominally an estimate of the energy-dependent flux as in Eq. (2.12). These weights correspond to the neutron energy spectrum. A computer model of the reactor is used to calculate the relative neutron intensity in each energy energy bin.

A stochastic transport code such as MCNP or GEANT4 can be used to model and tabulate the neutron spectrum. However, running a Monte Carlo simulation of a reactor is a time intensive process regardless of the computational power. For a constant reactor arrangement, the time intensive simulation only needs to be run to convergence once, not every time the forward model is run. After the neutron spectrum has converged, the results are stored and then recalled as necessary for use with the forward model, alleviating the need for expensive Monte Carlo runs. A tally within the

reactor collects the flux averaged over the cell associated with the sample location. The neutron spectrum at the sample location is simulated by scoring this tally within energy bounds corresponding to those used by the cross section collapsing code COUPLE. An example of the neutron spectrum obtained from the simulation of a light water reactor compared to expected features is shown in Fig. 2.8.

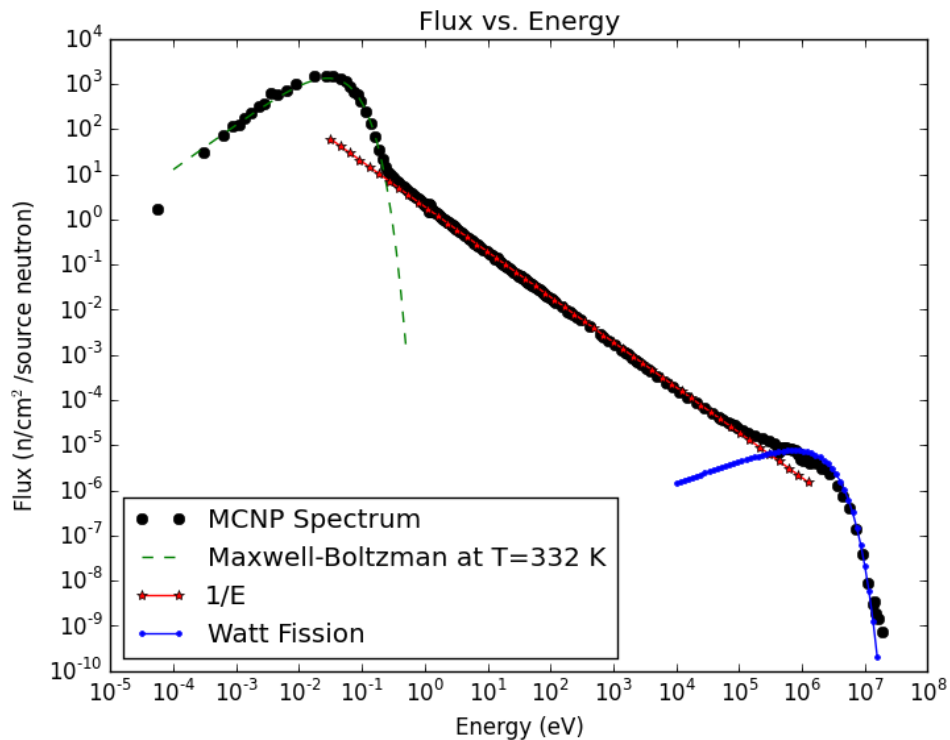


Figure 2.8 Plot of MCNP flux tally segmented by energy compared to standard components of a typical light water reactor spectrum.

The spectrum conforms to the expected spectrum of a light water reactor. It has a Watt fission spectrum at high energies, giving way to a 1/E slowing down region, and finally transitioning to a Maxwell-Boltzman distribution at low energies [24]. The Watt fission spectrum comes directly from the energy distribution of neutrons born from a fission event as was shown in Fig. 2.2. The 1/E

slowing occurs as neutrons interact with the moderator, hydrogen nuclei within the water, and give up their energy through elastic scattering collisions. The Maxwell-Boltzman distribution describes the energies of neutrons of a given average temperature that equilibrate with the surrounding medium.

The neutron spectrum in Fig. 2.8 comes from the WSU MCNP model of the TRIGA reactor described in chapter 1. As research reactors capable of pulsed operation typically use a light water moderator, a standard LWR spectrum can be used without the need for time intensive simulation. A similar model can be created for any reactor to model the neutron spectrum within the reactor if the sample being analyzed is believed to come from a different class of reactor. A comparison of the neutron spectrum generated for this research to the STAYSL PNNL adjusted spectrum is shown in Fig. 2.9.

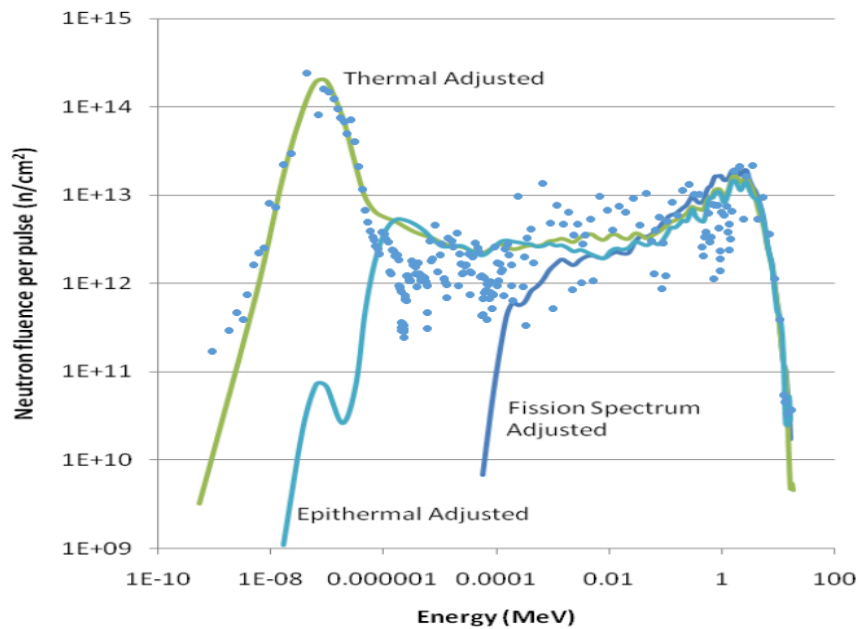


Figure 2.9 PNNL STAYSL adjusted spectra for the bare, Cd-shielded, and B₄C shielded cases with the unshielded MCNP generated spectrum shown in dots. PNNL STAYSL data from [10].

Nuclide Inventory Processing

When evaluating Eq. (2.11), for long irradiation periods, nuclides created through neutron interaction can themselves capture neutrons. These nuclides were not present in the initial composition and as such have values of zero in the initial condition vector, \vec{N}_0 . To account for multiple capture reactions involving these nuclides, the irradiation time interval is broken into small steps and the composition at the end of each mini-step is used as the input at the start of the next mini-step⁶.

Similarly, during and after irradiation, radionuclides decay and produce daughters that were not present in $\vec{N}_0(t)$. To model the ingrowth of these new nuclides, multiple time steps are taken during the cooling period. The commonly held rule for decay is that no time step should be more than a factor of three greater than the previous time step [32]. As such, the rule of three is applied until the measurement begins. This time step spacing maintains equally spaced steps on a logarithmic scale.

The measurement period was broken into several time steps (nominally five divisions) to capture ingrowing and decaying nuclides, because the measurement duration is long relative to the half-lives of some of the nuclides. The composition from each interval was computed via ORIGEN and then trapezoidal integration was used to obtain an average nuclide composition during the measurement. The trapezoidal rule to compute the integral is

$$\frac{1}{t_{end} - t_{start}} \int_{t_{start}}^{t_{end}} f(t) dt \approx \frac{1}{2N} \sum_{k=1}^N (f(t_{k+1}) + f(t_k)) \quad (2.13)$$

This process was repeated for each nuclide to arrive at the average nuclide composition contributing

⁶The functionality of breaking the irradiation period up for longer irradiations was implemented but deemed unnecessary for this research due to the short irradiation time.

to the gamma source term during the measurement.

Using the average nuclide concentration over the time interval of interest allows for the observation of nuclides that have a high concentration and activity early in the measurement, but also have a short half-life and decay away by the end of the measurement. Alternatively, a daughter product of radioactive decay may only exist in small amounts at the start of the measurement, but later it may grow in and make a significant contribution to the gamma spectrum at the end of the measurement.

For data analyzed in this research, all gaseous nuclides and associated daughter products were omitted from analysis, because the measured sample only partially retained these nuclides. Each sample was heat-sealed in Tedlar® packaging to retain gaseous fission products, but PNNL reported that there was some leakage. Since the exact amount of each gaseous nuclide escaping is unknown, and modeling the transport of gaseous fission products is outside the scope of this research, they were ignored in the analysis.

2.2.3 ENDF Gamma Source Term Generator

A list of nuclides and their concentrations is a useful forward model output if the comparison uses mass spectrometry measurements, but is insufficient for gamma spectroscopy measurements. The ENDF/B-VII.1 decay sublibrary provides the information needed to transform the nuclide inventory to a gamma source term. The sublibrary contains every radioactive nuclide and its associated radiation type, energy, and emission probability.

The gamma emission rate is calculated by:

$$\# \text{ of } \gamma \text{ emissions/second} = \frac{P_{emiss} \lambda_i N_i M}{\rho} \quad (2.14)$$

where

N_i = nuclide density of type i [nuclei/cm³],

P_{emiss} = probability of γ emission per decay [γ s/nucleus],

λ_i = decay constant for nuclide i [1/s],

M = sample mass [g],

ρ = sample mass density [g/cm³].

Performing this calculation for every nuclide in the inventory generates the gamma source term, which is a list of all emitted gamma energies and associated intensities. The full gamma source term has tens of thousands of lines, but only a handful that are dominant. A cut off is imposed to restrict the number of lines to those that will make a measurable contribution. The minimum intensity must be within five orders of magnitude of the most intense emission. From these lines, the lines contributing the top 99% of total gamma ray intensity are selected to further remove gamma lines that have limited contribution to the spectrum.

2.2.4 Ray Tracer

The gamma rays emitted from the sample are electromagnetic waves that interact with the electrons in the surrounding environment. These materials cause attenuation of the photon flux. A ray trace code was developed to account for transport effects of uncollided gamma rays, but was deemed unnecessary for this research due to the thin sample size. A detailed description of the ray tracing process and code is included in Appendix A. Geometric efficiency is included in the detector response function.

2.2.5 Detector Response Function

The gamma source term arriving at the detector is input to the detector response function (DRF) to simulate the interaction of radiation with, and the output from, the detector. The ideal detector response function would be a complete DRF, such as is provided by GADRAS⁷, allowing for the modeling of Compton continuum, backscatter, and escape peaks, along with photoelectric capture peaks. An interface to GADRAS was created for this purpose, but a GADRAS detector model requires individual spectra covering a range of energies to iteratively calibrate the model. The PNNL data included a single measurement of several calibration sources that was insufficient to create a GADRAS model. The information was sufficient to create a simplified detector response function that predicts photopeak areas instead of the full spectrum. This single calibration spectrum provided information for absolute efficiency, channel, and full width at half maximum (FWHM) calibrations.

The measurement used to determine the calibration is performed with radionuclides of known activity. The calibration measurement is performed using the calibration sources in the same geometric configuration as will be used later. The photopeaks in the measured spectrum are fit to determine their area, centroid, and standard deviation using the method subsequently described in section 2.3.1. The area corresponds to the number of photons of that energy detected. The ratio of the number of photons emitted from a source to the number detected gives the efficiency. The channel location compared to the known gamma emission energy provides the channel to energy calibration. Finally, the standard deviation of each photopeak at the particular gamma energy provides the FWHM vs. energy calibration.

⁷GADRAS stands for gamma detector response and analysis software and is maintained by Sandia National Laboratory.

Absolute Detector Efficiency

The absolute detector efficiency accounts for both geometric and intrinsic efficiencies. Geometric efficiency is the solid angle the detector subtends from the source. Intrinsic efficiency accounts for how likely a detector is to record an event for a given energy gamma ray hitting the detector. The calibration is broken up into high and low energy regions. This piece-wise definition is utilized because two effects interact and cause a maximum efficiency near 120 keV for a high purity germanium detector (HPGe). Lower energy gammas are attenuated by the detector housing and the outer dead region of the germanium, and higher energy gammas have a lower likelihood of being captured within the sensitive region of the detector.

The model for the detector efficiency for both regions is given as:

$$\epsilon(E) = \exp(C_0 + C_1 \ln(E) + C_2 (\ln(E))^2 + C_3 (\ln(E))^3 + \dots) \quad (2.15)$$

where the constants C_0 , C_1 , C_2 , etc. are determined through least squares fitting to the calibration data. The number of coefficients needed in each region is typically determined through visual inspection of the fit line to the calibration data. Example coefficient values used in the best fit lines are displayed in Table 2.1. These values are for one particular detector location, and change when the detector to source distance is changed.

Table 2.1 Coefficients used in Eq. (2.15)

	C_0	C_1	C_2	C_3	C_4	C_5
$E \leq 122$ keV	-55.75	29.18	-5.235	0.3019		
$E > 122$ keV	-392.9	324.1	-106.8	17.48	-1.423	0.0461

A plot showing the absolute efficiency versus energy with best fit lines is shown in Fig. 2.10. The dots denote the measured efficiency and the line shows the equation of best fit.

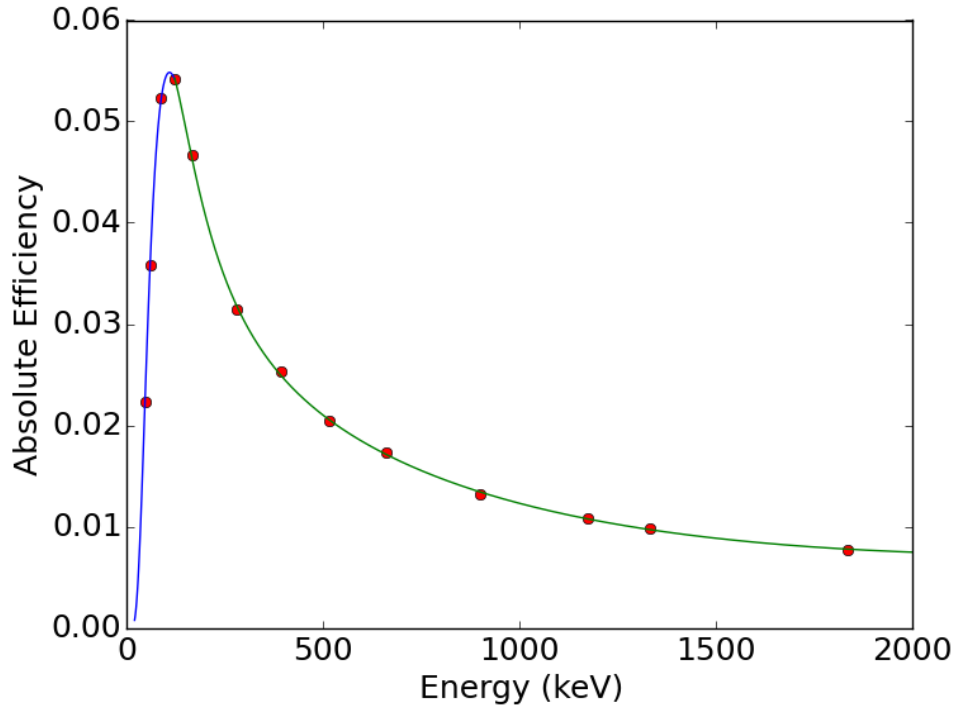


Figure 2.10 Plot of absolute detector efficiency versus energy.

Channel vs. Energy

The multi-channel analyzer (MCA) attached to the gamma detector outputs the number of detected counts versus MCA channel. Each channel corresponds to a small range of incident gamma energies. The channel vs. energy calibration converts channel number to units of energy through a quadratic equation. An example form is:

$$E = -0.396 + 0.500x - 1.08 \times 10^{-7} x^2 \quad (2.16)$$

where x is the spectrum channel number. These coefficients are typical for HPGe detectors; the calibration is nearly linear with a small nonlinear term. A plot of this calibration is shown in Fig. 2.11. No data points are included, because the spectrum this equation was taken from did not include the data points used to determine the coefficients.

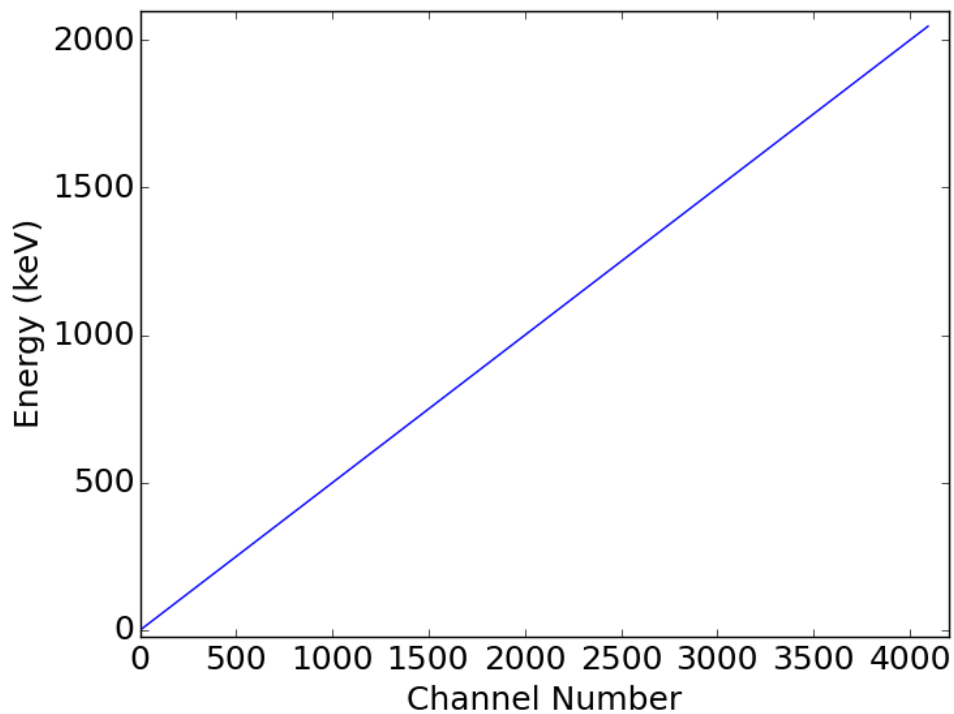


Figure 2.11 Plot of typical channel versus energy calibration.

FWHM vs. Energy

The full width at half-maximum (FWHM) calibration describes the width of a photopeak at half of its maximum height for a given energy. This description is related to the Gaussian shape described in Eq. 1.2, where the width of the Gaussian at half of its maximum height is given as $FWHM = 2.35\sigma$.

An example FWHM calibration is:

$$\text{FWHM} = 0.514 + 0.037\sqrt{E} \quad (2.17)$$

A plot showing the expected FWHM versus energy is displayed in Fig. 2.12. No data points are included, because the spectrum this equation was taken from did not include the data points used to determine the coefficients.

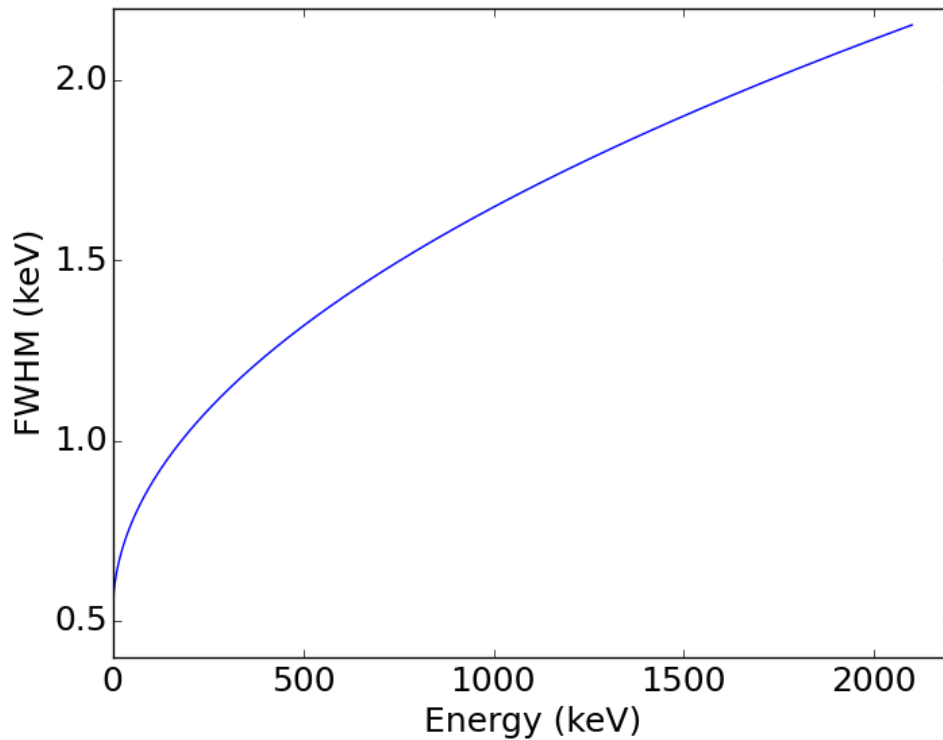


Figure 2.12 Plot of the full width at half maximum (FWHM) versus energy calibration.

Application

The detector calibrations function as a DRF using the area of photopeaks. Inputting an energy from the gamma source term to Eq. (2.15) provides the absolute detector efficiency for that energy.

The predicted number of gamma rays that fully deposit their energy in the detector is found by multiplying the full energy peak efficiency and the gamma intensity. This value directly corresponds to the measured area of a photopeak and this process is the final step in the forward model.

The FWHM and channel versus energy calibrations are used for peak fitting (described subsequently in section 2.3.1) at the start of the inverse analysis routine and for plotting as needed. The channel vs. energy calibration's purpose is two-fold. First, it provides a basis for comparison between the measured spectrum reported in channels and the equivalent energies of the gamma source term. Second, it allows for the plotting of the spectrum as intensity vs. energy. The FWHM calibration provides an initial estimate of the photopeak standard deviation for peak fitting.

2.3 Comparison of Prediction to Measurement

The FM predicts the location and area of photopeaks for a given set of parameters. These peak values need to be compared to what was measured using a HPGe detector to know if the parameters are an accurate representation of the irradiation history. This process is performed through peak fitting and comparison.

2.3.1 Peak Fitting

High purity germanium detectors can have an energy resolution of 0.3% or less where resolution is given as:

$$R = \frac{\text{FWHM}}{H_0} = \frac{2.35\sigma}{H_0} \quad (2.18)$$

where

R = Resolution

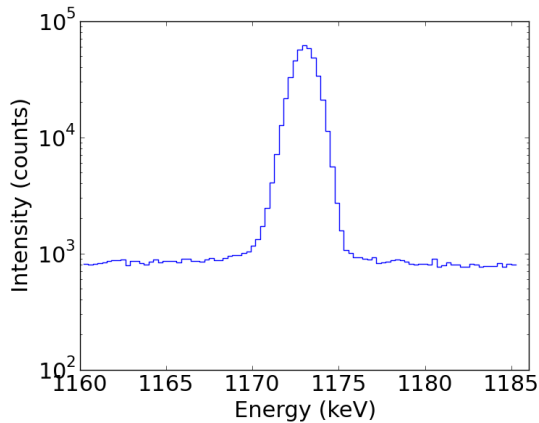
FWHM = Full Width at Half Maximum

σ = Peak standard deviation

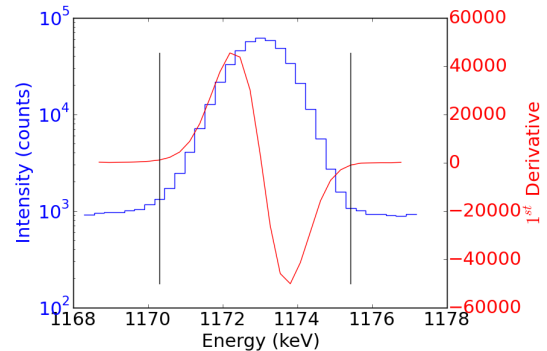
H_0 = The peak centroid [same units as FWHM or σ].

The high resolution causes photopeaks to be spread across a limited number of channels. The values of peak centroid, peak width, peak area, and underlying continuum need to be determined from these channels in order to compare a measured spectrum to the forward model. There are a number of methods to determine these characteristics, from channel summation to fitting.

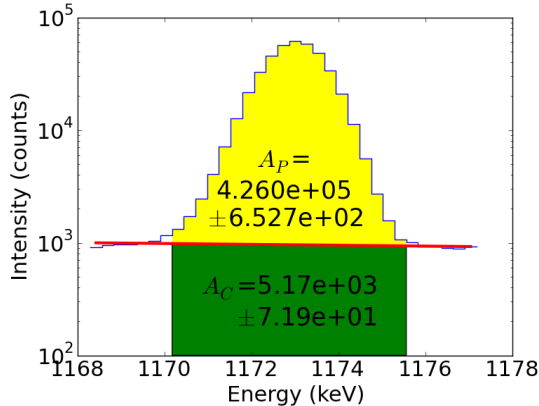
For isolated peaks, i.e., peaks that are sufficiently far from other peaks that they do not overlap, summation is an ideal method for calculating peak area. This process begins by determining the edges of the photopeak through visual inspection or a derivative based approach. All the channels within the photopeak bounds are summed to find the area of the peak and the underlying continuum. The channels just outside the photopeak are used to determine the underlying continuum, usually via a straight line connecting the two edges. The trapezoidal area bound by these points is the underlying continuum and is subtracted from photopeak channel summation to determine the net peak area. The peak centroid is found by either selecting the channel with the largest number of counts or by fitting a cubic spline to the channels bracketing this channel and using a derivative to determine the location of the maximum. The photopeak area and location are sufficient to compare to results from the forward model prediction. This process is illustrated in Fig. 2.13 for the 1173 keV photopeak of ^{60}Co .



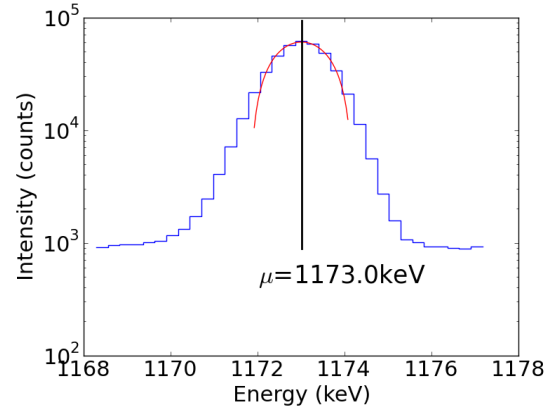
(a) The 1173 keV photopeak from ^{60}Co is isolated and on a flat continuum.



(b) Taking the first derivative around the peak to determine the peak edges.



(c) Linear continuum created from points external to the photopeak bounds separating the photopeak and continuum areas.



(d) A cubic polynomial is fit to the top seven points. The maximum of the cubic is the peak centroid.

Figure 2.13 The process for determining photopeak area and location for isolated photopeaks taken from an example spectrum of ^{60}Co .

The other method commonly used for finding peak parameters is nonlinear optimization. It has the benefit of being able to deal with overlapping photopeaks if a more advanced model is provided. In this method, a window is placed in the gamma spectrum that extends to $\pm 5\sigma^8$ around the expected peak centroid where σ is determined from the FWHM calibration. The optimal parameters are

⁸For a Gaussian peak, $\pm 5\sigma$ included 99.9999% of the photopeak area and has sufficient information at the edges to describe the underlying continuum.

those that minimize the difference between the measurement and the Gaussian model in Eq. (1.2).

Fig. 2.14 shows the fit with relevant information for the 1173 keV photopeak discussed previously.

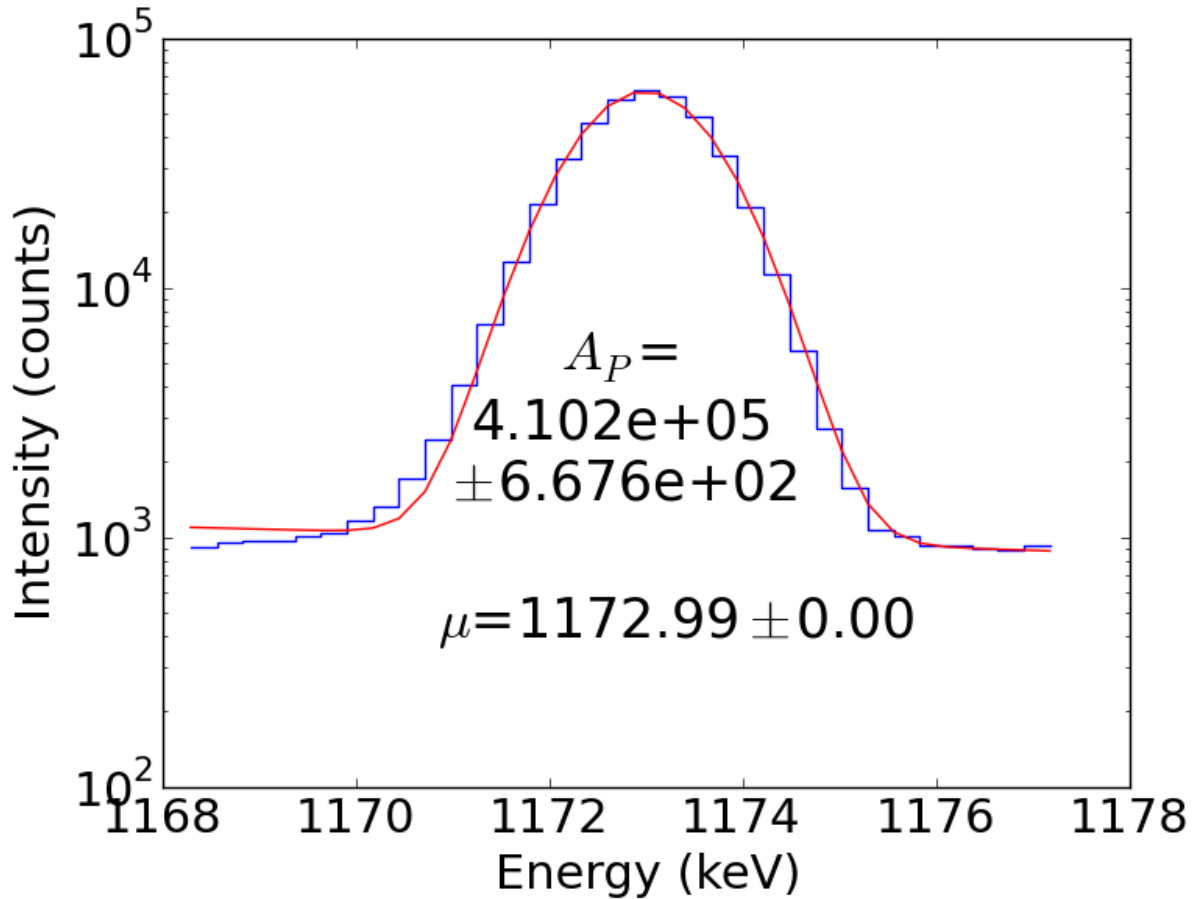


Figure 2.14 Using parameter optimization to determine the photopeak area and location.

The parameter optimization is performed using optimization methods described in 2.4, Levenberg-Marquardt being the preferred method and Markov Chain Monte Carlo being the favored alternative. For optimizations that converge, a series of criteria are used to validate the parameters. The criteria are:

- The centroid must be within two standard deviations of the predicted centroid, or the peak fit

may not be the one that is intended.

- The standard deviation must be within 50-150% of the predicted standard deviation or the peak may be convolved with another. This criterion is kept quite loose as the FWHM calibration is often a poor predictor of the actual standard deviation, using a square root instead of an exponent utilizing the appropriate Fano factor⁹.
- The area must be within 30-300% of the predicted value. This criterion is quite loose as the initial guess may be far from the true solution causing a peak to be far smaller (or larger) than expected.
- The fit spectrum can not cross the average value of the measured spectrum within in the window more than twice. This prevents fitting overlapping peaks and accounts for the possibility of a different photopeak being just outside the window with an edge inside the window, affecting the underlying continuum.

A plot of a photopeak that fails to meet all the criteria is shown in Fig. 2.15.

⁹The Fano factor is defined as $\frac{\text{observed variance in } N}{\text{Poisson predicted variance } (N)}$ where N is the number of charge carriers for a radiation detection event. It is around 0.1 for HPGe detectors.

Peak Fit Comparison

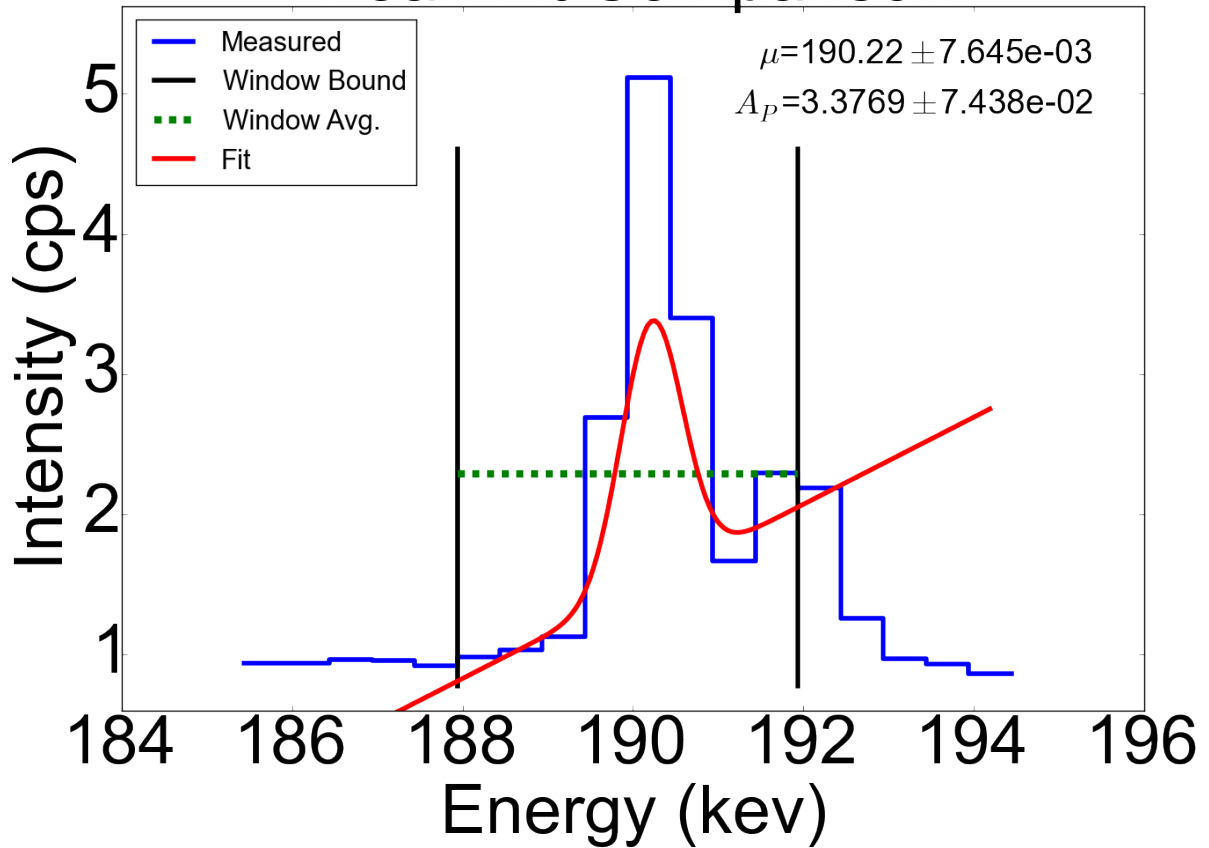


Figure 2.15 Two photopeaks in close proximity (but more than 4.3σ according to the predicted gamma emissions) that are rejected. The spectrum outside the fitting window is included for reference.

2.3.2 Source Term Mapping

The process of predicting the gamma source term and fitting measured photopeaks are separate functions. The two are combined together through a technique termed mapping. The mapping process uses the gamma emissions from the forward model to indicate the locations of the measured spectrum where the photopeak fitting process should be performed. The predicted gamma energies are sorted in descending order by intensity and processed sequentially until predicted intensity is

five orders of magnitude smaller than the most intense emission. This process ensures that only gamma emissions sufficiently intense to result in a photopeak are searched for, and that the most intense lines have priority over weaker emissions. Each predicted gamma emission has a window drawn around it that encompasses the full width at tenth maximum¹⁰. All other predicted gamma emission intensities within the window are summed. If the total of the other emissions are in excess of 1% of the main gamma emissions, the photopeak is discarded and the next one in the list is selected to begin the process again. Otherwise, the gamma line is treated as a distinct peak and the fitting process is performed. More stringent requirements on the window width and the total summation value causes excess rejection of the photopeaks.

The measured spectrum within the window and the initial values to be used in the Gaussian model are used as input to the peak fitter. The initial values for location and area are taken from the energy and intensity estimated by the forward model prediction, and the peak uncertainty is taken from the FWHM calibration for the peak's energy. The underlying continuum is initially assumed to be zero. The peak fitting process is run, and if a photopeak is fit and passes the preceding criteria, the gamma emission that began the process is associated with the measured peak area. Later comparisons of the predicted photopeak intensity to the measured area can be performed without the need for refitting the photopeak each time. The process is illustrated in Fig. 2.16.

¹⁰Full width at tenth maximum occurs at approximately $\pm 4.3\sigma$.

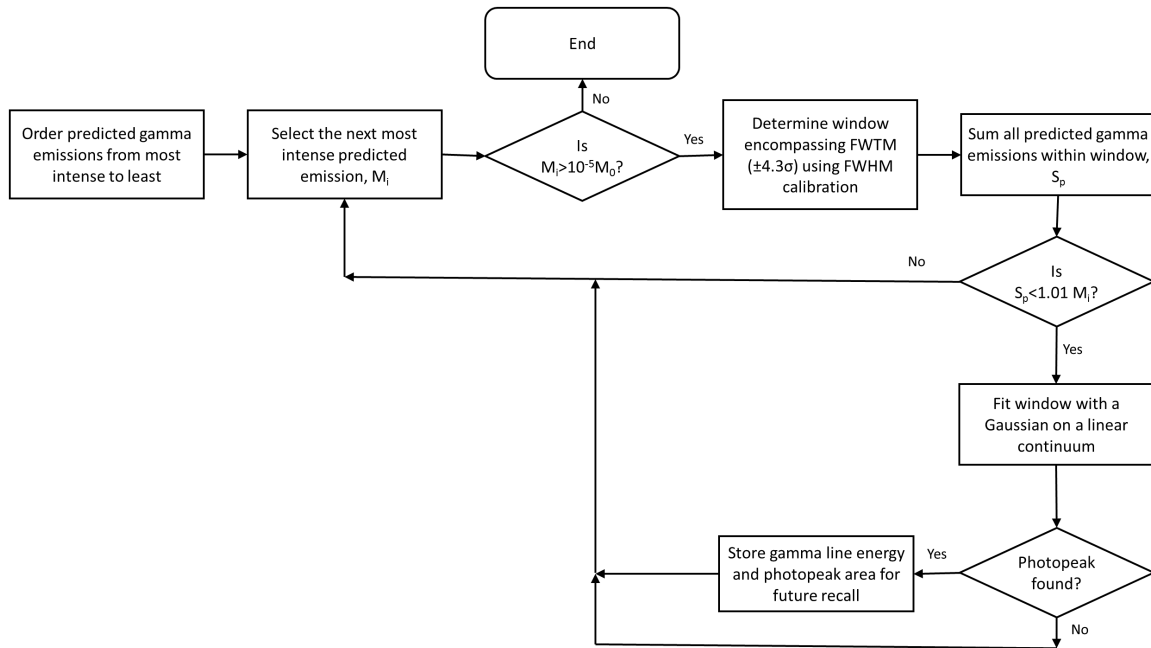


Figure 2.16 Flow chart for the mapping process.

The first FM run is used to create the gamma line to photopeak map. If the parameters used in the FM are far from the true solution, only a few peaks will be mapped while many others will be discarded. To remedy this potential problem, once the inverse solver converges to a solution, the inverse solver is restarted from the previous optimum solution to obtain an updated peak map and ensure that convergence has actually occurred. Applying this method to the ^{239}Pu spectrum taken fifty-three minutes post irradiation, twelve peaks are found. A plot of the peaks in the spectrum along with the source nuclides are shown in Fig. 2.17.

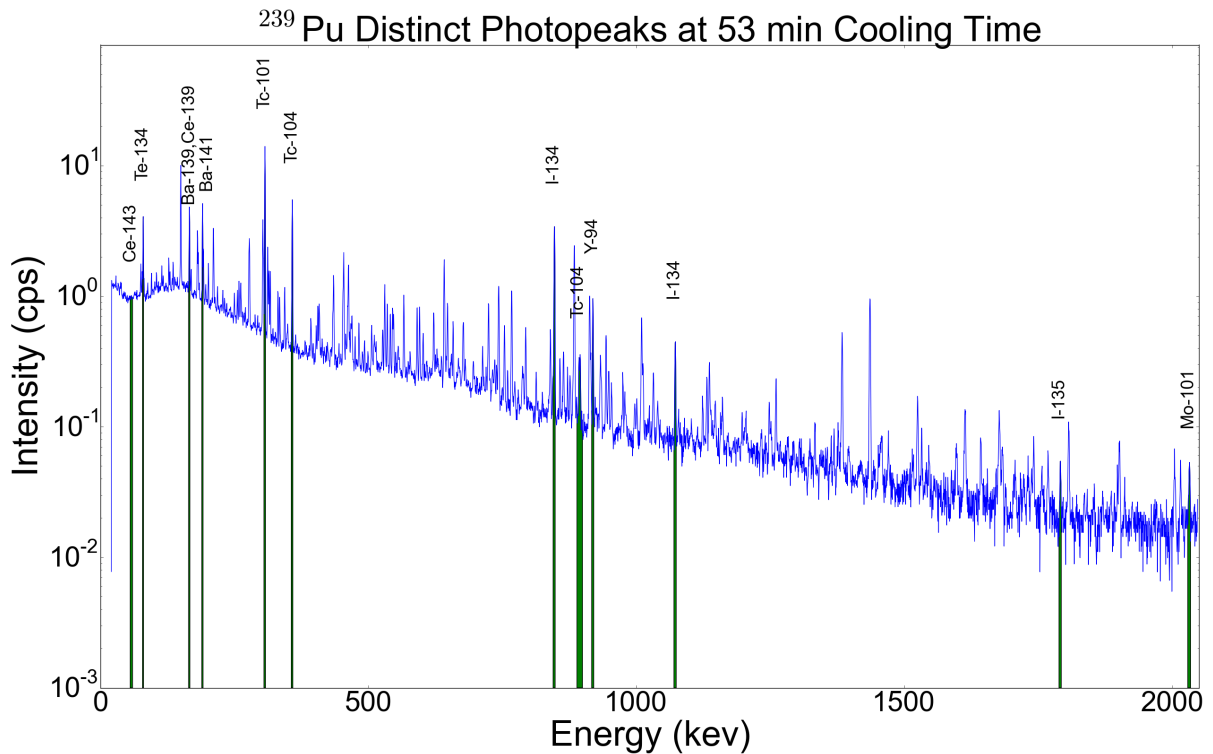


Figure 2.17 Plot of the fifty-three minute cooling time ²³⁹Pu sample with the peaks used for inverse analysis.

2.4 Inverse Analysis

In inverse analysis, a forward model is run using optimizable parameters and constants. An error metric compares the output of the forward model to the measurement being simulated. Differences between the prediction and measurement drive the changes to the parameter values until the difference between the simulation and the measurement is minimized. Changes to the parameters in the forward model cause effects that are not linear, so a nonlinear optimizer is used to determine the minimum. The optimizer may be a global or local solver, or a combination of the two. The forward model has been described previously, while the nonlinear optimizers are described in this section.

2.4.1 Nonlinear Optimization

The job of the nonlinear optimizer is to solve for a set of values x^* such that for some cost function $f(x)$ the following is true:

$$f(x^*) \leq f(x) \text{ for all } x \in U \subseteq \mathbb{R} \quad (2.19)$$

In this application, the function to be minimized is χ^2 given in Eq. (1.1) repeated here.

$$\chi^2(\mathbf{X}) = \sum_i \frac{(y_i - A(t_i; \mathbf{X}))^2}{\text{Var}_{y_i}} \quad (1.1)$$

There are many optimization algorithms to minimize Eq. (1.1), and they all fall into two main categories, global and local. An example problem will be used to demonstrate the functionality of each category of algorithm. The problem selected is one dimensional, but the methodology holds for higher dimensions. The test problem to minimize is

$$f(x) = -(1.4 - 3x) \sin(18x) \quad (2.20)$$

on the interval $x \in [0, 1.5]$. A plot of this function is shown in Fig. 2.18.

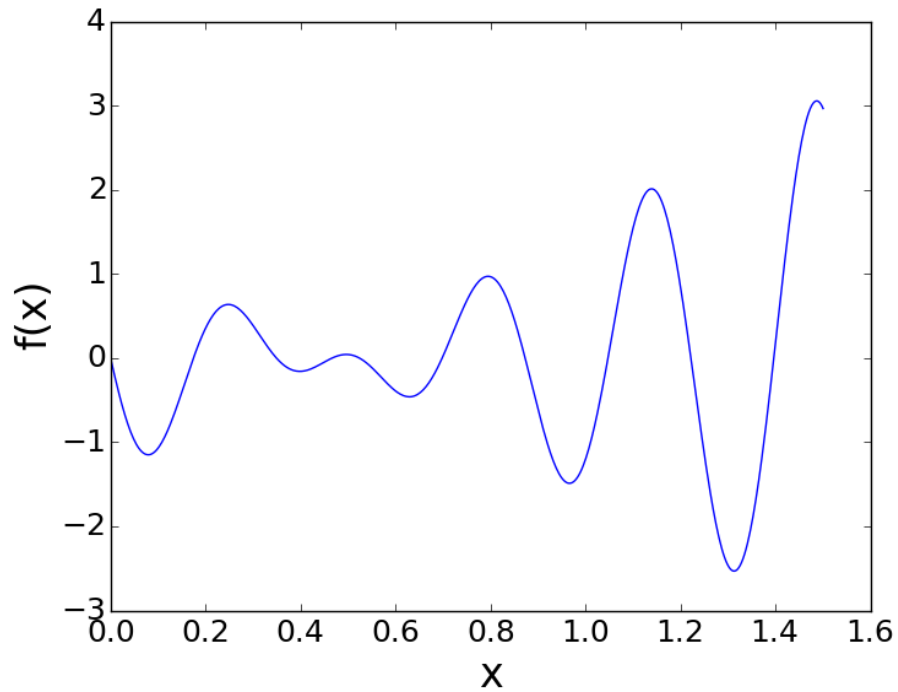


Figure 2.18 Plot of Eq. (2.20) on $x \in [0, 1.5]$.

The global minimum occurs at $(1.313, -2.532)$.

Global Search

In a global search, the entire sample space is explored and the global minimum is returned. This is useful for problems where multiple extrema exist and a local solver may miss the true global extremum. The improved search capacity has drawbacks as the computation time for a global solver is much higher than for a local solver. The function being searched by the solver must be evaluated hundreds of times, restricting the forward model to be computationally inexpensive.

Exhaustive Search

The simplest and least efficient global solver is the exhaustive search. A mesh is placed over the solution space and each point is evaluated. After a comparison of each output, the minimum point

is taken to be the solution. The computation time is directly proportional to the mesh density and inversely proportional to the likelihood of finding an extrema. A comparison of a coarse mesh and a mesh that is ten times finer, applied to the test problem, is shown in Fig. 2.19

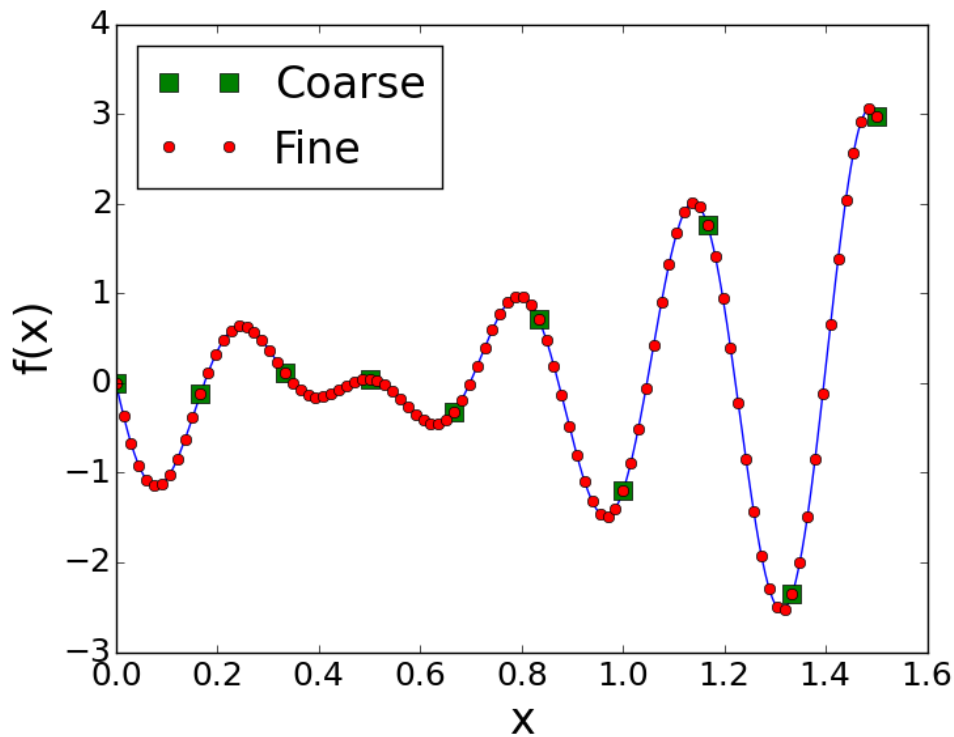


Figure 2.19 Plot of Eq. (2.20) and two different exhaustive mesh densities

The coarse mesh finds a solution of (1.33,-2.35) and the fine mesh has a minimum of (1.32, -2.52), a difference of 7% and 0.5% from the true minimum respectively. The improved solution requires ten times longer, but provides an answer that is more than ten times more accurate. For these two meshes, the coarse mesh had a serendipitous placement and could just as easily have missed the global minimum entirely, demonstrating the need for a fairly dense mesh.

Genetic Algorithm

A genetic algorithm is intended to mimic the evolutionary process in a computational way. A series of rules are followed to find the most "fit", or optimum, solution in a parameter space. The following rules describe the genetic algorithm process.

1. Creation: A series of points, called chromosomes, are created throughout the possible solution space. This is done by uniform random selection of the gene values from each gene's domain and the set of genes comprise the chromosome.
2. Sorting: The χ^2 value is calculated for each chromosome, and the resulting values are sorted from lowest χ^2 to highest.
3. Selection: Chromosomes with χ^2 values placing them in the top $k_1\%$ are kept, while the rest are discarded.
4. Breeding: From the retained chromosomes, three are selected to create a new chromosome to replace those discarded. The new chromosome will use all three parents to create a quadratic model ($y = ax^2 + bx + c$) of the error surface and select the minimum for the parameter value. This is done using the coefficient values

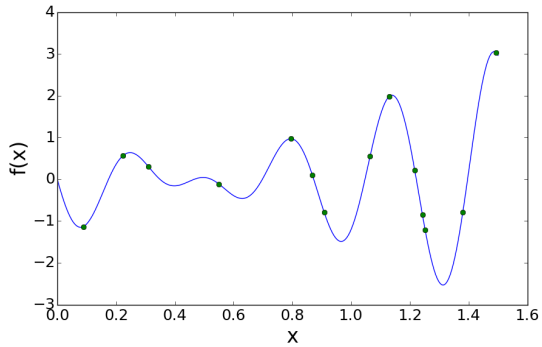
$$\begin{aligned} a &= \frac{1}{x_3 - x_2} \left[\frac{y_3 - y_1}{x_3 - x_1} - \frac{y_2 - y_1}{x_2 - x_1} \right] \\ b &= \frac{y_2 - y_1}{x_2 - x_1} - a(x_2 + x_1) \\ c &= y_1 - ax_1^2 - bx_1 \end{aligned} \tag{2.21}$$

for points $p_1 = (x_1, y_1)$, $p_2 = (x_2, y_2)$, and $p_3 = (x_3, y_3)$ where x_i is the parameter value and y_i is the associated value of χ^2 . Setting the derivative of the quadratic equal to zero and solving gives the new parameter value for the chromosome as $x_{new} = -\frac{b}{2a}$. If the quadratic has a maximum instead of a minimum, then the new chromosome will inherit a randomly selected

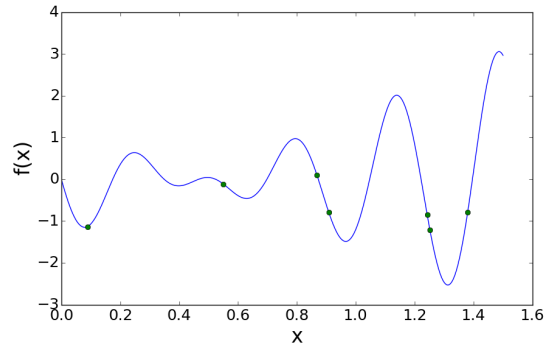
weighted average from two of the three parents. The new chromosome is created with the updated parameters and three more of the original chromosomes are selected to begin the process again.

5. Mutation: A random number, k_2 , of mutations are introduced to change the values of a chromosome. This mutation may affect each component within the chromosome or individual pieces. This process allows for the exploration of the sample space and prevents the solver from getting trapped in a local minimum.
6. Steps 2-5 correspond to one generation. If k_3 generations have occurred, return the fittest chromosome. Otherwise, return to step 2.

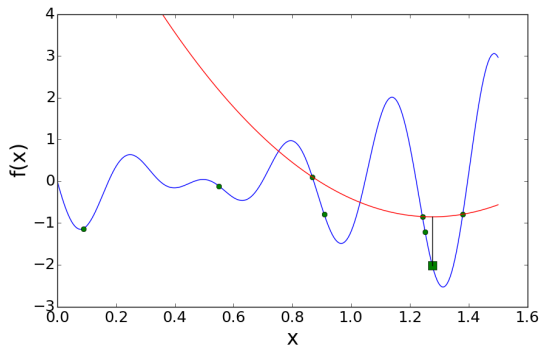
The value of k_1 is typically 50%, k_2 is 10% of the population, and k_3 is 20-40. This process is shown graphically in Fig. 2.20. The method is slow, but it samples a large portion of the parameter space and reasonably ensures the global minimum has been found.



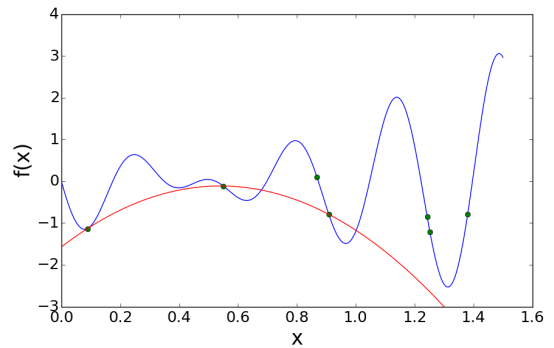
(a) Distribution of chromosomes in the first generation.



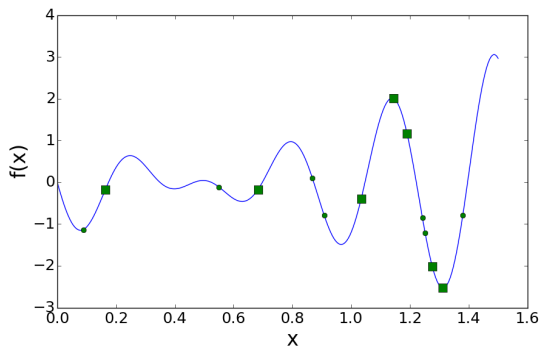
(b) Removing half the chromosomes that score the worst.



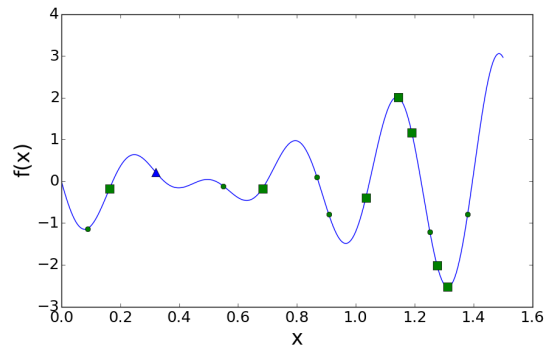
(c) The minimum of the three chromosome defined parabola is the new chromosome.



(d) The quadratic parabola has a maximum, so two chromosomes will be blended randomly.



(e) The chromosome population after mating.



(f) Mutation moves one chromosome to a new location. These points are the population after one generation.

Figure 2.20 Graphical representation of one generation of the genetic algorithm. Circles are the initial chromosome population, squares indicate new chromosome values from the quadratic breeding, and triangles represent mutations.

Markov Chain Monte Carlo

Markov Chain Monte Carlo (MCMC) is a global search algorithm that uses a stochastic process to generate states that are only dependent upon the previous state. Each sample updates the prior distribution until a posterior distribution showing the optimum location and the distribution of solutions around it has been achieved.

Several variations of the MCMC method exist, usually making changes to the proposal function or acceptance step. A commonly used variant is called Metropolis-Hastings, named after the one of the original authors of the algorithm and a statistician who extended the work to a more general form. The steps taken in the Metropolis-Hastings version of MCMC are as follows:

1. Set some initial value for $x^{(0)}$.
2. For $i = 1$ to N total samples.
 - Sample $u \sim \text{Uniform}(0,1)$
 - Sample $x^* \sim g(x^*|x^{(i)})$, the likelihood of x^* given $x^{(i)}$
 - Calculate the acceptance probability as

$$\alpha(x^*|x^{(i-1)}) = \min \left\{ 1, \frac{\pi(x^*)g(x^{(i-1)}|x^*)}{\pi(x^{(i-1)})g(x^*|x^{(i-1)})} \right\}$$

- If $u < \alpha$, $x^{(i)} = x^*$
else $x^{(i)} = x^{(i-1)}$

The function $\pi(x)$ is the (un)normalized prior probability for value x . The ratio $\frac{\pi(x^*)}{\pi(x^{(i-1)})}$ is the probability ratio of the proposed sample to the previous sample, ranking the superiority of the new sample.

For Metropolis MCMC, $g(x^{(i-1)}|x^*) = g(x^*|x^{(i-1)})$ making the acceptance criterion

$$\alpha(x^*|x^{(i-1)}) = \min \left\{ 1, \frac{\pi(x^*)}{\pi(x^{(i-1)})} \right\}.$$

This criterion is met by having $g(x|y)$ be a normal distribution where

$$g(x|y) = g(y|x) = \text{Normal}(x - y; 0, \sigma) = \text{Normal}(y - x; 0, \sigma)$$

and the value of σ determines the size of the random step for each sample.

A graph showing how the distribution moves around the sample space to the global minimum is shown in Fig. 2.21.

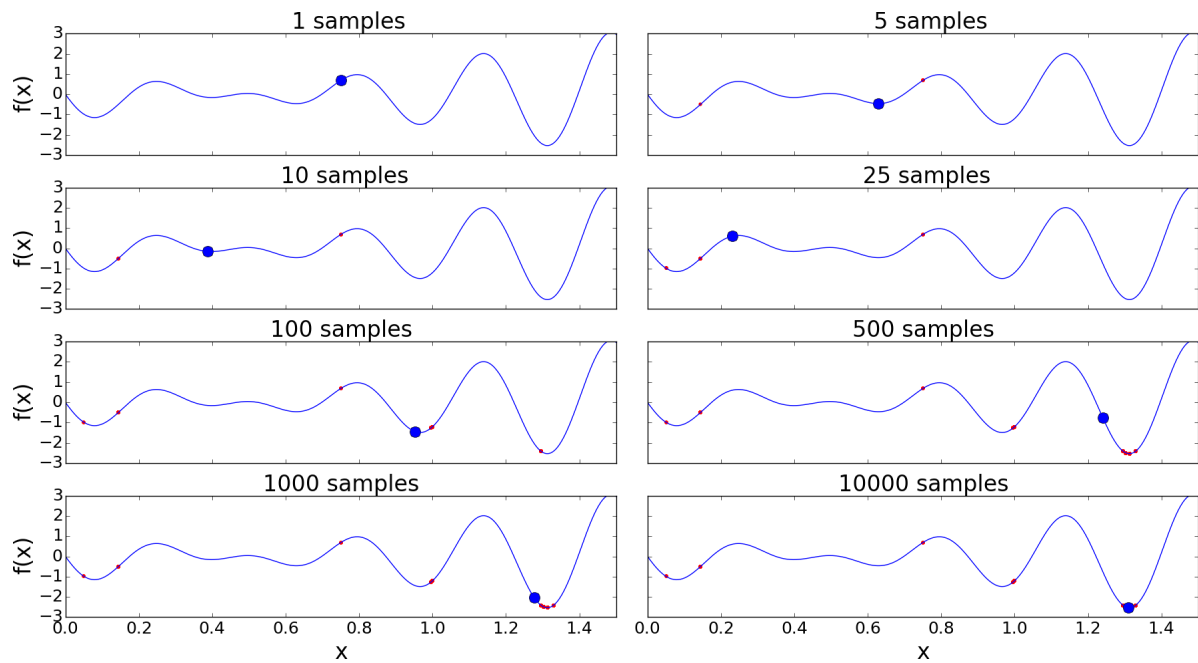


Figure 2.21 Location of accepted samples as red dots and the posterior mean as blue circle after X samples. Only a few points are accepted, though the entire sample space is explored. The mean of the posterior is calculate to be (1.312,-2.532).

Local Search

Local search methods are typically gradient based methods although a direct search method exists. Gradient based methods use derivatives to guide their search for a minimum while direct search methods do not. Levenberg-Marquardt and Gauss-Newton are examples of gradient based methods and Nelder-Mead is a direct search method. Local search methods decrease an objective function and have no methodology to look for minima outside of the one they are currently iterating towards. This focus on convergence makes them faster than global methods, but require initial guesses close to the true solution to prevent them becoming trapped in a local minimum.

Nelder-Mead

A direct, local search method is Nelder-Mead. It does not make use of gradients, but compares the vertices of an $N+1$ dimensional simplex in N dimensional space. Following a set of rules, the method will converge to a local minimum. The steps for points x_1, x_2, \dots, x_{N+1} are:

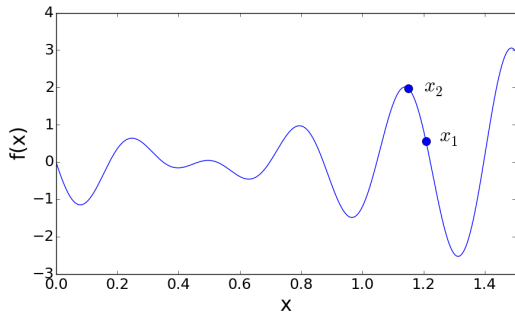
1. Arrange the values such that

$$f(x_1) \leq f(x_2) \leq \dots \leq f(x_{N+1})$$

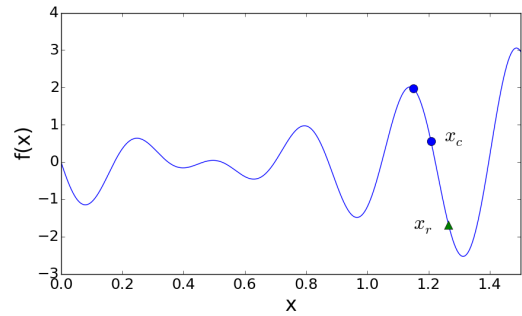
2. Find the centroid x_c of all points excluding x_{N+1} .
3. Calculate a reflected point $x_r = x_c + k_1(x_c - x_{N+1})$ for $k_1 > 0$. If $f(x_1) \leq f(x_r) < f(x_N)$ then replace x_{N+1} with x_r . Return to step 1.
4. If $f(x_r) < f(x_1)$, then expand the point as $x_e = x_c + k_2(x_r - x_c)$ for $k_2 > 0$. Then replace x_{N+1} with x_e or x_r dependent upon $\min\{f(x_e), f(x_r)\}$. Return to step 1.
5. For $f(x_r) > f(x_N)$, then contraction is used to find $x_s = x_c + k_3(x_{N+1} - x_c)$ for $0 < k_3 < 0.5$. If $f(x_s) < f(x_{N+1})$, replace x_{N+1} with x_s . Return to step 1.

6. Every point is replaced with $x_i = x_1 + k_4(x_i - x_1)$ for $i \in \{2, \dots, N + 1\}$. Return to step 1.

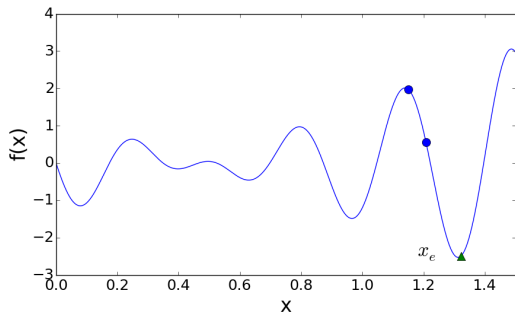
Common values for k_x are $k_1 = 1$, $k_2 = 2$, $k_3 = 0.5$, and $k_4 = 0.5$. A graphical display of this process is shown in Fig. 2.22.



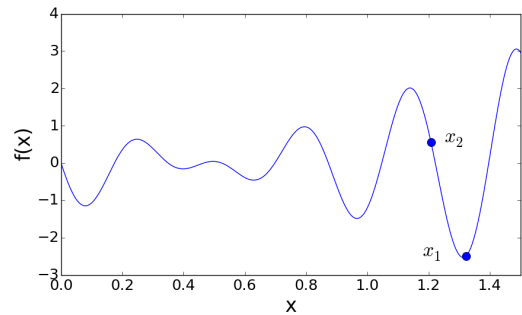
(a) Two initial points of the simplex.



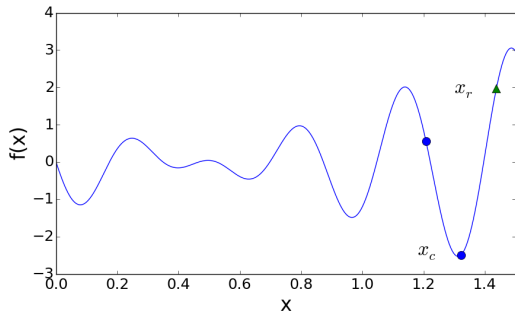
(b) Create the reflected point, x_r .



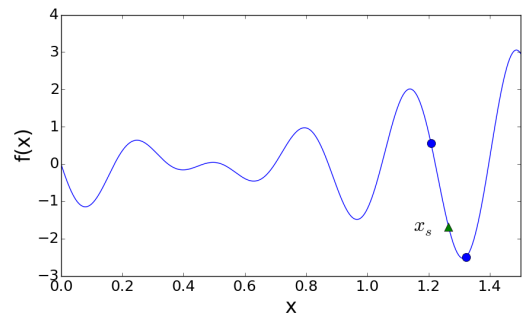
(c) The point x_r has $f(x_r) < f(x_1)$, so the expanded point x_e is created.



(d) The point x_e is accepted as the new simplex point.



(e) Create the reflected point, x_r .



(f) The point x_r has $f(x_r) > f(x_2)$, so a contraction point x_s is created.

Figure 2.22 Graphical representation of Nelder-Mead moving towards a minimum. Triangles are candidates for new points on the simplex.

Levenberg-Marquardt

Levenberg-Marquardt (LM) is an algorithm that combines gradient descent with Gauss-Newton. The algorithm was first described by Levenberg in 1944 and further generalized by Marquardt in 1963 [23],[26]. It uses an iterative procedure to move towards a local minimum, and as such needs a well informed initial guess. It functions by writing Eq. (1.1) in vector notation as

$$\chi^2(\mathbf{X}) = \mathbf{y}^T \mathbf{W} \mathbf{y} - 2\mathbf{y}^T \mathbf{W} A(\mathbf{X}) + A(\mathbf{X})^T \mathbf{W} A(\mathbf{X}) \quad (2.22)$$

where $\mathbf{W}_{ii} = 1/\sigma_{y_i}^2$ where y_i is the uncertainty in t_i .

LM iteratively updates the parameter vector \mathbf{X} through a vector step \mathbf{h}_{lm} to advance from $A(t_i; \mathbf{X})$ to $A(t_i; \mathbf{X} + \mathbf{h}_{lm})$ where the step along \mathbf{h}_{lm} minimizes Eq. (1.1)/(2.22). This minimization step is in the direction of the gradient to give

$$A(t_i; \mathbf{X} + \mathbf{h}_{lm}) \approx A(t_i; \mathbf{X}) + J_i \mathbf{h}_{lm} \quad (2.23)$$

where J_i is the column of the Jacobian matrix for peak i

$$J_i = \frac{\partial A(t_i; \mathbf{X})}{\partial \mathbf{X}} \quad (2.24)$$

Rearranging the terms of Eq. (2.23), and including the \mathbf{W} , gives the pure steepest descent step as

$$\mathbf{h}_{lm} = \alpha J_i^T \mathbf{W} (A(t_i; \mathbf{X}) - A(t_i; \mathbf{X} + \mathbf{h}_{lm})) \quad (2.25)$$

To determine the Gauss-Newton step, Eq. (2.23) is substituted into Eq. (2.22) as an updated step. The new value for Eq. (2.22) becomes:

$$\chi^2(\mathbf{X}) \approx \mathbf{y}^T \mathbf{W} \mathbf{y} + A(\mathbf{X})^T \mathbf{W} A(\mathbf{X}) - 2\mathbf{y}^T \mathbf{W} A(\mathbf{X}) - 2(\mathbf{y} - A(\mathbf{X}))^T \mathbf{W} \mathbf{J} \mathbf{h}_{lm} + \mathbf{h}_{lm}^T \mathbf{J}^T \mathbf{W} \mathbf{J} \mathbf{h}_{lm} \quad (2.26)$$

The minimum value will occur when the derivative with respect to \mathbf{h}_{lm} equals zero.

$$0 \approx -2(\mathbf{y} - A(\mathbf{X}))^T \mathbf{W} \mathbf{J} + 2\mathbf{h}_{lm}^T \mathbf{J}^T \mathbf{W} \mathbf{J} \quad (2.27)$$

which becomes

$$[\mathbf{J}^T \mathbf{W} \mathbf{J}] \mathbf{h}_{lm} = \mathbf{J}^T \mathbf{W} (\mathbf{y} - A(\mathbf{X})) \quad (2.28)$$

Levenberg introduced a damping factor to create an adjustment to make the algorithm act like Gauss-Newton when Eq. (2.22) is changing rapidly as

$$(\mathbf{J}^T \mathbf{W} \mathbf{J} + \lambda \mathbf{I}) \mathbf{h}_{lm} = \mathbf{J}^T \mathbf{W} [\mathbf{y} - A(\mathbf{X})] \quad (2.29)$$

Marquardt replaced \mathbf{I} with $\mathbf{J}^T \mathbf{J}$ to scale the each component of the gradient with the intent of increasing the step along directions with a small gradient. All of this, along with a weighting matrix \mathbf{W} , gives the following

$$[\mathbf{J}^T \mathbf{W} \mathbf{J} + \lambda \text{diag}(\mathbf{J}^T \mathbf{W} \mathbf{J})] \mathbf{h}_{lm} = \mathbf{J}^T \mathbf{W} (\mathbf{y} - A(\mathbf{X})) \quad (2.30)$$

where \mathbf{J} is the $m \times n$ Jacobian, \mathbf{W} is the diagonal matrix where \mathbf{W}_{ii} is equal to $1/\sigma_A^2$ and λ is a parameter used to determine the type of step taken. If λ is small, a Gauss-Newton step is taken, but if it is large, a conjugate-gradient step is taken.

Numerous implementation of LM exist, but SciPy was selected for ease of interface and strong validation history. This SciPy algorithm utilizes the model-trust region approach to determine the

value of λ [9]. In this method, the maximum expected successful step length δ constrains the distance that can be traveled each step. The trust region requires that $\|\mathbf{h}_{lm}\|_2 \in [\frac{3\delta}{4}, \frac{3\delta}{2}]$. The value of \mathbf{h}_{lm} is found through an iterative process that adjusts λ and converges to the optimal, constrained step length. The value of δ is initially set to a constant (100 is the recommended value) and adjusted after each step. Each step along \mathbf{h}_{lm} has a predicted reduction $\Delta\chi_p$ assuming the error surface is quadratic, and an actual reduction $\Delta\chi$. If $\Delta\chi \geq 0.75\Delta\chi_p$ then the trust region is doubled. If $\Delta\chi < 0.1\Delta\chi_p$ then the trust region is halved. Otherwise the trust region remains unchanged.

The Levenberg-Marquardt process is illustrated in Fig. 2.23.

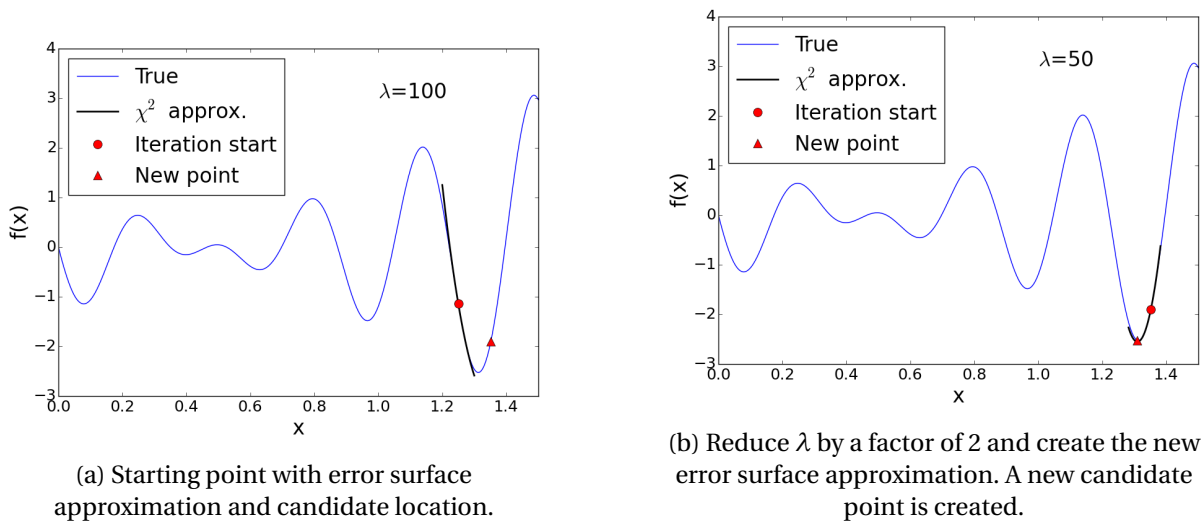


Figure 2.23 Graphical representation of Levenberg-Marquardt moving towards a minimum. Circles are accepted points and triangles are candidate points.

Hybrid Algorithm

The optimization routine primarily used in this research is composed of the previously described genetic algorithm and/or Levenberg-Marquardt. The GA was developed specifically for this appli-

cation while the SciPy [20] implementation of LM was utilized. The GA determines the solution neighborhood by running a small number of generations with a large mutation factor to explore the solution space, but not determine the optimum parameter values. Then, a LM search begins from the best point, creating an algorithm more likely to find the global minimum and converging quickly once the region of the optimum has been identified. When both the GA and LM are used it creates a hybrid genetic algorithm and Levenberg-Marquardt optimizer hence forth referred to as hGALM. The LM algorithm can be used independently if initial parameter values are sufficiently close to the true solution. Chapter 3 shows the hGALM algorithm applied to estimate:

- neutron fluence and number of fissions,
- decay time, and
- initial composition.

The peak fitting process uses the LM algorithm, because the initial parameter estimates are typically close to the final values. Any of the other optimization methods are available, but prove slower in implementation with no notable improvements in number of successful peaks fit.

CHAPTER

3

ALGORITHM APPLICATION

This section discusses the application of the preceding algorithm to the experiments conducted by PNNL. Several parameters of interest shall be discussed: fluence, cooling time, and sample composition. The estimates of fluence obtained by the algorithm will be compared to fluence wire measurements conducted by PNNL, while the estimates of cooling time will be compared to the reported measurement start times. Estimates of the original composition obtained by the algorithm will be evaluated for accuracy using synthetic spectra composed of mixtures of irradiated ^{239}Pu and ^{235}U . All results are obtained using the hybrid genetic algorithm with Levenberg-Marquardt (hGALM), unless otherwise stated.

For this research, only the gamma spectra taken from unshielded samples are used. This was

decided because the fluence and number of fission values reported with the PNNL data were in question. Fig. 2.8 and Fig. 2.9 show that the expected neutron spectra are dominated by low energy neutrons. Similarly, Fig. 2.3 shows that the cross section is largely sensitive to thermal and epithermal neutrons. The cadmium and B₄C shielding attenuate thermal and epithermal neutrons but do not increase the number of fission neutrons. Removing the low energy neutrons through shielding should result in a decrease in the number of fissions within the sample. The results from PNNL are in direct contradiction to this as shown in Table 1.1. The highest number of fissions occur for the B₄C shielding, followed by the cadmium shielding and then the bare case. No explanation for this discrepancy was provided, so this data is excluded.

3.1 Parameters

The algorithm can solve for the following parameters:

- initial composition,
- sample mass,
- irradiation flux,
- irradiation duration, and
- cooling time.

The measurement duration and the neutron spectrum are considered known.

The parameters of initial composition and sample mass are intrinsically related. Sample composition lists the constituents of the sample in absolute terms, where any of the elements can be set as a parameter. This allows for multiple components of the composition to be simultaneously optimized. The parameter of sample mass acts as a multiplier of the composition, such that if the composition is known, the total amount can be varied until an optimum is determined.

Flux and irradiation duration are the parameters related to the irradiation sequence within the reactor. Flux is the rate of neutron tracks per unit volume, and irradiation time is the duration the sample is exposed to this flux. Flux and irradiation duration can be multiplied together to compute fluence, the total number of neutrons tracks per unit volume.

The cooling time parameter accounts for natural radioactive decay of the fission products. For the neutron rich daughter products of fission, beta decay is the preferred method of decay accompanied by gamma emissions from the excited daughter product. Measurements of the gamma rays with a properly calibrated detector indicate the amount of each radionuclide present. Knowing the initial nuclide distribution from induced fission, the current nuclide concentrations, and the rate of decay for each radionuclide, allows for the determination of the cooling time.

3.2 Results

3.2.1 Single Gamma Spectrum

Fifteen gamma spectra were measured for ^{239}Pu , and fourteen spectra were measured for ^{235}U and ^{233}U at the WSU irradiation site. In this section each spectrum will be analyzed individually. The algorithm was applied to each spectrum, but the primary focus will be on ^{239}Pu because it is representative of the trends observed.

3.2.1.1 Fluence

Flux and Irradiation Time

PNNL estimated the fluence the sample was exposed to using fluence wires and estimated the number of fissions within the sample using a three group cross section as described in Sec. 1.3. The

algorithm in this dissertation uses the measured gamma spectrum to determine the irradiation flux and time, thereby providing an independent means of calculating fluence for comparison. When comparing the algorithm results to the PNNL measurements, the full hGALM algorithm was run on the same spectrum to confirm stability of the solution. This led to a variety of flux and irradiation time solutions. Each solution had a consistent, but highly uncertain value for fluence. To investigate this, just the LM portion of the algorithm was run with a range of initial values for flux and irradiation time. A selection of these values are included in Table 3.1. A wide set of initial values for flux

Table 3.1 Initial and final flux and irradiation time for a ^{239}Pu sample with 192 min cooling time.

Initial Guess			Solution		
Flux (n/cm ² s)	Irradiation Time (s)	Fluence (n/cm ²)	Flux (n/cm ² s)	Irradiation Time (s)	Fluence (n/cm ²)
4.8×10^{17}	0.0021	1.064×10^{15}	2.55×10^{17}	1.20×10^{-4}	3.048×10^{14}
2.986×10^{15}	0.10	2.986×10^{14}	2.76×10^{15}	0.110	3.048×10^{14}
8.19×10^{12}	5.0	4.095×10^{13}	5.01×10^{12}	60.6	3.033×10^{14}
				Average	3.043×10^{14}

and irradiation time were investigated, providing a range of starting fluence values. The algorithm converges to a single stable fluence value of approximately $3.04 \times 10^{14}[\text{n/cm}^2]$ with values of final flux and irradiation time varying over six orders of magnitude. This stable output is characteristic of parameter values that can not be found individually but only as a product. This leads to the result: *when flux and irradiation time can not be determined individually, it is indicative of very short duration irradiation.*

Physically, the short irradiation time of a pulsed reactor, typically 10 ms, precludes a nuclide from undergoing multiple neutron capture events. Each neutron capture creates a new nuclide with its own decay signature, and the chain of multiple captures is required to determine irradiation

duration. The concentration of nuclides born from (multiple) neutron capture events indicates flux intensity. Any sufficiently short irradiation duration minimizes multiple capture events and prohibits uniquely determining both irradiation time and flux.

The relation between flux and irradiation time can be seen in Fig. 3.1. Note that there is a continuum of minimum χ^2 values as is expected for parameters with an inverse relation. This behavior was also observed for ^{233}U and ^{235}U samples.

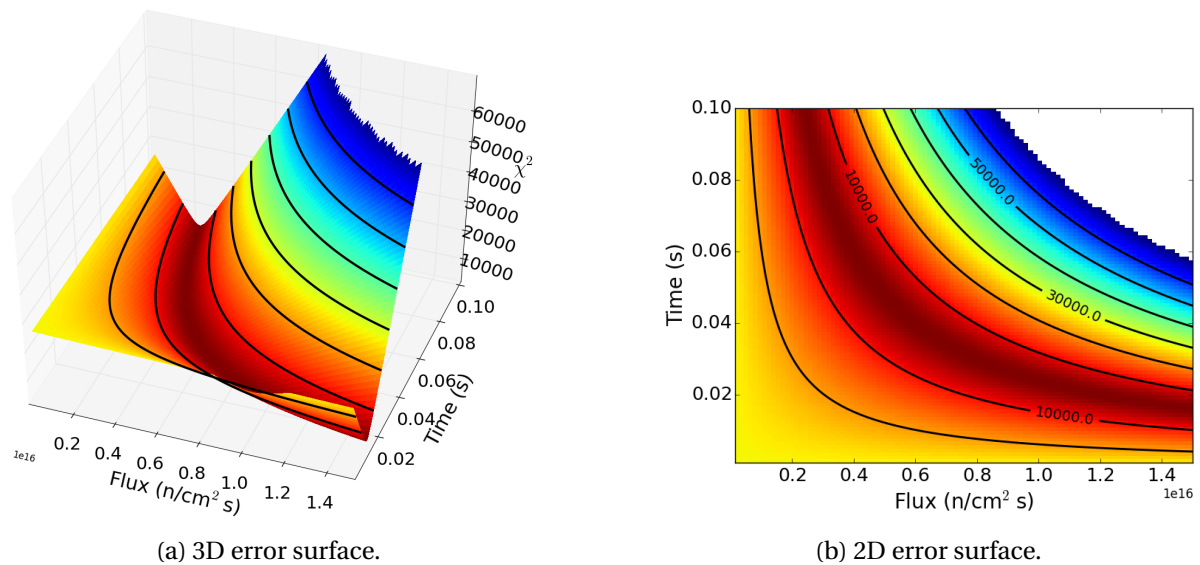


Figure 3.1 The error surface for a ^{239}Pu sample at 192 minutes cooling time for the parameters flux and irradiation time.

Fluence and Number of Fissions

Determining the number of fissions requires knowing the appropriate fission cross section, provided by COUPLE, the fluence found via the algorithm, and the sample mass. Multiplying the one group fission cross section with the fluence and sample mass gives the number of fissions in the sample. Table 3.2 compares the fluence and number of fissions calculated by the algorithm to the results from PNNL for all three nuclides.

Table 3.2 Best fit values of fluence and number of fissions compared to reported values (300K neutron spectrum).

^{239}Pu			^{235}U			^{233}U		
start	fluence $\times 10^{14}$	# of fissions	start	fluence $\times 10^{14}$	# of fissions	start	fluence $\times 10^{14}$	# of fissions
[min]	[n/cm 2]	$\times 10^8$	[min]	[n/cm 2]	$\times 10^7$	[min]	[n/cm 2]	$\times 10^8$
4	NS*	NS	4	2.04 \pm 1%	6.58 \pm 1%	4	2.05 \pm 1%	1.22 \pm 1%
9	NS	NS	10	2.95 \pm 1%	9.48 \pm 1%	11	2.47 \pm 1%	1.46 \pm 1%
15	2.73 \pm 1%	1.27 \pm 1%	15	3.00 \pm 1%	9.64 \pm 1%	17	3.14 \pm 1%	1.86 \pm 1%
20	2.69 \pm 1%	1.25 \pm 1%	20	2.95 \pm 1%	9.47 \pm 1%	23	3.07 \pm 1%	1.82 \pm 1%
31	2.67 \pm 1%	1.24 \pm 1%	31	2.97 \pm 1%	9.54 \pm 1%	34	3.02 \pm 1%	1.79 \pm 1%
42	2.73 \pm 1%	1.27 \pm 1%	41	2.94 \pm 1%	9.45 \pm 1%	44	3.08 \pm 1%	1.83 \pm 1%
53	2.72 \pm 1%	1.27 \pm 1%	52	2.95 \pm 1%	9.46 \pm 1%	57	3.02 \pm 1%	1.79 \pm 1%
69	2.73 \pm 1%	1.27 \pm 1%	68	3.14 \pm 3%	10.1 \pm 3%	73	3.02 \pm 1%	1.79 \pm 1%
84	2.77 \pm 1%	1.29 \pm 1%	83	3.02 \pm 1%	9.70 \pm 01%	89	3.07 \pm 1%	1.82 \pm 1%
100	2.71 \pm 1%	1.26 \pm 1%	99	3.04 \pm 1%	9.77 \pm 1%	106	2.96 \pm 1%	1.75 \pm 1%
131	2.65 \pm 1%	1.23 \pm 1%	129	3.16 \pm 1%	10.1 \pm 1%	137	3.04 \pm 1%	1.80 \pm 1%
162	2.67 \pm 1%	1.24 \pm 1%	160	3.25 \pm 1%	10.4 \pm 1%	168	3.15 \pm 1%	1.86 \pm 1%
192	2.69 \pm 1%	1.25 \pm 1%	220	3.25 \pm 1%	10.4 \pm 1%	229	3.15 \pm 1%	1.87 \pm 1%
253	2.87 \pm 1%	1.34 \pm 1%	280	3.08 \pm 1%	9.90 \pm 1%	291	3.15 \pm 1%	1.86 \pm 1%
313	2.85 \pm 1%	1.32 \pm 1%						
Avg	2.73 \pm 0.2%	1.27 \pm 0.2%	Avg	2.98 \pm 0.4%	9.57 \pm 0.4%	Avg	2.96 \pm 0.3%	1.75 \pm 0.3%
PNNL	2.731	1.15	PNNL	2.986	11.4	PNNL	2.88	1.70

*NS:No solution. The hGALM algorithm did not find a stable solution for fluence.

For time scales from fifteen minutes post irradiation onward, the algorithm finds a stable solution with fluence and number of fissions comparable to that found by PNNL. Times shorter than fifteen minutes result in under-predictions and in the case of ^{239}Pu , no solution. No solution was found as the large number of photopeaks caused overlapping and prevented the existence of distinct photopeaks. At longer time scales the most active radionuclides decay and the photopeaks in the spectrum are more distinct. Note that the uncertainties listed do not include the contribution of uncertainties from the nuclear data and only reflect the shape of the local error surface.

The over-prediction in number of fissions for ^{233}U and ^{239}Pu and under-prediction for ^{235}U has two probable causes. The most likely cause for the discrepancy arises from the fact that the PNNL report included an average sample mass determined numerically from the manufacture process, but the nanogram scale mass of the irradiated sample is not known. The second cause is the existence of a large resonance at low energies present for ^{233}U and ^{239}Pu that is not present for ^{235}U . PNNL adjusted the neutron spectrum to remove neutrons from thermal energies and place them in the epithermal range above 0.25eV using STAYSL. Taking neutrons from the thermal region and placing them in the epithermal region with the large resonances increased their prediction of the number of fissions. The fission cross sections for ^{233}U , ^{235}U , and ^{239}Pu are shown in Fig. 3.2. A comparison

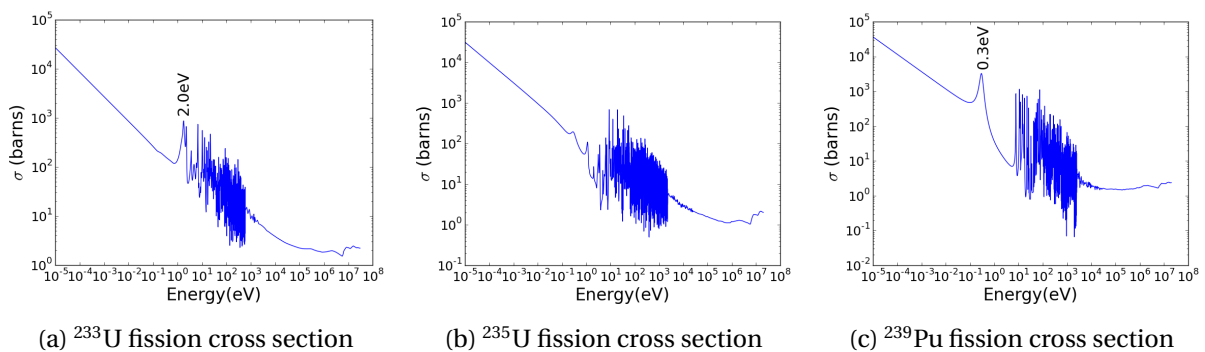


Figure 3.2 Thermal neutron induced fission cross sections for ^{233}U , ^{235}U , and ^{239}Pu .

of the measured spectrum to the spectrum created with the estimated parameters is shown in Fig. 3.3.

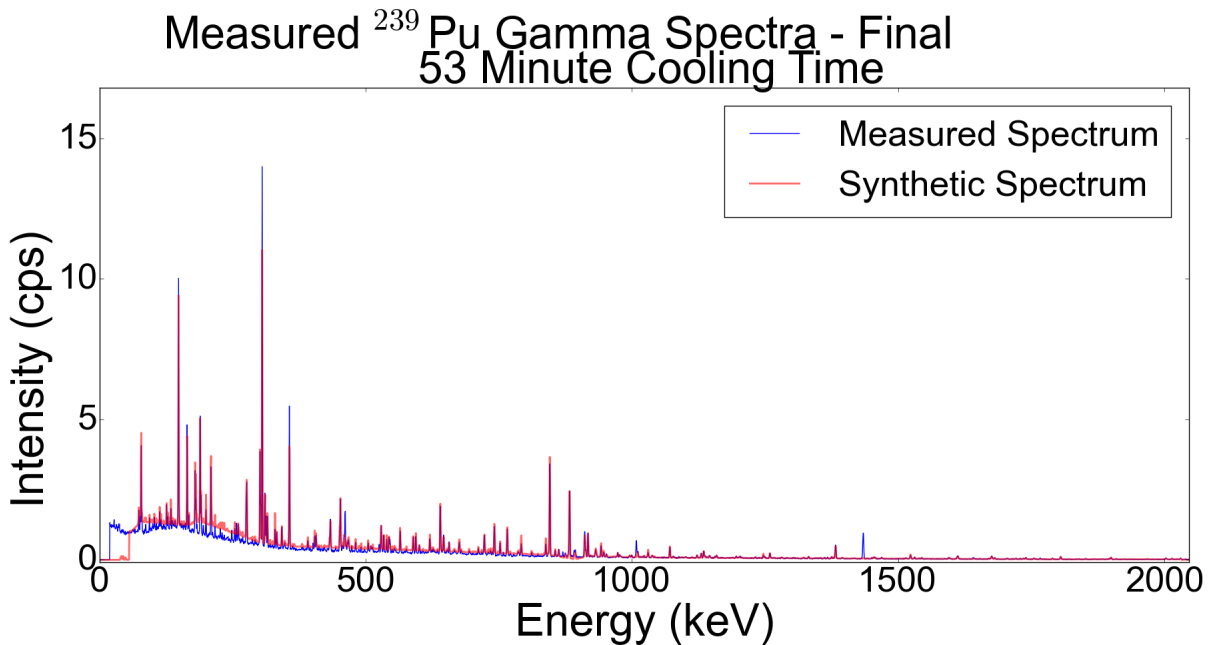


Figure 3.3 Comparison of measured to predicted gamma spectrum for fifty-three minute cooling time sample of ²³⁹Pu.

3.2.2 Other Parameters

Cooling Time

The next objective was to test the ability of the algorithm to determine other parameters. Optimizing fluence and cooling time simultaneously was selected as the first combination. The fluence value is known from the fluence wires included with each sample by PNNL, and the cooling time from the measurement start. The results of the algorithm optimizing fluence and cooling time are displayed in Table 3.3.

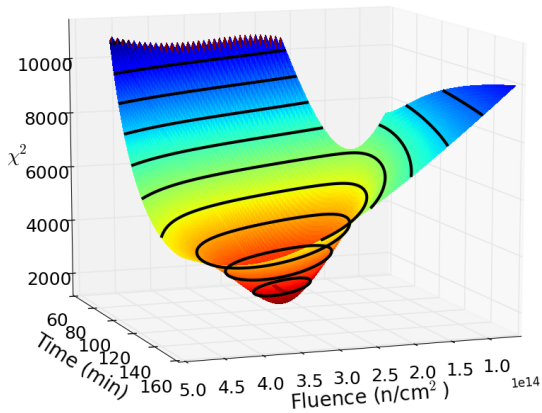
The computed parameter values are within 10% of the true and PNNL-estimated values for cooling

Table 3.3 Fluence and cooling time calculated by the algorithm for the ^{239}Pu sample. PNNL fluence value was $2.731 \times 10^{14} [\text{n}/\text{cm}^2]$. Uncertainties for each value are less than 0.1%

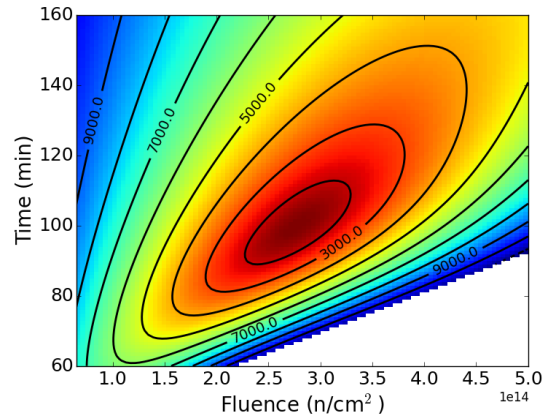
Final Fluence* (n/cm^2)	Final Cooling Time** (min)	True Cooling Time (min)
2.894×10^{14}	21.6	20
2.670×10^{14}	27.7	31
2.637×10^{14}	40.6	42
2.664×10^{14}	52.1	53
2.555×10^{14}	65.1	69
2.751×10^{14}	83.6	84
2.720×10^{14}	100.0	100
2.760×10^{14}	136.1	131
2.756×10^{14}	168.3	162
2.818×10^{14}	200.1	192
3.017×10^{14}	265.5	253
2.961×10^{14}	325.1	313

* All uncertainties less than 0.05%
** All uncertainties less than 0.2%

time and fluence respectively, demonstrating the viability of the algorithm for determining these two parameters simultaneously. No degeneracies were expected for these two parameters as each affects a different attribute. Cooling time is determined by comparison of gamma intensities from nuclides with different half lives. For a given initial nuclide inventory, particularly a nuclide inventory where each nuclide was created at effectively the same time, it is possible to use the current ratio of nuclides to determine the time since irradiation. The effect of fluence is to adjust the amount of each nuclide create and the subsequent gamma emission intensity. A plot of the error surface shows a minimum near the true value of fluence and cooling time. This can be seen in Fig. 3.4, where the minimum occurs near the value for 100 minutes of cooling time listed in Table 3.3.



(a) 3D error surface.



(b) 2D error surface.

Figure 3.4 The error surface for a ^{239}Pu sample at 100 minutes cooling time for the parameters flux and cooling time.

Sample Composition

Each sample measured was highly pure and notionally composed of only the nuclide of interest. To test the algorithm's capability to optimize initial composition, an artificial spectrum composed of two pure spectra was generated. This is possible because gamma spectra are a linear combination of the emissions from nuclides and adding two spectra is also a linear combination. To apply the algorithm to a combined spectrum composed from two different samples, each spectrum must have similar cooling times and the same detector calibrations. A mixture of ^{239}Pu and ^{235}U spectra was created in the following ratios:

- 25%-75%,
- 33%-67%,
- 50%-50%,
- 67%-33%, and
- 75%-25%.

The intention is to exploit the slight mass distribution differences shown in Fig. 2.1 to discriminate between ^{235}U and ^{239}Pu . The results for 20 minutes to 160 minutes of cooling time using this analysis are shown in Fig. 3.5.

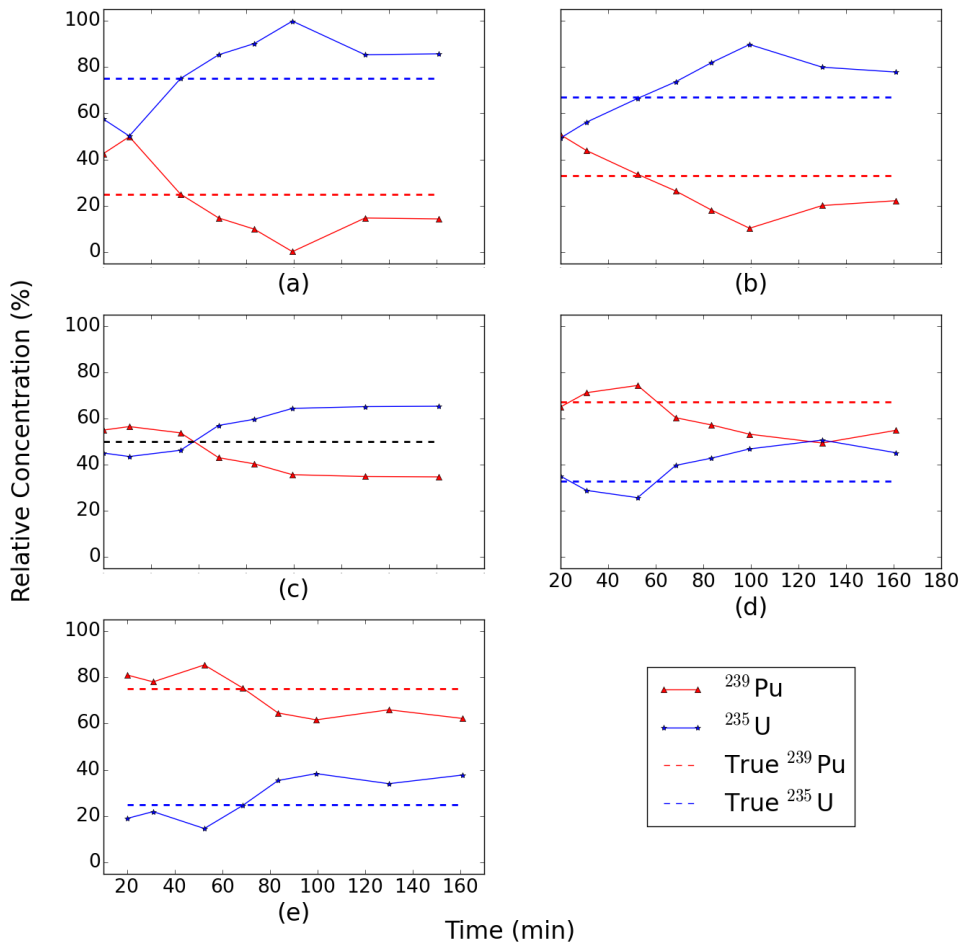


Figure 3.5 Algorithmic determination of the relative concentration of ^{239}Pu and ^{235}U for a true value of: (a) is a 25% ^{239}Pu and 75% ^{235}U mixture, (b) is a 33% ^{239}Pu and 67% ^{235}U mixture, (c) is a 50% ^{239}Pu and 50% ^{235}U mixture, (d) is a 67% ^{239}Pu and 33% ^{235}U mixture, (e) is a 75% ^{239}Pu and 25% ^{235}U mixture

The graphs show the algorithm outputs trend toward the nuclide with the larger spectrum contribution. A precise determination is desired, but the ability to determine the special nuclear material that has been irradiated is a useful metric for attribution. The coarse characterization would be fol-

lowed by more sensitive analysis using different methodology, e.g., mass spectrometry. Note that the spectrum composed of measurements taken at 42 minutes were excluded from this study because they were measured at different distances and had different absolute detector efficiency calibrations.

A plot of the error surface for when the spectrum is composed of equal contributions from ^{239}Pu and ^{235}U measured fifty-three minutes post-irradiation is shown in Fig. 3.6.

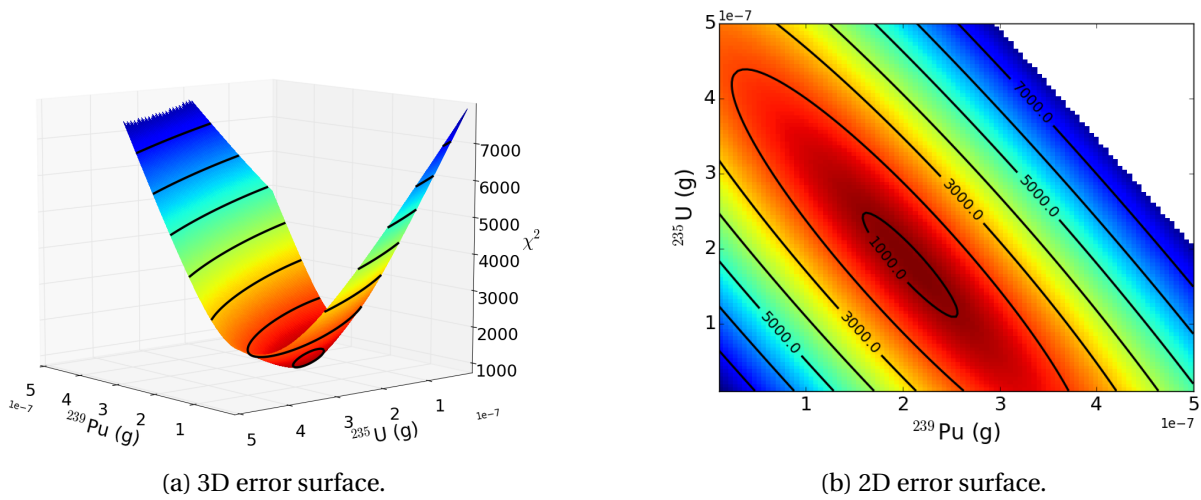


Figure 3.6 Error surface for ^{235}U and ^{239}Pu mass

There exists a minimum within the valley of the error surface near 1.85×10^{-7} grams of ^{235}U and 2.0×10^{-7} grams ^{239}Pu , which is near the true concentrations 1.75×10^{-7} grams of ^{235}U and ^{239}Pu . The discrepancy between the true value and the error surface minimum stems from the difficulty in finding photopeaks corresponding to nuclides on the edges of the mass distribution shown in Fig. 2.1. Increasing the number of photopeaks used in the inverse analysis should bring the predicted value inline with the true value. Note that the valley is not oriented at 45 degrees because plutonium has a larger cross section than uranium ($5.20078\text{E}+02$ vs. $3.56979\text{E}+02$ barns). This means that for a

constant number of fissions, a smaller mass of plutonium is needed relative to uranium.

3.3 Multiple Spectra

Previously, each spectrum was analyzed individually. Given the short cooling times, the number of distinct peaks ranged from zero, in the short cooling time cases of ^{239}Pu , to a maximum of approximately thirty photopeaks for the spectra taken six hours post irradiation. The limited number of peaks at the short time scales does cause inaccuracies as can be seen in table 3.2. Two possibilities exist to improve the results: increase the number of peaks that are fit by improving peak fitting methods, or make use of sequential measurements of the same sample to obtain photopeaks at different time scales. This second method was implemented and the results are reported in this section.

Fluence

Building on the results from the single spectrum analysis, optimizing both flux and irradiation time is problematic. For this analysis, the irradiation time is fixed at 10 ms and the flux is set as the optimizable parameter. Several different combinations of two to four spectra, along with the thirteen ^{239}Pu spectra that have distinct photopeaks, are used to demonstrate the functionality of multiple spectra analysis. The results of using multiple spectra to determine the fluence is shown in Table 3.4.

Table 3.4 Fluence and number of fissions calculated by the algorithm using multiple spectra from the ^{239}Pu sample. PNNL fluence value was $2.731 \times 10^{14} [\text{n}/\text{cm}^2]$ and underwent 1.15×10^8 fissions.

Start Times (min)	Number of Peaks	Fluence (n/cm^2)	Number of fissions
20,31	9,8	$2.678 \times 10^{14} \pm 0.06\%$	$1.246 \times 10^8 \pm 0.05\%$
20,31,53	9,8,12	$2.718 \times 10^{14} \pm 0.02\%$	$1.264 \times 10^8 \pm 0.02\%$
20,31,53,84	9,8,12,15	$2.745 \times 10^{14} \pm 0.01\%$	$1.277 \times 10^8 \pm 0.01\%$
31,131	8,20	$2.649 \times 10^{14} \pm 0.01\%$	$1.232 \times 10^8 \pm 0.01\%$
84,131	15,20	$2.670 \times 10^{14} \pm 0.01\%$	$1.242 \times 10^8 \pm 0.006\%$
84,131,192	15,20,26	$2.684 \times 10^{14} \pm 0.01\%$	$1.249 \times 10^8 \pm 0.003\%$
84,131,192,313	15,20,26,32	$2.764 \times 10^{14} \pm 0.01\%$	$1.286 \times 10^8 \pm 0.002\%$
15,20,31,42,53,69,84, 100,131,162,192,253,313	6,9,8,12,12,15,15, 23,20,21,26,32,32	$2.784 \times 10^{14} \pm 0.002\%$	$1.295 \times 10^8 \pm 0.002\%$

Increasing the number of spectra used has a corresponding increases in the number of photopeaks used by the algorithm. The added photopeaks do not affect the *accuracy* of the solution, but they do increase the *precision*. A visible comparison of the algorithm output to the measurement for three spectra is shown in Fig. 3.7.

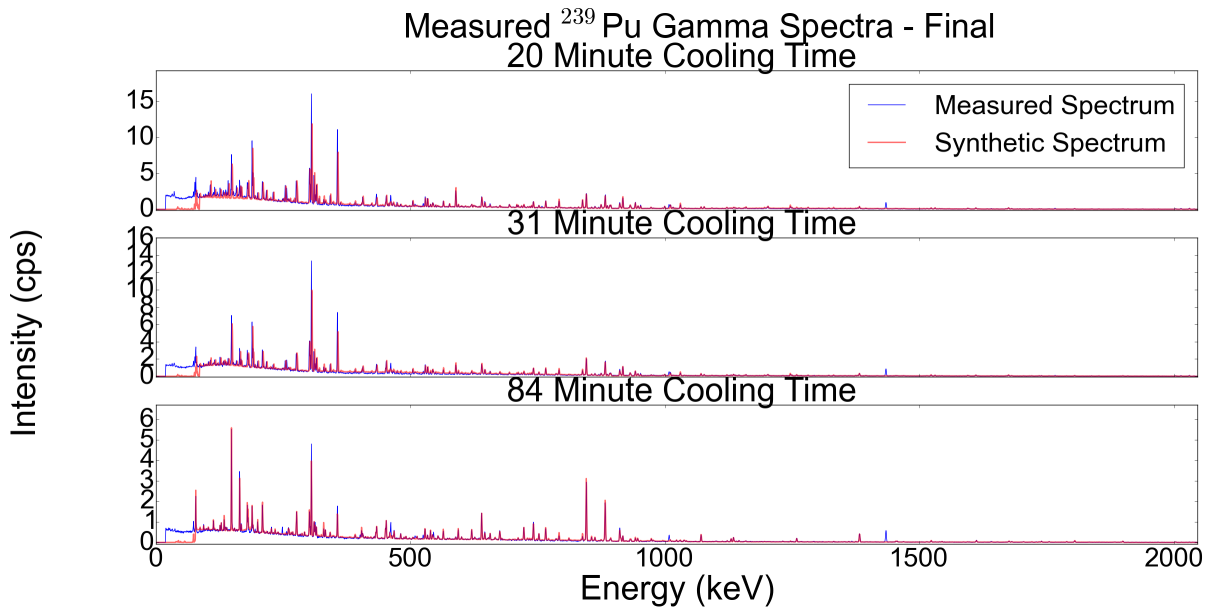


Figure 3.7 Optimizing fluence using spectra taken at 20, 31, and 84 minutes cooling time.

Cooling Time

The ability of the algorithm to determine sample fluence and cooling time was tested using two to four spectra in various combinations, along with all spectra together. The results are displayed in Table 3.5. The cooling time listed is the time from irradiation until the start of the first measurement as determined by the algorithm.

The use of multiple spectra corrects the under prediction of issue that was present in Table 3.3 at short cooling times. When spectra with long cooling times are used, an over prediction in the cooling time continues to occur. Using the spectra taken at 20 and 31 minutes cooling time, the calculated cooling time is correct. Using the 31 and 131 minute cooling time causes a 15% over prediction. The same effect is seen when the 192 minute spectrum is added to the 84 and 131 spectra, or when the 192 and 253 minute spectra are used together. Overall, the use of multiple spectra creates a more

Table 3.5 Fluence and number of fissions calculated by the algorithm using multiple spectra from the ^{239}Pu sample. PNNL fluence value was $2.731 \times 10^{14} [\text{n}/\text{cm}^2]$.

Start Times (min)	Number of Peaks	Fluence (n/cm^2)	Cooling Time (min)
20,31	9,8	$2.686 \times 10^{14} \pm 0.07\%$	$20.33 \pm 0.13\%$
20,31,53	9,8,12	$2.676 \times 10^{14} \pm 0.03\%$	$19.29 \pm 0.06\%$
20,31,53,84	9,8,12,15	$2.721 \times 10^{14} \pm 0.02\%$	$19.52 \pm 0.04\%$
31,131	8,20	$2.748 \times 10^{14} \pm 0.02\%$	$35.60 \pm 0.06\%$
84,131	15,20	$2.664 \times 10^{14} \pm 0.01\%$	$83.78 \pm 0.01\%$
84,131,192	15,20,26	$2.786 \times 10^{14} \pm 0.005\%$	$89.83 \pm 0.005\%$
84,131,192,313	15,20,26,32	$2.767 \times 10^{14} \pm 0.003\%$	$84.17 \pm 0.003\%$
192,253	27,32	$2.936 \times 10^{14} \pm 0.005\%$	$203.6 \pm 0.004\%$
15,20,31,42,53,69,84, 100,131,162,192,253,313	6,9,8,12,12,15,15, 23,20,21,26,32,32	$2.876 \times 10^{14} \pm 0.002\%$	$26.42 \pm 0.002\%$

precise and accurate estimate of cooling time and fluence compared to single spectrum analysis.

Fig. 3.8 displays two of the spectra used in the analysis along with the measured spectra they are simulating.

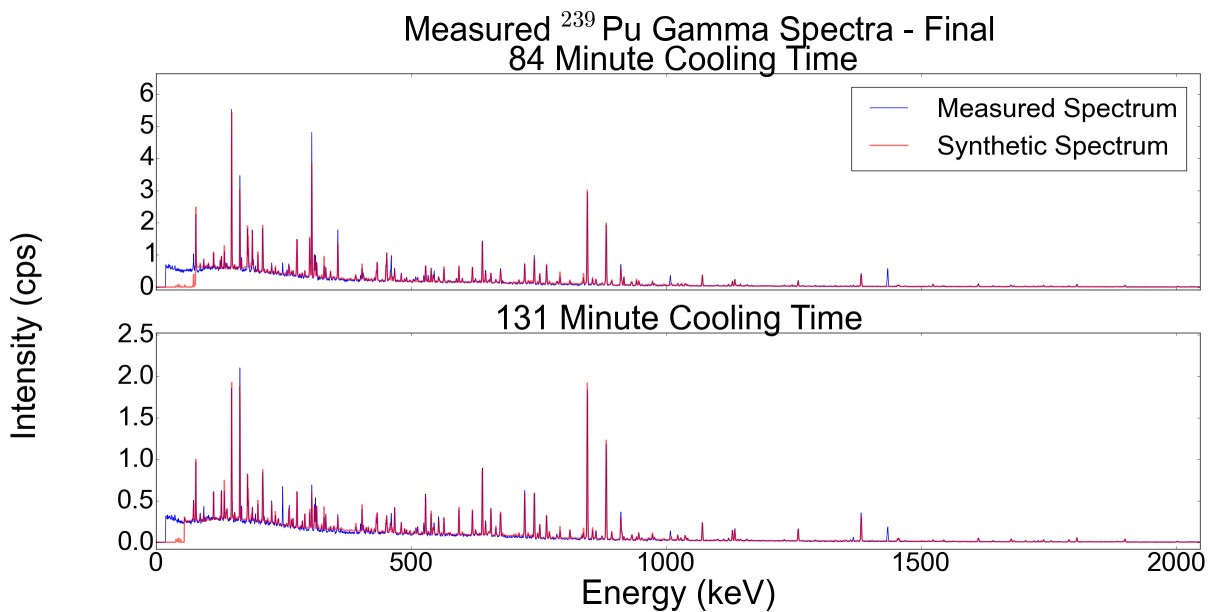


Figure 3.8 Optimizing fluence and cooling time using spectra taken at 84 and 131 minutes cooling time.

Sample Composition

The same contribution amounts used in the single spectrum analysis will be used for the multiple spectra analysis. Differing combinations of measurement start times and sample mixtures are shown in Table 3.6.

The algorithm continues to over-predict the amount of ^{235}U in the sample. The addition of extra spectra reduces the over-prediction from 15% to 10%. For all blend mixtures other than 50/50, the correct isotope was listed as having the larger contribution. A plot showing the predicted and measured spectra is shown in Fig. 3.9.

Table 3.6 Comparison of composition ratios found by the algorithm to the true ratio value for various numbers of spectra and blend ratios.

Start Times (min)	Number of Peaks	True Ratio $^{239}\text{Pu}/^{235}\text{U}$	Final Ratio $^{239}\text{Pu}/^{235}\text{U}$	σ %
20,31	10,12	25/75	45.17/54.83	± 0.05
20,31,84	10,12,21	25/75	21.34/78.66	± 0.02
20,31,84,131	10,12,21,22	25/75	17.02/82.98	± 0.01
20,31,53,69,84,100,131	11,13,16,20,21,23,22	25/75	16.11/83.89	± 0.006
20,31	10,9	33/67	46.61/53.39	± 0.06
20,31,53	10,9,15	33/67	35.04/64.96	± 0.02
20,31,53,131	10,9,15,22	33/67	25.22/74.78	± 0.01
20,31,53,69,84,100,131	10,9,15,19,19,22,22	33/67	23.20/76.80	± 0.007
31,53	9,12	50/50	54.55/45.45	± 0.02
20,31,53	7,9,12	50/50	54.76/45.24	± 0.02
20,31,53,100	7,9,12,22	50/50	40.74/59.26	± 0.01
20,31,53,69,84,100,131	7,8,13,16,19,22,22	50/50	39.76/60.24	± 0.006
20,31,53,69,84,100,131	9,9,12,15,19,20,21	67/33	56.25/43.75	± 0.008
20,31,53,69,84,100,131	8,9,13,16,18,20,22	75/25	66.39/33.61	± 0.006

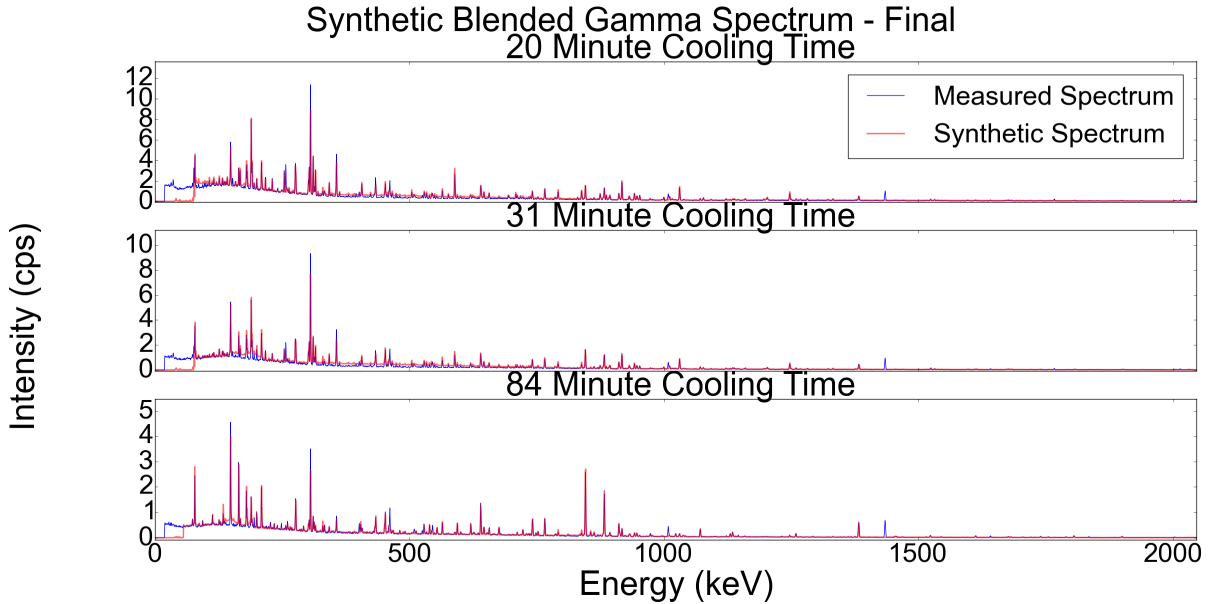


Figure 3.9 25/75 $^{239}\text{Pu}/^{235}\text{U}$ blend at 20, 31, and 84 minutes cooling time.

The principle observations from these results are:

- pulse irradiation results in flux and irradiation time not being uniquely identifiable,
- the optimized values calculated by the algorithm are in agreement to the results from PNNL,
- increasing the number of photopeaks used in the optimization process through the addition of multiple spectra, increases the precision of the solution without affecting the result values.

CHAPTER

4

CONCLUSIONS

This dissertation has presented an algorithm to estimate the history of pulse irradiated special nuclear material using gamma spectroscopy. Previous work in analyzing irradiated nuclear material primarily focused on spent nuclear fuel with long cooling times. These long time scales leave a small number of long-lived gamma ray emitting nuclides, necessitating the use of other analysis methods such as mass spectrometry. The previous work using gamma spectroscopy has made minimal use of a detector response function. Most notably, the new algorithm pairs a global nonlinear solver with a forward model, including a detector response function, to analyze short cooling time irradiated special nuclear material.

The algorithm was applied to measurements taken by PNNL of pulse irradiated special nuclear

material with cooling times ranging from minutes to hours. A comparison of the algorithm results to those provided by PNNL showed the fluence and cooling time could be determined to within 10% of the values reported using traditional activation-based methods. A spectrum comprised of various weighted spectra from pure ^{235}U and ^{239}Pu samples was tested to determine the relative contribution from each sample. The algorithm showed a bias in over predicting the amount of ^{235}U relative to ^{239}Pu , but it provided an indication of the predominant nuclide.

Strict criteria were put in place for accepting a photopeak fit used in the inverse analysis process. Each spectrum analyzed had a limited number of distinct photopeaks. To increase the number of photopeaks for analysis, multiple spectra from the same sample were analyzed as a time correlated series. The use of multiple spectra with different cooling times from the same sample, did not change the estimated fluence, cooling time, or sample composition relative to using a single spectrum but it did decrease the uncertainty associated with the estimated parameters. Another finding of this research is that for pulse irradiated materials, flux and irradiation time can not be uniquely determined, only their product (fluence) can be estimated. When these two quantities can not be determined uniquely, it is indicative of a sample that has undergone pulse irradiation, an event unique to pulse generators and research reactors. This fact is useful in identifying provenance of material.

The algorithm presented can not provide a detailed nuclide composition, but can provide a coarse characterization. The ability to determine fluence and cooling time at short time scales, combined with the previous work at long time scales by Dr. Grogan and Dr. Weber using INDEPTH, demonstrate the ability to determine basic irradiation characteristic from minutes to months post irradiation using gamma spectroscopy. This analysis is useful to quickly provide information about a radioactive sample using in-situ measurements.

The algorithm can be improved with an upgrade to the peak fitting method to account for overlapping peaks. The use of more photopeaks increases the probability that one peak will be highly dependent on the initial composition, and improve the ability of the algorithm to determine sample composition. The ideal improvement would be the use of full spectrum analysis to account for Compton continuum and escape peaks. Testing the algorithm against new measurements of irradiated special nuclear material in various shielding configurations, or the application of the algorithm against non-fissionable samples, will further extend its functionality. The gamma spectra should use the maximum number of channels available, as the 4096 channels over 2 MeV energy range used in this research meant each photopeak had approximately a dozen channels available for fitting, which contributed substantially to the uncertainties in the estimated photopeak areas.

In summary, an algorithm has been developed for the inverse analysis of irradiated special nuclear material with short cooling times that incorporates a detector response function, a global nonlinear solver, and the ability to analyze sequential spectra. The algorithm is capable of determining the cooling time and fluence of the pulse irradiated nuclear material coarsely characterize the sample's original composition. This functionality will allow for rapid in situ analysis to determine the provenance of interdicted material.

BIBLIOGRAPHY

- [1] Adewuya, A. *New methods in genetic search with real-valued chromosomes*. 1993.
- [2] Ambartsumian, V. A. *Ambartsumian's View on Astronomy of XX century: Epilogue*.
- [3] Argoul, P. "Overview of Inverse Problems, Parameter Identification in Civil Engineering" (2012), pp. 1–13.
- [4] Badrun, N. et al. "Transient behavior studies of TRIGA core for variations in reactor kinetics". *Annals of Nuclear Energy* **85** (2015), pp. 394–397.
- [5] Baxter, P. *The False Hope of Nuclear Forensics? Assessing the Timeliness of Forensics Intelligence*. 2015.
- [6] Bell, M. J. *ORIGEN - The ORNL Isotope Generation and Depletion Code*. Tech. rep. 1973, pp. 7–8.
- [7] Borio Di Tigliole, A. et al. "TRIGA reactor absolute neutron flux measurement using activated isotopes". *Progress in Nuclear Energy* **70** (2014), pp. 249–255.
- [8] Broadhad, B L; Weber, C. F. *Validation of Inverse Methods Applied to Forensic Analysis of Spent Fuel*. Tech. rep. 2015, pp. 1–6. arXiv: arXiv:1011.1669v3.
- [9] Dennis, J. E. & Schnabel, R. B. *Globally Convergent Modifications of Newton's Method*. 1996.
- [10] Erin C Finn et al. "Methods to Collect , Compile , and Analyze Observed Short-lived Fission Product Gamma Data". September (2011).
- [11] Fagerholm, R. "Safeguards at research reactors : Current practices , future directions". *International Atomic Agency Bulletin* **38.4** (1996), pp. 20–24.
- [12] Favorite, J. a. et al. "Surface and Volume Integrals of Uncollided Adjoint Fluxes and Forward-Adjoint Flux Products". *Nuclear Science and Engineering* **163** (2009), pp. 73–84.
- [13] Finn, E. C. et al. *Observed neutron fluences table and pulse times*. 2011.
- [14] Gauld, I. & Francis, M. *Investigation of Passive Gamma Spectroscopy to Verify Spent Nuclear Fuel Content*. Tech. rep. 2013. arXiv: arXiv:1011.1669v3.
- [15] General Atomics. *TRIGA@ Nuclear Reactors*. 2015.
- [16] Grogan, B. "Fiscal Year 2014 INDEPTH Analysis of Clab PWR Assemblies" (2014).
- [17] Grogan, Brandon; Weber, C. *ORNL Inverse Analysis with INDEPTH TASK 8: Calculate IE, CT, BU presentation*. 2014.

- [18] Helmer, R. G. & Lee, M. A. “Analytical functions for fitting peaks from Ge semiconductor detectors”. *Nuclear Instruments and Methods* **178.2-3** (1980), pp. 499–512.
- [19] IAEA. *IAEA Research Reactor Database*. 2016.
- [20] Jones, E. et al. *SciPy: Open source scientific tools for Python*.
- [21] Khoo, K. S. et al. “Determination of thermal to epithermal neutron flux ratio (f), epithermal neutron flux shape factor (??) and comparator factor (Fc) in the Triga Mark II reactor, Malaysia”. *Journal of Radioanalytical and Nuclear Chemistry* **271.2** (2007), pp. 419–424.
- [22] Lee, B. & Schmerler, D. “CNS Global Incidents and Trafficking Database”. March (2016), pp. 1–22.
- [23] Levenberg, K. “A Method for the Solution of Certain Non-Linear Problems in Least Squares”. *Quarterly of Applied Mathematics* **2.2** (1944), pp. 164–168.
- [24] Lewis, E. E. *Fundamentals of Nuclear Reactor Physics*. 1st. London: Elsevier Inc., 2008, p. 280.
- [25] Longoria, L. C. et al. “Analytical peak fitting for gamma-ray spectrum analysis with Ge detectors”. *Nuclear Inst. and Methods in Physics Research, A* **299.1-3** (1990), pp. 308–312.
- [26] Marquardt, D. W. “An Algorithm for Least-Squares Estimation of Nonlinear Parameters”. *Journal of the Society for Industrial and Applied Mathematics* **11.2** (1963), pp. 431–441.
- [27] Mele, I. et al. “Triga Mark II Benchmark Experiment, part II:Pulse Operation”. *Nuclear Technology* **105** (1994), pp. 52–58.
- [28] Metz, L. A. et al. “Experimental measurements of short-lived fission products from uranium, neptunium, plutonium and americium”. *Journal of Radioanalytical and Nuclear Chemistry* **282.2** (2009), pp. 373–377.
- [29] Moody, K. J. et al. *Nuclear Forensic Analysis*. Boca Raton, FL: CRC Press, 2005.
- [30] Mozin, V. “Delayed Gamma-Ray Assay for Nuclear Safeguards”. *PhD Proposal* **1** (2011). arXiv: arXiv:1011.1669v3.
- [31] Nelder, J. et al. “A simplex method for function minimization”. *Computer Journal* **7.4** (1965), pp. 308–313.
- [32] ORNL. “Scale : A Comprehensive Modeling and Simulation Suite for Nuclear Safety Analysis and Design”. *Ornl/Tm-2005/39* June (2011).

- [33] Park, K. J. et al. “Determination of burnup and Pu/U ratio of PWR spent fuels by gamma-ray spectrometry”. *Nuclear Engineering and Technology* **41.10** (2009), pp. 1307–1314.
- [34] Payne, R. F. et al. “Neutron fluence and energy reproducibility of a 2-dollar TRIGA reactor pulse”. *Journal of Radioanalytical and Nuclear Chemistry* **282.1** (2009), pp. 59–62.
- [35] Robert, C. & Casella, G. “A Short History of Markov Chain Monte Carlo: Subjective Recollections from Incomplete Data”. *Statistical Science* **26.1** (2011), pp. 102–115. arXiv: arXiv:0808.2902v7.
- [36] Silagadze, Z. K. “A new algorithm for automatic photopeak searches”. *Nuclear Instruments and Methods in Physics Research, Section A: Accelerators, Spectrometers, Detectors and Associated Equipment* **376.3** (1996), pp. 451–454. arXiv: 9506013v1 [arXiv:hep-ex].
- [37] Skutnik, S. E. & Davis, D. R. “Characterization of the non-uniqueness of used nuclear fuel burnup signatures through a Mesh-Adaptive Direct Search”. *Nuclear Instruments and Methods in Physics Research, Section A: Accelerators, Spectrometers, Detectors and Associated Equipment* **817** (2016), pp. 7–18.
- [38] Sternat, M. R. et al. “Development of Technical Nuclear Forensics for Spent Research Reactor Fuel”. PhD thesis. Texas A&M University, 2012.
- [39] Weber, C. F. & Broadhead, B. L. “Inverse Depletion/Decay Analysis Using the SCALE Code System”. *New York* (2008), pp. 4–5.
- [40] Weber, C. F. et al. “Inverse Solutions in Spectroscopic Analysis with Applications to Problems in Global Safeguards” (2008).
- [41] Willman, C. *Applications of Gamma Ray Spectroscopy of Spent Nuclear Fuel for Safeguards and Encapsulation*. 2006.

APPENDIX

APPENDIX

A

RAY TRACER

Radiation transport comes in two major classes: stochastic and deterministic. Ray tracers have been developed using each method, tracking the path of photons that leave the source medium and travel, without collision, to the detector. Each method will be described in this appendix. The general layout being simulated is shown in Fig. A.1.

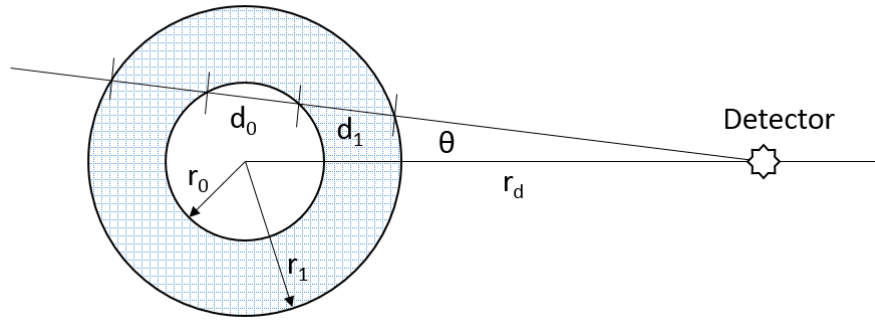


Figure A.1 Arrangement of layers for a sphere of radioactive material with a single layer of shielding.

A.1 Deterministic

The deterministic ray tracer was developed using work by Favorite [12]. The uncollided flux at the detector is given by:

$$\phi(r_d) = \frac{1}{2} \int_0^{\theta_{max}} d\theta \sin(\theta) \frac{q(1 - e^{-\Sigma_0 d_0(\theta)})}{\Sigma_0} \prod_{i=1}^N e^{-\Sigma_i d_i(\theta)} = \int_0^{\theta_{max}} d\theta f(\theta) \quad (\text{A.1})$$

where

$$\theta_{max} = \sin^{-1} \left(\frac{r_0}{r_d} \right)$$

$$d_0(\theta) = 2\sqrt{r_0^2 - r_d^2 \sin^2 \theta}$$

$$d_i(\theta) = \sqrt{r_1^2 - r_d^2 \sin^2 \theta} - \sqrt{r_{i-1}^2 - r_d^2 \sin^2 \theta}$$

Σ_i = is the macroscopic cross section for region i

$$f(\theta) = \frac{1}{2} \sin(\theta) \frac{q(1 - e^{-\Sigma_0 d_0(\theta)})}{\Sigma_0} \prod_{i=1}^N e^{-\Sigma_i d_i(\theta)}$$

The composite Simpson's rule listed in Eq. A.2 is used calculate the integral in Eq. A.1.

$$\int_a^b d\theta f(\theta) \approx \frac{h}{3} \left[f(\theta_0) + 2 \sum_{j=1}^{k/2-1} f(\theta_{2j}) + 4 \sum_{j=1}^{k/2} f(\theta_{2j-1}) + f(\theta_k) \right] \quad (\text{A.2})$$

where

$$a = 0$$

$$b = \theta_{max}$$

$$h = \frac{\theta_{max}}{k}$$

$$\theta_i = i h \text{ for } i = 0, 1, \dots, k$$

$$k = \text{number of subdivisions}$$

A.2 Stochastic

The stochastic ray tracer was developed to expand the functionality of the deterministic ray tracer. The stochastic variant is capable of modeling spheres and cylinders, providing for an increased number of options in describing the geometry of a source and the shielding material. Equations describing the initial gamma source location, the streaming path, and the entrance and exit locations for each layer will be described.

A.2.1 Spherical

The equations to determine the initial source location for k spherical shells, are:

$$\begin{aligned}
 r &= ((r_{i+1}^3 - r_i^3)\lambda_1)^{1/3} + r_i \\
 \theta &= 2\pi\lambda_2 \\
 \phi &= \cos^{-1}(2\lambda_3 - 1) \\
 x &= r \sin(\phi) \cos(\theta) \\
 y &= r \sin(\phi) \sin(\theta) \\
 z &= r \cos(\phi) \\
 \lambda_x &= U[0, 1]
 \end{aligned} \tag{A.3}$$

where $r_{i+1} > r_i \geq 0$ for $i = -1, 0, 1, \dots, k-1$ and $r_{-1} = 0$.

The source point shall be described as $\vec{S} = [x, y, z]$ and the detector located at $\vec{D} = [r_d, 0, 0]$, where $[0, 0, 0]$ is the center of the sphere and $r_d > r_k$. The distance from the detector to the source point is the distance formula given in Eq. A.4

$$d = \|\vec{S} - \vec{D}\| = \sqrt{\|\vec{S}\|^2 + \|\vec{D}\|^2 - 2\vec{S} \cdot \vec{D}} = \sqrt{(x - r_d)^2 + y^2 + z^2} \tag{A.4}$$

with direction

$$\vec{L} = \frac{\vec{S} - \vec{D}}{d} \tag{A.5}$$

The travel path from the source to the detector is given as

$$\vec{P}(t) = \vec{S} + t\vec{L}, t \geq 0 = \begin{cases} x(t) = S_x + tD_x \\ y(t) = S_y + tD_y \\ z(t) = S_z + tD_z \end{cases}, t \geq 0 \quad (\text{A.6})$$

Finding the intersection of the the ray with a the outer surface of some sphere with radius r_i occurs for values of t where the line hits the sphere. This occurs for

$$\begin{aligned} x^2 + y^2 + z^2 &= r_i^2 \vec{P} \cdot \vec{P} = r_i^2 \\ (\vec{S} + t\vec{L}) \cdot (\vec{S} + t\vec{L}) &= r_i^2 \\ t^2(\vec{L} \cdot \vec{L}) + t(2\vec{S} \cdot \vec{L}) + (\vec{S} \cdot \vec{S} - r_i^2) &= 0 \end{aligned}$$

Values of t are found with the quadratic formula

$$t = \frac{-b \pm \sqrt{b^2 - 4ac}}{2a} \quad (\text{A.7})$$

where

$$\begin{aligned} a &= \vec{L} \cdot \vec{L} \\ b &= 2\vec{S} \cdot \vec{L} \\ c &= \vec{S} \cdot \vec{S} - r_i^2 \end{aligned} \quad (\text{A.8})$$

If $b^2 - 4ac < 0$, the ray does not intersect with the sphere. If $b^2 - 4ac = 0$ the ray touches, but does not travel through the sphere. Finally, if $b^2 - 4ac > 0$, the ray travels through the sphere.

A.2.2 Cylindrical

For k finite cylindrical shells of height $\pm z^*$, the initial point is given as

$$\begin{aligned}
 r &= \sqrt{(r_{i+1}^2 - r_i^2)\lambda_1} + r_i \\
 \theta &= 2\pi\lambda_2 \\
 x &= r \cos(\theta) \\
 y &= r \sin(\theta) \\
 z &= z^*(2\lambda_3 - 1) \\
 \lambda_x &= U[0, 1]
 \end{aligned} \tag{A.9}$$

The source point shall be described as $\vec{S} = [x, y, z]$ and the detector located at $\vec{D} = [r_d, 0, 0]$, where $[0, 0, 0]$ is the center of the cylinder with end caps centered at $[, 0, \pm z^*]$ and $r_d > r_k$.

Finding the intersection of the the ray with a the outer surface of some cylinder with radius r_i occurs for values of t where the ray hits the edge. This occurs for

$$\begin{aligned}
 x^2 + y^2 &= r^2 \\
 (S_x + tD_x)^2 + (S_y + tD_y)^2 &= r_i^2 \\
 t^2(D_x^2 + D_y^2) + t(2S_xD_x + 2S_yD_y) + (S_x^2 + S_y^2 - r_i^2) &= 0
 \end{aligned}$$

Values of t are found with the quadratic formula given in Eq. A.7 where the coefficients are

$$\begin{aligned}
 a &= D_x^2 + D_y^2 \\
 b &= 2S_xD_x + 2S_yD_y \\
 c &= S_x^2 + S_y^2 - r_i^2
 \end{aligned} \tag{A.10}$$

If $b^2 - 4ac < 0$, the ray does not intersect with the cylinder. If $b^2 - 4ac = 0$ the ray touches, but does not travel through the cylinder. Finally, if $b^2 - 4ac > 0$, the ray travels through the cylinder.

A.2.3 Pseudo-code

Using the equations, a psuedo-code for finding the path a ray takes through k layers is given as:

1. Set sum intensity $S = 0$.
2. **For** history $m = 0, \dots, m_{max}$
 - (a) Initialize attenuation value $A = 0$.
 - (b) Select a gamma emitting region x .
 - (c) Using Eq. A.3 or Eq. A.9, select a starting point in the region and Eq. A.5 to determine the distance d and direction \vec{L} from the source to the detector.
 - (d) **For** $i = x - 1, \dots, 0$
 - Using the coefficients in Eq. A.8 or AppA:Eq-cylCoeff for r_i and Eq. A.7, determine if the ray passes through the inner layer.
 - **If** ray intersects layer, multiply distance from last interaction to layer boundary by the energy appropriate cross section for the region. Add this value to A.

Else, break
 - (e) **For** $j = i, \dots, k$
 - Using the coefficients in Eq. A.8 or AppA:Eq-cylCoeff for r_j and Eq. A.7, determine the distance the ray travels through the layer. Multiply distance from last interaction to layer boundary by the energy appropriate cross section for the region. Add this value to A.
 - (f) Add $\frac{e^{-A}}{4\pi d}$ to S.
3. Calculate $\phi = \frac{I_0 S}{m_{max}}$ where I_0 is the intensity of the in emissions per unit time.

A.3 Comparison

A comparison between the stochastic and deterministic methods, with a validation using MCNP, will be performed in this section. The model being simulated is a sphere of radius 3.151 cm comprised of highly enrich uranium with a 1.6 cm radius void. The uranium density is 18.7 g/cm³. A four line source is comprised of values listed in table A.1. A point detector is placed 70.2 cm from the center

Table A.1 Source energy and intensity for comparison of ray tracers.

Energy (keV)	intensity
144	1.55E5
186	7.99E5
766	4.79E1
1001	1.27E2

of the sphere. The results from the stochastic and deterministic ray tracer are shown in table A.2. The results show strong agreement across all methods.

Using the same four line source, uranium density, and detector location, a cylinder with approximately the same volume as the previous sphere for a total height of 4.919 cm centered so that 2.2495 cm exists above and below the plane containing the detector is modeled. The results are listed in Table A.3. Once again, the results show strong agreement across both methods.

Table A.2 Comparison between MCNP and the deterministic and stochastic ray tracers for spherical shells.

method	Energy (MeV)	Flux
Deterministic $k=400$ subdivisions	0.144	1.511
	0.186	14.78
	0.766	0.0126
	1.001	0.0443
Stochastic $m_{max}=5E5$	0.144	1.510
	0.186	14.57
	0.766	0.0126
	1.001	0.0442
MCNP $nps=1E8$	0.144	1.438±0.2%
	0.186	13.97±0.2%
	0.766	0.0120±0.2%
	1.001	0.0423±0.1%

Table A.3 Comparison between MCNP and the stochastic ray tracer for cylindrical shells.

method	Energy (MeV)	Flux
Stochastic $m_{max}=5E5$	0.144	1.552
	0.186	14.95
	0.766	0.0129
	1.001	0.0456
MCNP $nps=1E8$	0.144	1.477±0.2%
	0.186	14.38±0.2%
	0.766	0.0123±0.2%
	1.001	0.0436±0.1%